

PhD Dissertation

Ana M^a Rodríguez Pérez

Valencia, November 2014



UNIVERSITAT
POLITÈCNICA
DE VALÈNCIA




PhD Dissertation

Synthesis of Planar Microwave Circuits based on Metamaterial Concepts through Aggressive Space Mapping

Departamento de Comunicaciones
Universitat Politècnica de València

Author
Ana Rodríguez Pérez
Advisor
Dr. Vicente E. Boria Esbert

Valencia, November 2014



Synthesis of Planar Microwave Circuits based on Metamaterial Concepts through Aggressive Space Mapping

Ana María Rodríguez Pérez

Thesis advisor: Dr. Vicente E. Boria Esbert

Thesis submitted to the School of Telecommunication Engineering
(ETSI de Telecomunicación) in Partial Fulfillment of the
Requirements for the Degree Doctor of Philosophy

Universitat Politècnica de València
November 2014

RESUMEN

Las aplicaciones de RF y microondas representan uno de los sectores con mayor crecimiento en el sector de la electrónica de altas prestaciones, donde uno de los factores críticos es la innovación. Los distintos fabricantes compiten en aras a cumplir unas determinadas especificaciones de mercado, reduciendo en la medida de lo posible los costes, el tamaño y/o peso de los dispositivos (entre otros criterios). Bajo este escenario, las líneas de transmisión basadas en metamateriales pueden considerarse como una alternativa muy interesante a las líneas de transmisión convencionales, al presentar unas dimensiones menores (compatibles con procesos de fabricación planares) y una mayor flexibilidad de diseño (mayor número de grados de libertad). Y no sólo eso, gracias a ellas se puede obtener propiedades como la ingeniería de dispersión o de impedancias que no son realizables con otras tecnologías. Sin embargo, a pesar de su gran potencial, el impacto en la industria no puede ser todavía considerado relevante, siendo una de las principales causas la complejidad asociada a su síntesis y diseño. A día de hoy, estos procesos se basan en la experiencia y conocimientos del ingeniero, el cual mediante costosos simuladores electromagnéticos y otros procedimientos de extracción de parámetros, tras un arduo proceso, llegará al resultado requerido.

El objetivo de esta tesis, es contribuir a la simplificación y aceleración del diseño/síntesis de las líneas de transmisión artificial. De forma más específica, a las líneas que se obtienen cargando periódicamente una línea de transmisión convencional con resonadores eléctricamente pequeños, como son el resonador de anillos abiertos (SRRs) o su complementario (CSRR). Se pretende automatizar este proceso usando técnicas de Mapeado Espacial (en inglés Space Mapping). A diferencia de otros métodos, la síntesis real se realiza a partir de unos determinados valores circuitales objetivo (dato), que son los del circuito eléctrico equivalente que caracteriza a la estructura que se pretende sintetizar. Con el fin de lograr que el método sea práctico y útil, se han realizado distintos esfuerzos enfocados a determinar si, dada una respuesta objetivo (descrita mediante los valores circuitales) y una tecnología (características de sustrato, límites de fabricación dados por el usuario), la estructura es físicamente realizable (determinación de una región de convergencia asociada). Esta técnica ha sido

formulada con éxito y se denomina “Two-Step Aggressive Space Mapping Approach”.

En este trabajo se presentan los distintos avances realizados hasta la fecha, desde la síntesis de distintas celdas unidad hasta su aplicación a distintos diseños más complejos, concretamente de diversos circuitos pasivos –filtros, divisores- basados en metamateriales. Los resultados obtenidos son prometedores y prueban la validez del método, así como su aplicación potencial a otras celdas unidad y diseños más complejos. El conocimiento general adquirido con estos casos de estudio constituye una buena base para la futura implementación de estas técnicas de síntesis en programas (software) de carácter comercial, que de este modo incrementen su competitividad en los mercados y puedan contribuir a un uso más generalizado de la tecnología basada en líneas de transmisión artificiales.

RESUM

Les aplicacions de RF i microones representen un dels sectors amb major creixement en el sector de l'electrònica d'altres prestacions, on un dels factors crítics és la innovació. Els diferents fabricants competeixen a fi de complir unes determinades especificacions de mercat, reduint en la mesura del possible els costos, la grandària i/o el pes dels dispositius (entre altres criteris). Sota aquest escenari, les línies de transmissió basades en metamaterials poden considerar-se com una alternativa molt interessant a les línies de transmissió convencionals, en presentar unes dimensions menors (compatibles amb processos de fabricació planars) i una major flexibilitat de disseny (major nombre de graus de llibertat). I no només això, gràcies a elles es pot obtenir propietats com l'enginyeria de dispersió o d'impedàncies o no realitzables amb altres tecnologies. No obstant això, malgrat el seu gran potencial, l'impacte en la indústria no pot ser considerat encara rellevant, sent una de les principals causes la complexitat associada a la seua síntesi i disseny. A dia de hui, aquests processos es basen en l'experiència i coneixements de l'enginyer, el qual mitjançant costosos simuladors electromagnètics i altres procediments com a extracció de paràmetres, després d'un ardu procés, arribarà al resultat requerit.

L'objectiu d'aquesta tesi, és contribuir a la simplificació i acceleració del disseny/síntesi de les línies de transmissió artificial. De forma més específica, a les línies que s'obtenen carregant periòdicament una línia de transmissió convencional amb ressonadors elèctricament petits, com són el ressonador d'anells oberts (SRR) o el seu complementari (CSRR). Es pretén automatitzar aquest procés usant tècniques de Mapejat Espacial (en anglès Space Mapping). A diferència d'altres mètodes, la síntesi real es realitza a partir d'uns determinats valors circuitals objectiu, que són els del circuit elèctric equivalent que caracteritza a l'estructura a sintetitzar. Amb la finalitat d'aconseguir que el mètode sigui pràctic i útil, s'han realitzat diferents esforços enfocats a determinar si, donada una resposta objectiu (descrita mitjançant els valors circuitals) i una tecnologia (característiques de substrat, límits de fabricació donats per l'usuari), l'estructura és físicament realitzable (determinació d'una regió de convergència associada). Aquesta tècnica ha estat formulada amb èxit i es denomina "Two-Step Aggressive Space Mapping Approach".

En aquest treball es presenten els diferents avanços realitzats fins hui, des de la síntesi de diferents cel·les unitat fins a la seua aplicació a diferents dissenys més complexos, concretament de diversos circuits passius –filtres, divisors- basats en metamateriales. Els resultats obtinguts són prometedors i proven la validesa del mètode, així com la seua aplicació potencial a altres cel·les unitat i dissenys més complexos. El coneixement general adquirit amb aquests casos d'estudi constitueix una bona base per a la futura implementació en un programari de caràcter comercial, la qual cosa pot incrementar la seua competitivitat als mercats i puguin contribuir a un ús més generalitzat de la tecnologia basada en línies de transmissió artificials.

ABSTRACT

RF and microwave applications represent one of the fastest-growing segments of the high performance electronics market, where ongoing innovation is critical. Manufacturers compete intensively to meet market needs with reduced cost, size, weight and many other performance criteria demands. Under this scenario, transmission lines based on metamaterial concepts can be considered a very interesting alternative to the conventional transmission lines. They are more compact (compatible with planar manufacturing processes) and present higher degrees of design flexibility. Furthermore, metamaterial transmission lines can also provide many other unique properties not achievable with ordinary transmission lines, such as dispersion or impedance engineering. Nevertheless, the impact in the industry is still not relevant, mostly due to the complexity of the related synthesis and design procedures. These procedures are mainly based on the engineer's experience, with the help of costly full-wave electromagnetic (EM) simulators and parameter extraction methods.

The aim of this thesis is to contribute to simplify and speed up the synthesis and design procedures of artificial transmission lines. In particular, the lines obtained by periodically loading a conventional transmission line with electrically small resonators, such as split ring resonators (SSRs) or its complementary particle (CSRR). The design procedure is automated by using Space Mapping techniques. In contrast to other alternative methods, real synthesis is found from the circuit schematic (that provides a given target response) and without need of human intervention. Some efforts to make the method practical and useful have been carried out. Given a certain target response, it is determined whether it can be physically implemented with a chosen technology, and hence proceeding next to find the synthesis, or not. For this purpose, a two-step Aggressive Space Mapping approach is successfully proposed.

In contrast to other methods, the real synthesis is found from certain target circuit values (corresponding to the equivalent circuit model that characterizes the structure to be synthesized). Different efforts have been carried out in order to implement a useful and practical method. Some of them were focused to

determine if, given certain circuit parameters (which determine the target response) and certain given technology specifications (permittivity and height of the substrate, technology limits), that response is physically realizable (convergence region). This technique was successfully formulated and it is known as “Two-Step Aggressive Space Mapping Approach”.

In this work, the latest improvements made till date, from the synthesis of basic unit cells until different applications and kinds of metamaterial-based circuits, are presented. The results are promising and prove the validity of the method, as well as its potential application to other basic cells and more complex designs. The general knowledge gained from these cases of study can be considered a good base for a coming implementation in commercial software tools, which can help to improve its competitiveness in markets, and also contribute to a more general use of this technology.

AGRADECIMIENTOS

Toda etapa en la vida tiene su principio y su fin y con esta redacción cierro el capítulo vital denominado tesis. Ha sido una etapa enriquecedora tanto a nivel personal como profesional, que me ha dado la oportunidad de conocer sitios increíbles y a gente de lo más variopinta y excepcional. Miro el mundo con una mirada distinta, más clara y nítida, pero siendo consciente de que me quedan muchas lecciones por aprender. Nombraré a continuación a varias de las personas a las que estoy especialmente agradecida por haber enriquecido mi vida y por ayudarme a recorrer este tramo del camino.

En primer lugar al catedrático Vicente E. Boria, por creer en mí y guiarme en todo el proceso. Gracias de todo corazón, eres una persona genial en el más amplio sentido de la palabra, personal y profesional. Destacar en un determinado área es difícil, pero en tantas está sólo al alcance de unos pocos privilegiados como tú.

Al grupo GEMMA/CIMITEC, perteneciente a la Universidad Autónoma de Barcelona. Gracias por haber realizado este tándem, que nos ha permitido explorar nuevos caminos juntos. Ha sido un auténtico honor y un placer poder trabajar tanto con el catedrático Ferran Martín, como con el ya doctor Jordi Selga.

Al GAM en su conjunto, no solo por compartir su saber, sino por hacer que los momentos buenos fueran mejores y los malos, menos malos. Tampoco me olvido de otros integrantes del iTEAM, VSC, AuroraSAT SL, i3M, Wave Fenomena Group que han estado ahí, os expreso mi gratitud en todos los idiomas que conozco: ¡Gracias! ¡Gràcies! Thanks! Grazie! Merci! Obrigada! Danke! Kiitos!

A mi familia y amigos, sois mi más preciado tesoro. En otras palabras, a todos los que conformáis mi mundo amarillo y en especial, a un amarillo que ha mutado a un intenso color naranja muy valenciano ;)

"AMARILLO. Definición: Dícese de aquella persona que es especial en tu vida. Los amarillos se encuentran entre los amigos y los amores. No es necesario verlos a menudo o mantener contacto con ellos...". Albert Espinosa. El mundo amarillo.

TABLE OF CONTENTS

List of Figures	xiii
List of Tables	xxi
List of Acronyms and Symbols	xxiii
1 Introduction	3
1.1 Motivation	3
1.2 State of the art	9
1.3 Thesis Structure	17
References	18
2 Metamaterials	27
2.1 General Overview	28
2.2 Transmission Lines Based on MTM Concepts.....	34
2.2.1 Resonant Approach	41
2.2.1.1 TLs based on SRRs.....	46
2.2.1.2 TLs based on CSRRs	49
2.2.1.3 TLs based on OSRRs and OCSRRs	52
References	58
3 Optimization	67
3.1 Introduction.....	67
3.2 Space Mapping.....	71
3.2.1 Concept and classical formulation	71
3.2.2 State of the art.....	74
3.3 Application Examples.....	82
3.3.1 Aggressive Space Mapping (ASM)	89
3.3.1.1 Determination of initial layout.....	92

Table of Contents

3.3.1.1.1 TLs based on CSRRs 93

3.3.1.1.2 TLs based on OCSRRs..... 94

3.3.1.2 Parameter Extraction 95

3.3.1.2.1 TLs based on CSRRs 95

3.3.1.2.2 TLs based on OCSRRs..... 98

3.3.1.3 Automated Synthesis 99

3.3.1.3.1 TLs based on CSRRs 99

3.3.1.3.2 TLs based on OCSRRs..... 103

3.3.2 ASM + Line Search 105

3.3.3 Identification of a convergence region 108

3.3.3.1 TLs based on CSRRs 108

3.3.3.2 TLs based on OCSRRs 118

References 124

4 Applications 131

4.1 Band-stop filter based on CSRR-loaded metalines..... 131

4.2 Dual-band power divider based on CSRR-gap-loaded metalines 134

4.3 Band-pass filter based on OCSRRs TLs 139

References 144

5 Conclusions and Future Work 147

5.1 Conclusions 147

5.2 Future Research Lines 148

List of Publications..... 151

International Journals and Book Chapters 151

International Conferences..... 152

LIST OF FIGURES

Fig. 1.1. - Examples of classic transmission lines: (a) rectangular waveguide, (b) microstrip line (sizes are not scaled, microstrip is much thinner)..... 4

Fig. 1.2. - Rectangular Waveguide with EBG sidewalls. Boundary conditions in the waveguide: sidewalls are perfect magnetic conductor (PMC) while top /bottom walls are PEC (perfect electric conductor). 5

Fig. 1.3. - Examples of Gap Waveguide technology: (a) single hard wall waveguide, (b) ridge gap waveguide..... 5

Fig. 1.4. -Substrate Integrated Waveguide typical layout. 6

Fig. 1.5. - Composite right left-handed mushroom structure (a), and equivalent circuit (b) where C_L is enhanced due to the presence of interdigital capacitors. ... 7

Fig. 1.6. - Layout of a filter implemented in CPW with SRR and shunt connected metallic strips [25]..... 8

Fig. 1.7. - Flowchart diagram: (a) conventional versus (b) modern (EM-based CAD) microwave design. 11

Fig. 1.8. - Conceptual diagram of: Artificial Neural Networks (a) and Space Mapping (b)..... 12

Fig. 1.9. - Block diagram of optimization process with OSA. 13

Fig. 1.10. - Block diagram of Space Mapping Framework (SMF) architecture. .. 14

Fig. 1.11. – Fine model (a) and coarse model (b) corresponding to the unit cell of the bandpass filter synthesized in [33]. The SRR design parameters (not indicated in Fig.1.11.a) are: r_m (mean radius), w (rings’ width), d (separation between rings), and g (rings’ split). 15

Fig. 1.12. - (a) Layout of the interdigital/stub unit cell. (b) Equivalent circuit model..... 16

Fig. 2.1. - Conventional materials versus LH MTMs: light refracted by the material; orientation of the different vectors: electric field E , magnetic field H , Poynting vector P and wave vector k . $Re()$ indicates real part..... 28

Fig. 2.2. - Conventional materials (properties derive from constituent atoms) versus metamaterials (properties derive from their constituent units)..... 28

Fig. 2.3. - Classification of materials based on the permittivity (ϵ) and permeability (μ). $Re()$ indicates real part. 32

Fig. 2.4. - Classification of materials based on bulk modulus (K) and density values (ρ). $\gamma=a+j\beta$ is the propagation constant (see section 2.2). 32

List of Figures

Fig. 2.5. - Simplified lumped-element equivalent circuit for: (a) RH TL; (b) LH TL; (c) CRLH-TL with L'_R, C'_R, L'_L and C'_L per-unit-length quantities. 34

Fig. 2.6. - Dispersion diagrams: (a) RH TL (b) LH TL; with L'_R, C'_R, L'_L and C'_L per-unit-length quantities. 36

Fig. 2.7. - (a) Schematic for MTM TL, with N (reciprocal and symmetrical) unit cells with lattice constant d . (b) Every unit cell is characterized by the transfer matrix T_{cell} 38

Fig. 2.8. - Dispersion diagrams for: (a) unbalanced CRLH-TL; (b) balanced CRLH-TL. 40

Fig. 2.9. - Cross-sectional view of a Helmholtz resonator (a). An acoustic TL ($K < 0$) that consists of an array of Helmholtz resonators (b). Picture extracted from [32]. 41

Fig. 2.10. - Sub-wavelength resonators: (a) SRR, (b) DS SRR, (c) SR, (d) NB-SRR, (e) MSRR. Metal parts are depicted in grey. 42

Fig. 2.11. - Topology of an SRR (a) and its dual particle CSRR (b). Metal parts are depicted in grey. 43

Fig. 2.12. - Sub-wavelength resonators: (a) OSRR, (b) OCSRR. 43

Fig. 2.13. - Parameter extraction process. 44

Fig. 2.14. - (a) Topology of a SRR with the relevant dimension: external radius (r_{ext}), mean radius (r_0), ring's width (c), distance between the metallic rings (d). (b) Equivalent circuit of a SRR. 46

Fig. 2.15. - Topology of a basic unit cell of a CPW loaded with SRRs (a), with its equivalent circuit (b). Topology of a basic unit cell of a CPW with SRRs and shunt strips (c), and its equivalent circuit (d). SRRs in dark grey are on the bottom. 47

Fig. 2.16. - (a) Topology of a CPW loaded with SRRs, shunt strips and varactors; (b) simulated response of the 3-stage tunable filter [48]. 48

Fig. 2.17. - (a) Topology of microstrip line loaded with SRRs, and metallic vias [50]. (b) Prototype that demonstrates application to spurious suppression [28]. (c) Schematic of dual-band matching network, including slot antenna [51]. 49

Fig. 2.18. - (a) Topology of a CSRR with its relevant dimensions. Metal regions are depicted in grey. (b) Equivalent circuit of a CSRR. 49

Fig. 2.19. - Basic unit cell of a microstrip loaded with CSRR (a), and equivalent circuit (b). Basic unit cell of microstrip loaded with CSRR and gaps (c), and equivalent circuit (d). The upper metallization is depicted in black and ground plane in grey. 50

Fig. 2.20. - Basic unit cell, the two shunts are connected to ground by vias (a); equivalent circuit (b). The upper metallization is depicted in black and ground plane in grey. 51

Fig. 2.21. - (a) Generalized impedance model; (b) Modified circuit model for topology depicted in Fig. 2.19.a, (c) Modified circuit model for topology depicted in Fig. 2.19.c. Models from [56]. 51

Fig. 2.22. - Basic unit cell of a CPW loaded with CSRRs positioned on the ground plane (a), idem with added slots in the center conductor (b), and equivalent circuit of the structure in (c). At the edges of the structure the tapers used to perform the measurements are depicted. Figures extracted from [59]. 52

Fig. 2.23. - (a) Typical topology of an OCSRR (the two terminals/ports are indicated). (b) Equivalent circuit of an OCSRR. 52

Fig. 2.24. - (a) Typical topology of an OSRR excited by a microstrip line. Ground plane window is practiced in order not to disturb the EM behavior of the OSRR. (b) Equivalent circuit of an OCSRR: 1st approach. (c) More accurate circuit model (taking into account access lines) with $L'_s = L_s + 2L$ 53

Fig. 2.25. - (a) Typical topology of an OSRR in CPW technology. Equivalent circuit of an OCSRR (b), simplified circuit model with $L'_s = L_s + 2L$ 53

Fig. 2.26. - (a) Topology of OCSRRs loaded in CPW, (b) Equivalent circuit 1, (c) Equivalent circuit $L'_p = L_p/2$, $C'_p = 2 \cdot (C + C_p)$ 54

Fig. 2.27. - (a) Typical network of a bandpass filter with admittance inverters and shunt LC resonators. (b) Layout of first bandpass filter implemented with OCSRR [40]. 55

Fig. 2.28. - a) Layout of a wide-band bandpass filter (b) Photograph of the prototype, (c) Frequency response (measured, EM simulation and circuit simulations) [63]. 55

Fig. 2.29. - (a) Layout of a wide-band bandpass filter (order-3 Chebyshev), (b) Frequency response (measured, EM and circuit simulations (c) Circuit model, including access line effect ($L'_s = L_s + 2L$, $L'_p = L_p/2$, $C'_p = 2 \cdot (C + C'_p)$). L_{sh} can be included in the schematic for better accuracy. 56

Fig. 2.30. - (a) Layout of a wide-band bandpass filter, (b) Photograph of the prototype, (c) Frequency response (measured, EM simulation and circuit simulations) [64]. 57

Fig. 3.1. - Flowchart of the Surrogate-Based Optimization process. 70

Fig. 3.2. - Concept of Space Mapping. 71

Fig. 3.3. - (a) Space Mapping Concept. (b) Frequency Space Mapping Concept (first introduced in [8]). 75

Fig. 3.4. - Connection between SM and direct optimization in HASM [19]. 77

List of Figures

Fig. 3.5. – *Space Mapped neuromodeling concept (SMN) [11]* 79

Fig. 3.6. - (a) *Original Space Mapping, the mapping with the coarse model constitutes the “surrogate” [6]. (b) Implicit Space Mapping, with input and output mapping [25].*..... 80

Fig. 3.7. - *Tuning Space Mapping: (a) Concept diagram [28], (b) Flowchart [29].* 81

Fig. 3.8. - *Application diagram for the negative permittivity unit cell. The coarse model is the equivalent circuit model, whereas the fine model is the EM model.* 82

Fig. 3.9. - *Typical magnitude (a) and phase (b) of the transmission coefficient of the CSRR-based artificial transmission lines shown in Fig. 3.8. $r_{ext}=4.46\text{mm}$, $c=0.44\text{mm}$, $d=0.23\text{mm}$, $W=3.10\text{mm}$.*..... 83

Fig. 3.10. - *Layout (a), equivalent circuit (b), T-model transformation of the previous equivalent circuit (c).*..... 84

Fig. 3.11. – *Representation of the series (χ_{se}) and shunt (χ_{par}) reactance, the characteristic impedance (Z_c) and the phase (βd) of a unit cell in Fig. 3.10. Two different cases are represented: $\omega_{se} < \omega_{par}$ and $\omega_{se} > \omega_{par}$ [38].* 86

Fig. 3.12. – *Layout of a CRLH unit cell where series gap presents different shapes: (a) flat, (b) T-shaped, (c) meandered.* 86

Fig. 3.13. - *Typical magnitude (a) and phase (b) of the scattering parameters of a CSRR-based artificial transmission line like the one shown in Fig. 3.12.a.*..... 87

Fig. 3.14. - *OCSR shunt connected to microstrip line. Unit cell layout (a), equivalent circuit (b), and frequency response of S-parameters magnitude (c).* .. 88

Fig. 3.15. - *Illustration of the flow-diagram of the ASM algorithm with constrains.*..... 89

Fig. 3.16. - *Illustration of the ASM algorithm evolution (error norm versus iteration number) in the case of a CSRR-based line (CRLH) using different shrinking factors. Target $x_c^* = [L, C, L_c, C_c, C_g] = [5.141\text{nH}, 14.841\text{pF}, 2.635\text{nH}, 2.812\text{pF}, 0.773\text{pF}]$.*..... 90

Fig. 3.17. - *Comparison of electromagnetic and circuitual simulations (PE) for the cell of negative permittivity. (a) S_{11} in Smith Chart (b) Frequency response of transmission coefficient S_{21} (magnitude and phase).* 96

Fig. 3.18. - *Comparison of EM simulation $x_{em}=[r_{ext}, c, d, W, s]=[5\text{mm}, 0.25\text{mm}, 0.3\text{mm}, 3.5\text{mm}, 0.3\text{mm}]$ and circuitual simulation $x_c=[L, C, L_c, C_c, C_g] = [3.882\text{nH}, 18.647\text{pF}, 2.751\text{nH}, 3.282\text{pF}, 0.893\text{pF}]$ obtained by PE for a CRLH unit cell. (a) S_{11} in Smith Chart (b) Frequency response of S-parameters (magnitude and phase).* 98

Fig. 3.19. - *Comparison of EM simulation $x_{em} = [r_{ext}, d, e] = [2.5\text{mm}, 1.2\text{mm}, 0.5\text{mm}]$, with $c = 0.25\text{mm}$ and circuitual simulation $x_c=[L_p, C_p, L_{sh}] = [1.612\text{nH}$,*

4.299pF, 0.584nH] obtained by PE for a shunt OCSR in microstrip: (a) S-parameters (in magnitude); (b) susceptance (B). The susceptance slope parameter *b* is calculated according to expression (4.15). 99

Fig. 3.20. - Evolution of the error function in norm ($\|f\|$) versus iteration number. 100

Fig. 3.21. - Frequency response of the transmission coefficient S_{21} in magnitude (a) and phase (b). 101

Fig. 3.22. - Evolution of the error function with the iteration number: (a) $\|f\|$; (b) $\|f_{norm}\|$ 102

Fig. 3. 23. - Frequency response of the transmission S_{21} and reflection S_{11} coefficients in magnitude (a) and phase (b). 103

Fig. 3. 24. - Evolution of the error function (norm) with the iteration no.: a) $\|f\|$; (b) $\|f_{norm}\|$ 104

Fig. 3.25. - Comparison of EM simulation of initial layout (dot line in light colors) and final layout (solid line) and circuital simulation (dashed line) of target parameters $x_c^* = [3.8nH, 4.1pF, 0.5nH]$: S-parameters in magnitude (a) and phase (b). 104

Fig. 3.26. - Flow-diagram of the ASM algorithm with Line Search (highlighted in yellow). 105

Fig. 3. 27. - Evolution of $\|f\|$ versus iteration number, using ASM with $\delta = 0.4$ (solid blue line) and ASM+LS (dashed black line). 106

Fig. 3.28. - Evolution of $\|f\|$ versus iteration number, using ASM (solid blue line) and ASM+LS (dashed black line), and ASM+LS modified (dotted green line). 108

Fig. 3.29. - Schematic of the new proposed two-step ASM algorithm. 109

Fig. 3. 30. - ASM Pre-optimization diagram used to determine the convergence region for a CSRR-loaded metaline. 110

Fig. 3. 31. - (a) Convergence region for $x_{cr}^* = [L^*, C^*] = [5.08 nH, 4.43 pF]$, defined by 4 vertices. (b) Regions defined with different constraints for the same x_{cr}^* . .. 111

Fig. 3.32. - Evolution of the error with different analytical (dashed lines) and interpolated (solid lines) initial layouts: T (blue), U (green) and V (pink). Be aware that x-axis graphic starts in 0 instead of 1. 114

Fig. 3.33. - Frequency response of the transmission coefficient (S_{21}) in magnitude and phase: (a) Target U, (b) Target V 115

Fig. 3.34. - (a) 3D-Convergence region for $x_{cr}^* = [L^*, C^*] = [3.046 nH, 12.144 pF]$ (b) 2D-Convergence region for $x_{cr}^* = [L^*, C^*, C_g^*] = [9.45 nH, 17.93 pF, 1.01 pF]$ cell with a T-shape gap. Substrate RO3010 $\epsilon_r = 10.2$. Thickness 1.27mm in (a), and 0.625mm in (b). 115

List of Figures

Fig. 3.35. - ASM pre-optimization diagram used to determine the convergence region for a CSRR-gap-loaded metaline. 116

Fig. 3.36. - Comparison between the EM simulation of initial (blue dash line) and final layout (black solid line) and circuital simulation (red dot line). (a) Magnitude and (b) phase of scattering parameters. 117

Fig. 3. 37. - Schematic of the new proposed ASM algorithm. 118

Fig. 3.38. - Estimated convergence regions calculated for external radius r_{ext} starting from 2 mm till 3.25 mm, in steps of 0.25 mm for an approximated target $L_{sh}^=0.5$ nH, which corresponds to $e =0.277$ mm. The 4 vertexes are determined by the layouts obtained with the different combinations of the extreme values of c and d. $x_{c_{cr}}^* = [3.8$ nH, 4.1 pF]. 119*

Fig. 3.39. - Graphical representation of the vertexes used for the OCSR radius determination. 121

Fig. 3.40. - Estimated convergence region fixing the radius to $r_{ext}=2.198$ mm. Red dot corresponds to the target given by: $L_p^=3.8$ nH; $C_p^*=4.1$ pF. 121*

Fig. 3.41. - ASM Pre-optimization diagram for an OCSR-unit cell..... 121

Fig. 3. 42. - Evolution of the error function with the iteration number: (a) $|f|$; (b) $|f_{norm}|$ 123

Fig. 3. 43. - Comparison of EM simulation of final layout (solid line) and circuital simulation (dot line) of target parameters: $x_c^ = [3.8$ nH, 4.1pF, 0.5nH]: S-parameters in magnitude (a) and phase..... 123*

Fig. 4.1. - Equivalent circuit and layout of the implementer band-stop filter. The small blue rectangles correspond to lines of physical length equal to 2.22mm and width according to the calculated value for each unit cell (see Table 4.2). 132

Fig. 4.2. - Manufactured prototype layout: (a) Ground. (b) Top. 133

Fig. 4.3. - Magnitude of the scattering parameters S_{21} and S_{11} , in blue-dash line the circuital simulation, in green-dot-dot-dash line the EM simulation, and in black-solid line the measurements..... 133

Fig. 4.4. –Schematic of the final prototype. 134

Fig. 4.5. –Dependence of the element values of the CSRR-gap loaded line with the phase of each cascaded transmission line section at f_1 137

Fig. 4.6. – Photograph of the designed dual band power divider. 137

Fig. 4.7. – Comparison between the EM and circuit simulations corresponding to the characteristic impedance (Z_B) and electrical length (βl) of the designed prototype..... 138

Fig. 4.8. –Frequency response (circuit and EM simulation and measurement) of the designed and fabricated dual-band power divider (magnitude of the scattering parameters)..... 139

Fig. 4.9.- Schematic of the 3-order bandpass filter (a), and layout inferred after the synthesis process (b). The circuit target parameters are summarized in Table 4.6 and dimensions in Table 4.6. Microstrip line parameters: $w_0 = 0.211$ mm and $l_0 = 14.94$ mm. 139

Fig. 4.10. - Insertion and return losses of the synthesized bandpass filter based on OCSRRs. 141

Fig. 4.11. - Photograph of the manufactured filter. 141

Fig. 4.12.-Layout of the 3-order bandpass filter (redesigned). The circuit target parameters are summarized in Table 4.7 and dimensions in Table 4.8. The dimension of microstrip $\lambda/4$ lines are the same of the previous design. 143

Fig. 4.13. - Insertion and return losses of the re-designed (enhanced out-of-band response) wideband bandpass filter based on OCSRRs. 143

Fig. 5. 1.- SIR interface programmed in Python. 149

Fig. 5. 2. - Topology of omega and spiral (one turn) inductor. 149

List of Figures

LIST OF TABLES

Table 2. 1. - Analogy Between Acoustic and Electromagnetic Variables and Material Characteristics. 31

Table 3. 1. - Coarse Parameters for CSRR Unit Cell ($\epsilon < 0$)..... 100

Table 3. 2. - Fine Parameters for CSRR Unit Cell ($\epsilon < 0$)..... 101

Table 3. 3. - Coarse Parameters for CSRR Unit Cell (CRLH) and Errors..... 102

Table 3. 4. - Fine Parameters for CSRR Unit Cell (CRLH)..... 103

Table 3. 5. - Coarse Parameters for OCSRR Unit Cell and Errors 104

Table 3. 6. - Fine Parameters for OCSRR Unit Cell..... 105

Table 3. 7. - Fine Parameters for CSRR Unit Cell and Error..... 107

Table 3. 8. - Fine Parameters for CSRR Unit Cell and Error..... 107

Table 3. 9. – Convergence Region Vertices and Required ASM Iterations 111

Table 3. 10. – Optimal Coarse Solutions..... 113

Table 3. 11. - Fine Parameters for the Initial Layout and Errors 113

Table 3. 12. - Fine Parameters for the Final Layout, Iteration Number and Errors 114

Table 3. 13. – Optimal Coarse Solutions..... 116

Table 3. 14. - Fine Parameters for the Final Layout, Iteration No. and Errors 117

Table 3. 15. – Vertexes for OCSRR Radius Determination..... 120

Table 3. 16. – Convergence Region Vertices and ASM Iterations Needed 122

Table 3. 17. - Coarse Parameters for OCSRR Unit Cell and Errors 122

Table 3. 18. - Fine Parameters for OCSRR Unit Cell..... 122

Table 4. 1. - Optimal Coarse Solutions (Unit Cells)..... 131

Table 4. 2. - Fine Parameters for the Final Layout, Iteration No. and Normalized Error..... 132

Table 4. 3. – Optimal Coarse Solutions..... 135

Table 4. 4. – Fine Parameters For Final CSRR-Gap-Loaded Line Unit Cell (T-Shape Gap) 137

List of Tables

*Table 4. 5. - Optimal Coarse Solutions, Reflection and Transmission Zero
Frequencies 140*

*Table 4. 6. - Fine Parameters for OCSRR Unit Cell, Iteration Number and Errors
..... 140*

*Table 4. 7. – Optimal Coarse Solutions, Reflection and Transmission Zero
Frequencies 142*

Table 4. 8. - Fine Parameters, Iteration No. and Error Function Norms 142

LIST OF ACRONYMS AND SYMBOLS

ANN	Artificial Neural Networks (Optimization)
ASM	Aggressive Space Mapping (Optimization)
CAD	Computer Aided Design
CFD	Computational Fluid Dynamics
CPU	Central Processing Unit
CPW	Coplanar Waveguide
CR	Convergence Region
CRLH	Composite Right/Left-Handed (Transmission Line / Media)
CSR	Complementary Split Ring Resonator
DS-SRR	Double-Slit Split Ring Resonator
D-CRLH	Dual Composite Right/Left-Handed (Transmission Line / Media)
DNG	Double Negative (medium)
E-CRLH	Extended Composite Right/Left-Handed (TL/ Media)
EM	Electromagnetic
FDTD	Finite Difference Time Domain
FEM	Finite Element Method
FSM	Frequency Space Mapping
FSS	Frequency Selective Surfaces
GA	Genetic Algorithm (Optimization)
GSM	Generalized Space Mapping (Optimization)
HASM	Hybrid Aggressive Space Mapping (Optimization)
HIS	High Impedance Surface
LFM	Linearized Fine Model
LH	Left-Handed (Transmission Line / Media)

List of Acronyms and Symbols

LS	Line Search (Optimization)
MCM	Mapped Coarse Model
MIC	Microwave Integrate Circuits
MSRR	Multiple Split Ring Resonator
MTM	Metamaterial
MoM	Method of Moments
NB-SRR	Non-bianisotropic Split Ring Resonator
NRI	Negative Refractive Index
OCSRR	Open Complementary Split Ring Resonator
OSRR	Open Split Ring Resonator
PBG	Photonic Band-Gap (crystal)
PCB	Printed Circuit Board
PE	Parameter Extraction
PEC	Perfect Electric Conductor
PMC	Perfect Magnetic Conductor
SB	Surrogate-Based (Optimization)
SIW	Substrate Integrated Waveguides
SM	Space Mapping (Optimization)
SMN	Space Mapping Neuromodel
SMF	Space Mapping Framework
SQP	Sequential Quadratic Progaming (Optimization)
SR	Spiral Resonator
SRR	Split Ring Resonator
SW	Software
TEM	Transverse Electromagnetic (Propagation / Mode)
TL	Transmission Line
TLM	Transmission Line Method
TRASM	Trust Region Aggressive Space Mapping (Optimization)
TSM	Tuning Space Mapping (Optimization)

CHAPTER 1

Introduction

1.1. Motivation

1.2. State of the Art

1.3. Thesis Structure

References

“Never regard study as a duty, but as the enviable opportunity to learn to know the liberating influence of beauty in the realm of the spirit for your own personal joy and to the profit of the community to which your later work belongs”

Albert Einstein



1 INTRODUCTION

Nowadays, RF-microwave engineering is more dependent on computer simulation. As the complexity of structure grows, it becomes more and more complicated to find theoretical models which can predict accurately the behaviour of the structure under study. Therefore, simulation-driven design and optimization has become a must in many areas, such as the one subject of our interest: the synthesis of artificial transmission lines based on metamaterial concepts.

Even most commercial electromagnetic (EM) simulation software supply optimization tools at present time; direct optimization of the real device (EM model) is usually not the smartest way to find a suitable solution, especially if the total CPU cost needs to be minimized. This becomes more than evident or relevant for complex designs, where simulating just one possible realization of the device may be already computationally demanding. Joining this fact to the potentially large number of variables/dimensions that may be optimized (and its mutual dependence), make that the global optimization is at least computationally prohibitive, and do not necessary yield to find a valid solution. Hence, the use of other optimization techniques like Space Mapping (SM), already tested with other microwave devices [1-2] and which avoids direct optimization procedure, seems to be a reasonable way to accelerate and simplify the synthesis of artificial transmission lines.

1.1 Motivation

Choosing a particular technology, as when making other kind of choices, has an implicit trade-off between advantages and drawbacks, and it is finally taken according to the target pursued. Regarding the first generation of microwave transmission lines, i.e. waveguides, main advantages are high power-handling capability and low loss (due to electromagnetic shielding). Those characteristics make them especially useful for space or radar applications. However, they are not suitable for mass production and are bulky and voluminous, which makes them difficult to integrate with planar technology processes [3]. For very low frequencies (under 300 MHz), the waveguide dimensions become impractically large, and for high frequencies (over 300 GHz) the dimensions become impractically small. The waveguide manufacturing process is very complex at

Chapter 1. Introduction

millimetre-wave frequency bands, and very precise machining is required in order to get good metal contact between the different split blocks. A typical example in this technology can be considered the rectangular waveguide depicted in Fig. 1.1.a.

On the other hand, planar transmission lines (stripline, microstrip lines -see Fig. 1.1.b-, slotlines, coplanar waveguides, and several other types of related geometries) are compact, have lower cost, are easy to integrate and adequate for mass production [3]. But, on the contrary to conventional waveguides, planar circuits do not have high power carrying capacity and high Q-factor (losses in planar are higher).

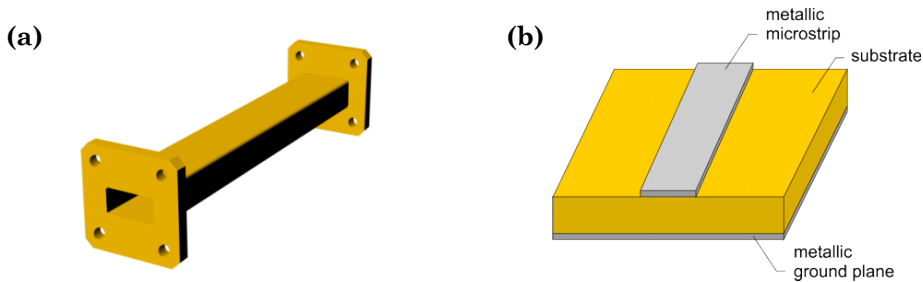


Fig. 1.1. - Examples of classic transmission lines: (a) rectangular waveguide, (b) microstrip line (sizes are not scaled, microstrip is much thinner).

Certain innovations have been applied in order to improve different aspects of the abovementioned transmission lines. Many of these innovations come from the research on new periodic structures known as metamaterials [4-8], which started at the beginning of the last decade. These structures can be made up of metal, dielectric materials, or both, and they present special properties, which are not normally found in nature. The main interest about metamaterials (MTMs) relies on their ability to modify the propagation properties of the waves (acoustic, elastic or electromagnetic), and the resulting higher design flexibility. The nomenclature of metamaterials includes a large range of engineered materials (there is not a standardized nomenclature) as: electromagnetic (photonic) band gap materials (EBG/PBG), high impedance surfaces (HIS), frequency selective surfaces (FSS), double negative medium (DNG) with its equivalencies left-handed media (LHM) or negative index materials (NMI) among others. A deeper overview about these structures, properties and applications can be found in Chapter 2.

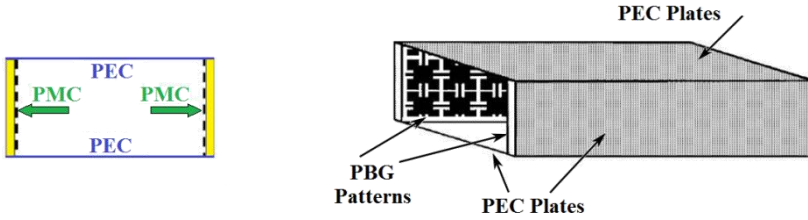


Fig. 1.2. - Rectangular Waveguide with EBG sidewalls. Boundary conditions in the waveguide: sidewalls are perfect magnetic conductor (PMC) while top /bottom walls are PEC (perfect electric conductor).

A straight transference from MTMs to waveguide technology is reported in [9] and illustrated in Fig. 1.2. By placing on the sidewalls of rectangular waveguides PBG patterns, transverse electromagnetic propagation (TEM) with a uniform field pattern inside the guide is achieved. Previously, TEM waveguides have been obtained by using dielectric substrates on the sidewalls of standard metal waveguides. Having higher permittivity values can provide better performance to the device, but with an inherent reduction of bandwidth. The use of PBG sidewalls yields to obtain a wider bandwidth instead.

Regarding waveguide technology is worth mentioning the Gap Waveguide Technology [10] based also in MTMs. It is intended for applications from 30 GHz to Terahertz frequencies, and it presents similar losses to entire-metal rectangular waveguides (no dielectric material), but in this case the manufacturing process is simplified (vertical walls are not required), and there is no requirement for conductive contact between the two different metal pieces making up a gap waveguide prototype. Different examples of this technology are: single hard wall waveguide [11-12], ridge gap waveguide [13] or groove gap waveguides [14], see Fig. 1.3. The Gap Waveguide Technology is protected by a patent application [15].

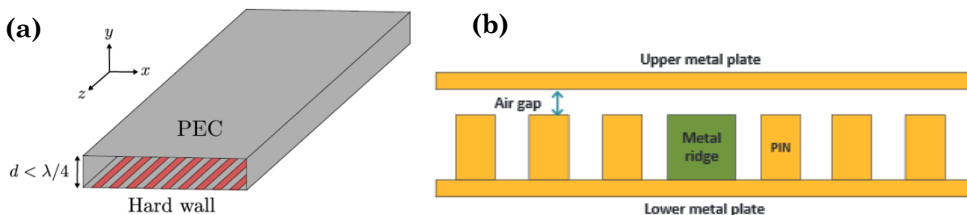


Fig. 1.3. - Examples of Gap Waveguide technology: (a) single hard wall waveguide, (b) ridge gap waveguide.

A mixed/hybrid technology between waveguide and planar transmission lines can be considered the laminated waveguides [16] or Substrate Integrated Waveguide (SIW) [17]. An “artificial” waveguide is synthesized by two parallel rows of via holes embedded in a dielectric substrate, which is covered with conducting sheets on the top and bottom sides (see Fig. 1.4). The manufacturing costs are drastically reduced, especially at high frequencies, since it takes benefits of mature manufacturing techniques like etching slots and drilling via holes in a Printed Circuit Board (PCB). Another interesting point of this feature is the possibility to implement any kind of geometry and form, not possible with other solutions.

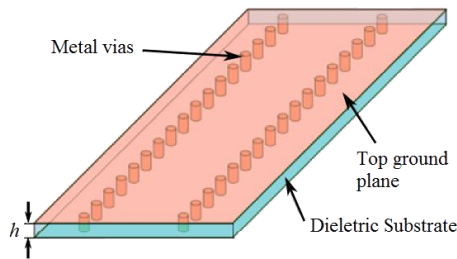


Fig. 1.4. -Substrate Integrated Waveguide typical layout.

Planar metamaterial transmission lines are based on periodically loading a host line with reactive elements (capacitors, inductors, and/or resonators), and exhibiting as result controllable electromagnetic properties. Two different categories are distinguished in literature according to the reactive elements used to load the line. In the first type, they are series capacitance and shunted connected inductors [18-20]. Hence, these lines present right-handed (forward) wave propagation or a left-handed (backward) behaviour, depending on the frequency range the loading elements dominate, thus they are also commonly known as composite right/left-handed transmission lines (CRLH). One example of these lines can be considered the Sievenpiper mushroom structure [21], not proposed initially as metamaterial but as a high impedance surface. Nevertheless, they also exhibit a possible negative refractive index (NRI) structure in the long wavelength regime [4]. They have different interesting applications too, such as the ability to suppress surface waves in planar antennas, which results in the gain enhancement and also in a reduction of side lobes making that the radiation pattern to be better.

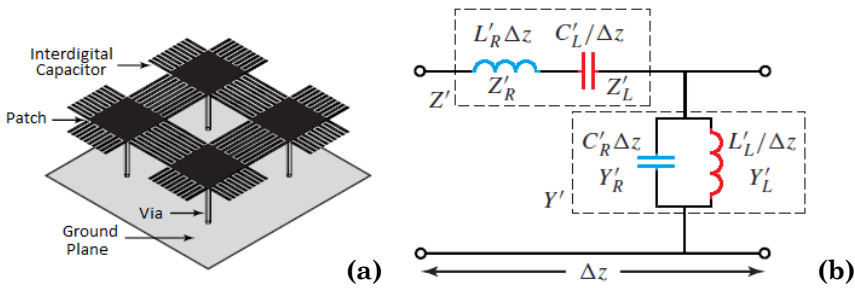


Fig. 1.5. - Composite right left-handed mushroom structure (a), and equivalent circuit (b) where C'_L is enhanced due to the presence of interdigital capacitors.

Afterwards, C. Caloz proposed the dual composite right-left handed (D-CRLH) transmission line [22]. In this case, the series impedance is a parallel LC tank and its shunt admittance a series LC tank, being the dual of the equivalent circuit of conventional CRLH lines shown in Fig. 1.5. The D-CRLH lines exhibit its left-handed band at high frequencies, and its right-handed band at low frequencies. CRLH transmission lines are in general suitable for low-pass, high-pass and band pass applications, while D-CRLH is a band-stop filter in nature. CRLH and D-CRLH structures may be also combined to provide novel and useful dispersion effects, giving rise to extended composite right-left handed transmission line (E-CRLH) which can be very useful for wireless applications [23-24].

The resonant-type approach, i.e. the second type of artificial transmission lines based on MTMs concepts, was initially proposed by F. Martin et al. [25]. In this case the host transmission line is periodically loaded with *sub-wavelength resonators*, such as split ring resonators (SSRs) or its complementary particle (CSRRs). Resonators can be coupled in different ways, giving rise to different kind of lines. The first example proposed (see Fig. 1.6), was obtained by etching SRRs in the back substrate of a coplanar waveguide (CPW) loaded with shunt connected metallic wires. Many applications using this kind of transmission lines (TL) have been already tested and implemented for the microwave field; being its compact size one of the most attractive aspects of this approach [26-27]. Note that many of these lines are included under the category of CRLH [28] or D-CRLH [29], because that name stands for the supporting wave propagation (in certain frequency bands), and it is not linked to the type of reactive elements used to load the host transmission line.

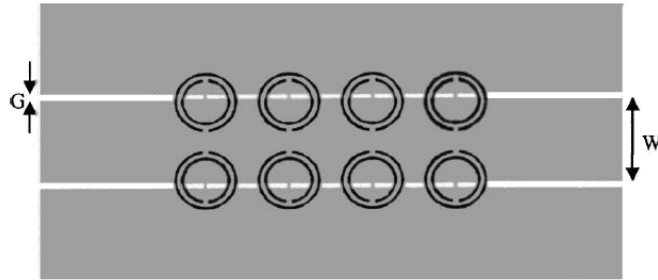


Fig. 1.6. - Layout of a filter implemented in CPW with SRR and shunt connected metallic strips [25].

This thesis was carried out at Microwave Applications Group (GAM) of *Universitat Politècnica de València* (UPV). The main GAM research interest is the development of techniques for the analysis and design of passive components in different technologies: coaxial, waveguide, planar and hybrid (dielectric substrate integrated guides, SIW). Various efforts have been also focused to automate the synthesis and simplify the whole design process of different microwave devices, taking advantage of the already efficient analysis tools implemented by the group. CAD techniques based on space mapping were applied first to waveguide filters [30-31] and later on to SIW [32]. Hence this work is connected with this latter research line, i.e. proposing a new methodology to automate the synthesis of MTMs transmission lines, in particular the resonant-type approach. In contrast to previous works from the group, a commercial analysis tool ANSOFT Designer was used for the full-wave EM analysis. Note that Designer was later acquired by ANSYS, so it may be referred also as ANSYS DesignerRF [33]. The first successful attempt to synthesize “in an automated way” a left-handed device, in particular a coplanar filter similar to the one shown in Fig. 1.6, was achieved in 2007 by members of this research group [34]. Therefore, they can be considered pioneers for applying, by the first time, these techniques to this technology. Moreover, a close collaboration with the group GEMMA/CIMITEC, which is part of the Electronics Engineering Department of the *Universitat Autònoma de Barcelona* (UAB), was established. GEMMA/CIMITEC has been part of the European Network of Excellence NoE 500252-2 METAMORPHOSE (Metamaterials Organized for Radio, Millimetre Wave and Photonic Super Lattice Engineering), the main objective of which was to research, study and promote artificial electromagnetic materials and metamaterials within the European Union. We have worked in parallel developing these techniques and taking advantage of the wide knowledge of both groups in every research area.

This work was partially supported for project TSI-020100-2010-169 METASINTEESIS granted to a consortium composed by *Aurora Software and Testing S.L.*, and a research institution *Universitat Autònoma de Barcelona* in collaboration with UPV, funded by Spanish Government (*Ministerio de Industria, Turismo y Comercio*) through AVANZA + ID projects [35].

1.2 State of the art

Artificial transmission lines, in particular the resonant-type approach, have a quite short life, a decade approximately [25]. Nevertheless, due to the intense research on the field different resonant particles (SRR, CSRR, OCSRR, OSRR...), many topologies and applications have emerged during this short span. In the next chapter a review is given for completeness, starting from general theory of metamaterials, and going through the most relevant advances in the artificial line applications, but making emphasis in the synthesized lines. Since the main interest is to automate the process, this review of the state of the art is focused on optimization of microwave devices in general, and particularly on artificial transmission lines.

Before the advent of EM field simulators, microwave engineering designs were in general less complex and involved a lot of trial (prototype manufacture) and error (see Fig. 1.7.a). During the 1980s, major companies like Ansoft Corporation (Ansys Inc. at present time), Hewlett-Packard (now Agilent Technologies), and Sonnet Software started to invest lot of resources on the development of simulators for solving complex geometries. At the beginning the practical utilization of EM simulators was limited to design validation, due the long simulation times needed for the analysis of a fixed structure. Anyway since they provided reliable results with good accuracy, a substantial reduction of time (and money, avoiding manufacturing of preliminary prototypes) was conquered. Afterwards, the evolution of EM analysis tools, joined to the increasing speed and memory capacity of modern computers, allow nowadays to solve more complex problems than ever, and made much easier the designer's work (friendly frameworks, visualization tools, shorter computing times, etc.). EM solvers are usually based on one or even on the combined use of several numerical methods at the same time (hybridised), being the most established ones:

- Method of Moments (MoM), as ANSYS DesignerRF [33], Agilent Momentum [36] or Sonnet EM [37]. It is the most typical method used for the analysis and design of planar structures.
- Finite Element Method (FEM), as ANSYS products Maxwell 3D [38] or HFSS [39], or CST Microwave Studio [40]; nowadays both hybridised with other methods such as MoM or finite integration techniques.
- Finite Difference Time Domain (FDTD), as EMPIRE [41].
- Transmission Line Method (TLM), as MEFiSTo [42].

or in the modal analysis area:

- Mode Matching, as μ Wave Wizard of Mician [43].
- Integral Equation, as FEST 3D [44].

No method is generally superior to the others, but they can be more efficient to solve certain problems. But even EM simulators have significantly improved (in terms of code efficiency, hybrid methods, parameterized design variables, integration of optimization tools...) and can accurately model any passive device, they are still very computationally intensive. Hence, they should be combined with other CAD tools to solve complex design problems when direct optimization is unpractical. Typical CAD tools include space mapping [1-2], neural network models [45-46] or genetic algorithm [47-48] among others.

The term Computer Aided Design (CAD) strictly designates any computer system which assists in the creation, modification, analysis, or optimization of a design, so actually an EM solver is a CAD system itself. This term is also used to emphasize that, without those computer processes, obtaining the final design would have had higher cost (time, human, resources) or that would be even unreachable. In most cases the design, which was previously tedious and manual, is now automated as result. The flowchart diagram for a typical CAD process as the one followed in this work is depicted in Fig. 1.7.b.

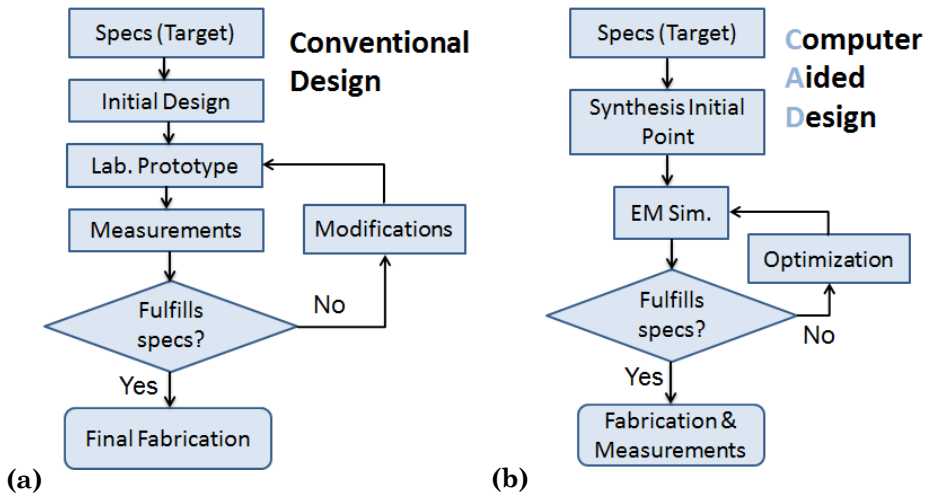


Fig. 1.7. - Flowchart diagram: (a) conventional versus (b) modern (EM-based CAD) microwave design.

The first step of a microwave design is to determine an initial synthesis from certain specs given (usually with well-established equations and/or theoretical models for the considered structure). The determination of the initial point is a key point in the whole CAD-process, because the closer to the final target response the initial layout is, the faster and smoothest the algorithm will converge to the final solution. Moreover, a very bad initial point can lead to the process failure, i.e. not to find any valid solution to the problem. In the next step, the initial synthesis solution is simulated, and right after it is checked if specs are fulfilled or not. In case they are not, an iterative optimization process starts and continues, till a valid solution is found or the maximum number of full-wave simulations (fixed by the user) is reached. Consequently, choosing the most appropriate optimization algorithm is a crucial aspect, since it will have deep impact in the robustness and speed of the whole CAD process. In Chapter 3, this issue will be further discussed.

Nevertheless, due the high cost of EM simulations, techniques which avoid direct optimization like artificial neuronal networks (ANN) or surrogate-based methods as space mapping became popular and are widely used in the microwave field. Neural networks were intensively developed during 1980s, and have been applied to a large number of fields, dating the first reported microwave engineering applications from 1990s. They are computational models inspired by animals' central nervous systems that are capable of machine learning and pattern recognition. In the conventional neuromodeling approach,

the neuromodel is trained such that it approximates the fine model response \mathbf{R}_f in a region of interest for the design parameters x_f and operating conditions ψ , as illustrated in Fig. 1.8.a. The vector w contains the internal parameters of the ANN (weighting factors, bias, etc.). Once the neuromodel is trained with sufficient learning samples (i.e. w is found), it can be used as a fast and accurate model within the region of interest. The fine model responses are typically obtained from an EM simulator, and then if a large amount of training data is needed to ensure model accuracy, process can result very expensive because of the training phase. This is the main drawback of the conventional ANN modelling approach, but different enhancements have arisen trying to minimize this fact. Some solutions proposed by J. E. Rayas [49], that combine space mapping and neuromodels, are worth to mention: Space Mapped Neuromodeling (SMN), Frequency-Dependent Space Mapped Neuromodeling (FDSMN), Frequency Space Mapped Neuromodeling (FSMN), Frequency Mapped Neuromodeling (FMN) and Frequency Partial-Space Mapped Neuromodeling (FPSM). Neural approaches are especially suitable for nonlinear devices.

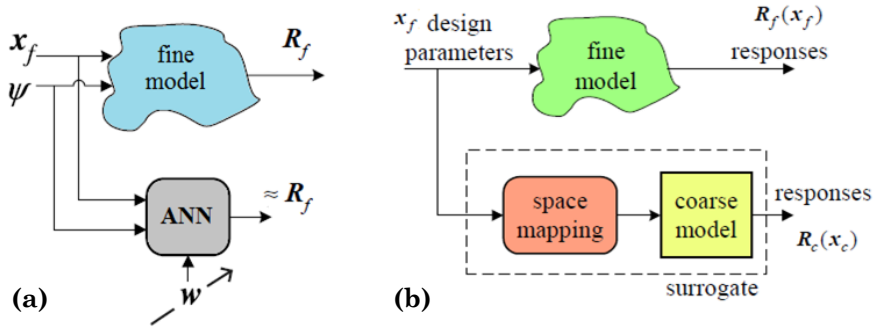


Fig. 1.8. - Conceptual diagram of: Artificial Neural Networks (a) and Space Mapping (b).

Moving now to space mapping, of more interest for this work, it appeared as an innovative and smart way to automate microwave design combining the accuracy of an EM field solver (fine model) with the speed of a circuit simulator (coarse model). The SM technique establishes a mathematical link (P) between the fine model (design/physical) parameter space x_f and the fast coarse model (circuit) parameter space x_c :

$$x_c = P(x_f) \tag{1.1}$$

such that the responses of fine model \mathbf{R}_f and coarse model \mathbf{R}_c are aligned:

$$R_c(x_c) \approx R_f(x_f) \tag{1.2}$$

The coarse model is used for optimization while the fine model is just used for verification or calibration of the coarse model, see Fig. 1.8.b. After firstly proposed in 1994 [50], different approaches to enhance the method are constantly arising [1], being also numerous the applications reported during these years. SM knowledge has also been transferred to industry, proof of that is for example the optimization of dielectric resonator filters and multiplexers at Com Dev [51]. SM is an efficient method, as typically provides solutions in just few iterations (reducing unnecessary, time-consuming full-wave EM simulations) and without need of performing fine model derivatives. More details about this algorithm are given in Chapter 3, but also a wide review about the state of the art of microwave CAD focused on adjoint sensitivity analysis and space mapping can be found in [52]. Adjoint sensitivity is another efficient way to speed up gradient-based optimization methods, and it is currently included in some important commercial EM solvers such as HFFS [39] or CST Microwave Studio [40].

Regarding to EM-based optimization processes in commercial software, OSA90 [53] can be considered the first successful attempt to provide EM solvers with optimization tools. As depicted in Fig. 1.9, an external interface, Empipe [54] was connected to an existing EM solver (e.g. Sonnet EM) with a circuit simulator and the different implemented optimization algorithms in OSA90 (e.g. minimax). It also provided distributed computing capabilities (possibility of run elements in different computers). A practical example to design a bandpass filter can be found in [55]. In 1997 OSA, property of Optimization Systems Associates, was sold to HP (now Agilent) [56], being part of those optimization tools integrated into Momentum [36]. OSA90 carried out also the first implementation of the original space mapping algorithm.

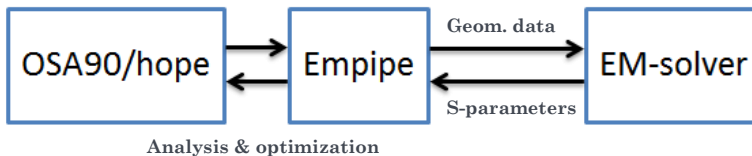


Fig. 1.9. - Block diagram of optimization process with OSA.

Different CAD software tools have integrated SM algorithm approaches. First we will mention DESAFIO, developed at this University (UPV), orientated

toward space industry applications [30]. It is a GUI-based software system based on aggressive space mapping to automate the design process of inductively coupled rectangular waveguide filters. The kernel is implemented in C and FORTRAN language source code, while the graphic interface is programmed in Visual Basic. The EM solver used was an own-developed code based on modal analysis methods (particularly Integral Equation [57]). The same solver is used to evaluate both models, but when used as coarse model a smaller number of modes are considered.

MATLAB™ [58] has also included different optimization toolboxes thanks to the work developed in different research University groups. In 2003, a space mapping optimization toolbox carried out at Technical University of Denmark was integrated [59]. Afterwards (2008), a surrogate modelling toolbox (SUMO toolbox) to automatically build surrogate models (coarse models), this one performed at Gent University [60-61], was generated.

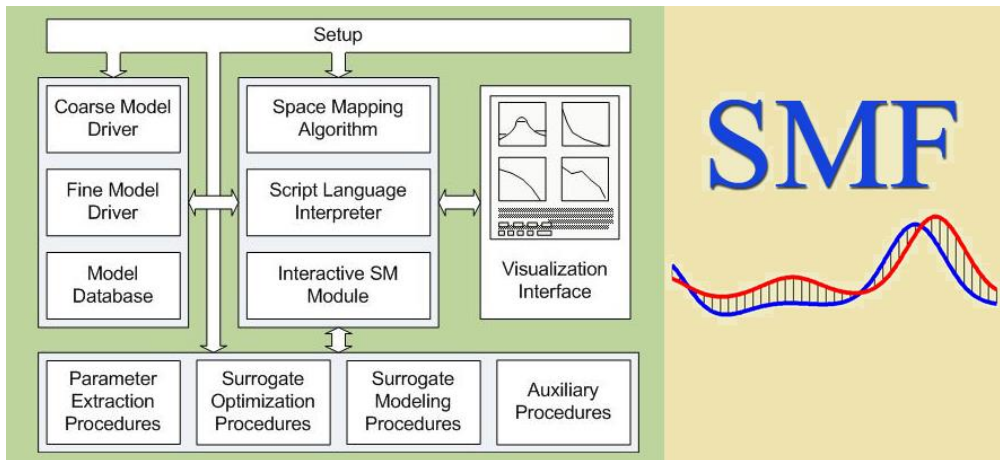


Fig. 1.10. - Block diagram of Space Mapping Framework (SMF) architecture.

Koziel, professor at Reykjavik University, and Bandler, founder of Optimization Systems Associates and intellectual inventor of SM, published the Space Mapping Framework (SMF) in 2006-2007. SMF [62-63] is a user-friendly, GUI-based software system that implements most of the state-of-the-art optimization algorithms and modelling procedures based on space mapping technology: original algorithm, the Broyden-based aggressive space mapping algorithm, various trust region approaches, neural space, and so on. SMF system is a MATLAB-based program, which contains drivers for several

commercial EM solvers (Sonnet em [37], HFSS [39], MEFisSTo [42], Agilent ADS [64]), and circuit simulators (similarly to OSA [53]) allowing the user to include these simulators in an automated optimization loop, and has visualization interfaces, as it can be seen Fig. 1.10.

Changing now to the specific issue of synthesizing artificial transmission lines, it is generally based on the engineer's expertise. Engineer, with the help of EM solvers and curve fitting, tries to find a valid solution. Equivalent circuit models are also commonly used tools, since they constitute a valid approximation in certain frequency range if the particle size is sufficiently small (size much smaller than the operating wavelength). Anyway, having accurate equivalent models for complex structures may be complicated. Only two works oriented to automate this laborious synthesis process were published previously to the realization of this thesis. The first study is the aforementioned work of Roglá et al [34], applied to obtain the design of a coplanar waveguide filter based on split ring resonators. The respective fine and coarse models that characterize the unit cell can be found in Fig. 1.11. A *multi-stage* space mapping technique was used to find the final layout of a periodic 3 cell structure, as well as a statistical approach for parameter extraction (PE). The simulation tools used are the 2.5D electromagnetic commercial software ANSOFT Designer [33] for EM model and the open source Qucs [65] for the circuitual model. Matlab is the computational motor used to interact with the different simulators and process the data.

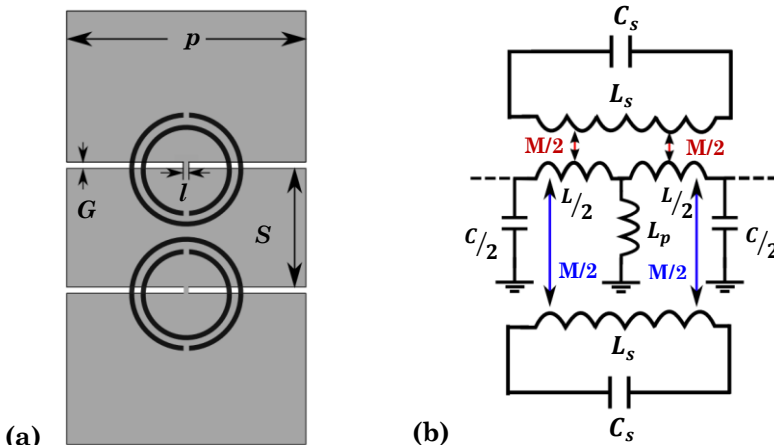


Fig. 1.11. – Fine model (a) and coarse model (b) corresponding to the unit cell of the bandpass filter synthesized in [33]. The SRR design parameters (not indicated in Fig.1.11.a) are: r_m (mean radius), c (rings' width), d (separation between rings), and g (rings' split).

Chapter 1. Introduction

The second work of R. Siragusa et al. [66] uses genetic algorithm (GA) as optimization strategy to synthesize a balanced CRLH structure. One advantage of GA respect to other classical methods (e.g. gradient based) is that they still can achieve good results in cases where the goal function has several local minima or maxima (not necessarily remain stuck), and the function does not need to be continuous or differentiable. This is a very common situation when the number of design parameters is large, and their influence on the value to be optimized can be very complicated, thus having a strongly non-linear behaviour. The unit cell of the design is shown in Fig. 1.12, and its equivalent circuit model.

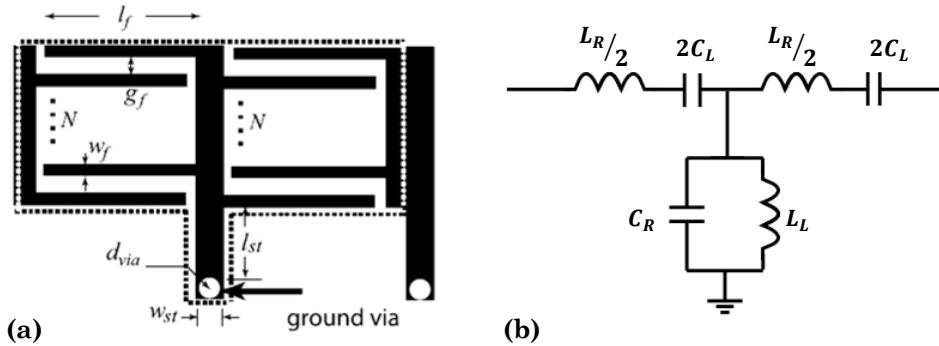


Fig. 1.12. - (a) Layout of the interdigital/stub unit cell. (b) Equivalent circuit model.

The main code is also written in Matlab making use of the available GA toolbox, and generating scripts to control EM solver ANSOFT Designer [33]. The methodology was demonstrated by fabricating and measurement a 6 unit cell prototype. Later on, a refined multi-stage approach was reported by the same authors in [67]. The first optimization was performed by means of a 2.5D solver (ANSOFT Designer [33]), and in the final optimization stage a 3D software CST Microwave Studio [40] was used instead.

During the realization of this PhD thesis, some other works over the same field (i.e. the automated synthesis of artificial TLs) have been published:

- Adjoint-accelerated space mapping and direct optimization to implement flat lens transmission line [68].
- GA to the design CRLH TL in coplanar waveguide technology [69].
- Aggressive space mapping with model-trust region algorithm [70] applied to complementary split-ring resonator (CSRR)-loaded transmission lines, which had already been previously solved based on the work performed at the beginning of the thesis [71].

The final goal of this work is to demonstrate that applying SM techniques is a suitable and an advantageous technique to synthesize artificial transmission lines, which has already been widely used to obtain other passive devices such as planar filters. The main advantage of this methodology is to minimize the whole design process cost (both human and computational). Different efforts to increase the robustness of the methods have been carried out. Some contacts with the industry of commercial EM software tools were made, and they have shown interest in the development of these techniques to have an advantage position in the market.

1.3 Thesis Structure

The present PhD thesis work is divided into five chapters as follows:

- Chapter 1: An overview of the different transmission lines at microwave domain is given. Then, the work is placed into context, and the motivation or interest of finding an autonomously or semi-autonomously way to synthesize artificial transmission lines is highlighted.
- Chapter 2: It begins with a short introduction to metamaterials and their main characteristic properties. Next, the focus is turned to artificial transmission lines based on MTMs, making special emphasis on the lines considered in this work, i.e. those based on the resonant approach. Hence the main resonant particles are introduced, and also main applications are presented
- Chapter 3: a general overview about optimization process, with special interest on space mapping techniques, is given. Next, the application of aggressive space mapping to the considered MTM unit cells is described. Even the general methodology does not change, every unit cell requires particular study and has its peculiarities. Different attempts to provide more robustness to the algorithm are also reported (line search and a two-step approach).
- Chapter 4: Practical applications related to the synthesis of different prototypes, including their fabrication and measurement, are shown in order to validate the design methodology proposed in this work.
- Chapter 5: Summary of the results deriving from the presented research, and introduction of the potential future developments.

Note that the references (listed in order of appearance) are placed at the end of every chapter, and not as a full list at the end of the whole document.

References

- [1] J. W. Bandler, Q. Cheng, S. A. Dakroury, A. S. Mohamed, M. H. Bakr, K. Madsen, and J. Søndergaard, "Space mapping: The state of the art," *IEEE Transactions on Microwave Theory and Techniques*, vol. 52, no. 1, pp. 337–361, Jan. 2004.
- [2] Q. S. Cheng, S. Koziel and J. W. Bandler, "Simplified space mapping approach to enhancement of microwave device models," *Int. J. RF and Microwave Computer-Aided Eng.* Vol. 16, no. 5, 518–535, Sept. 2006.
- [3] D. M. Pozar, *Microwave Engineering*, John Wiley & Sons, 3rd ed., 2005.
- [4] C. Caloz and T. Itoh, *Electromagnetic Metamaterials: Transmission Line Theory and Microwave applications: The Engineering Approach*, Wiley-IEEE Press, 2006.
- [5] G. Eleftheriades and K. Balmain, *Negative-refraction metamaterials: fundamental principles and applications*. Wiley-IEEE Press, 2005
- [6] N. Engheta and R. Ziolkowski, *Metamaterials: Physics and Engineering Explorations*. Wiley-IEEE Press, 2006
- [7] R. Marqués, F. Martín and M. Sorolla, *Metamaterials with negative parameters*, Wiley, 2008.
- [8] G. Ruvio, P-S. Kildal and S. Maci, "Modal propagation in ideal soft and hard waveguides," *IEEE Antennas and Propagation Society International Symposium*, vol. 4, pp. 438-441, June 2003.
- [9] F-R. Yang, K-P. Ma, Y. Qian, and T. Itoh, "A novel TEM waveguide using uniplanar compact photonic-bandgap (UC-PBG) structure," *IEEE Transactions on Microwave Theory and Techniques*, vol. 47, no. 11, pp. 2092-2098, Nov. 1999.
- [10] P-S. Kildal, S. Maci, A. Valero-Nogueira, A. Kishk and E. Rajo-Iglesias, "The Gap Waveguide as a Metamaterial-based Electromagnetic Packaging Technology Enabling Integration of MMICs and Antennas up to THz," *Proceedings of the 5th European Conference on Antennas and Propagation*, pp. 3715–3718, April 2011.
- [11] E. Alfonso, A. Valero-Nogueira, J. Herranz, and D. Sánchez, "Oversized waveguides for TEM propagation using hard surfaces," *IEEE Antennas and Propagation Society International Symposium*, pp. 1193-1196, July 2006.
- [12] A. Valero-Nogueira, E. Alfonso, J. Herranz, and M. Baquero, "Planar slot-array antenna fed by an oversized quasi-TEM waveguide," *Microwave and Optical Technology Letters*, vol. 49, no. 8, pp. 1875-1877, May 2007.

- [13] E. Pucci, A. U. Zaman, E. Rajo-Iglesias, and P-S. Kildal, "New low loss inverted microstrip line using gap waveguide technology for slot antenna applications," Proceedings of the 5th European Conference on Antennas and Propagation, pp. 979-982, April 2011.
- [14] E. Rajo-Iglesias and P-S. Kildal, "Groove gap waveguide: A rectangular waveguide between contactless metal plates enabled by parallel-plate cut-off," Proceedings of the 4th European Conference on Antennas and Propagation, pp. 1-4, April 2010.
- [15] Per-Simon Kildal, "Waveguides and transmission lines in gaps between parallel conducting surfaces", PCT/EP2009/057743 submitted 2009-06-22.
- [16] H. Uchimura, T. Takenoshita and M. Fujii, "Development of a laminated waveguide," IEEE Transactions on Microwave Theory and Techniques, vol. 46, no. 12, pp. 2438-2443, Dec. 1998.
- [17] D. Deslandes and K. Wu, "Integrated microstrip and rectangular waveguide in planar form," IEEE Microwave and Wireless Components Letters, vol. 11, no. 2, pp. 68-70, Feb. 2001.
- [18] A. K. Iyer and G. V. Eleftheriades, "Negative refractive index metamaterials supporting 2-D waves," IEEE MTT-S International Microwave Symposium Digest, vol. 2, pp. 1067- 1070, June 2002.
- [19] A. A. Oliner "A periodic-structure negative-refractive-index medium without resonant elements," IEEE MTT-S International Microwave Symposium Digest, vol. 1, pp. 191-194, June 2003.
- [20] C. Caloz and T. Itoh, "Application of the transmission line theory of left-handed (LH) materials to the realization of a microstrip LH transmission line," IEEE Antennas and Propagation Society International Symposium, pp. 412-415, June 2002.
- [21] D. Sievenpiper, L. Zhang, R. F. J. Broas, N. G. Alexopolous, and E. Yablonovitch "High-impedance surface electromagnetic surfaces with a forbidden frequency band," IEEE Transactions on Microwave Theory and Techniques, vol. 47, no. 11, pp. 2059-2074, Nov. 1999.
- [22] C. Caloz, "Dual Composite Right/Left-Handed (D-CRLH) Transmission Line Metamaterial," IEEE Microwave and Wireless Components Letters, vol. 16, no. 11, pp. 585-587, Nov. 2006.
- [23] A. Rennings, S. Otto, J. Mosig, C. Caloz and I. Wolff, "Extended Composite Right/Left-Handed (E-CRLH) Metamaterial and its Application as Quadband Quarter-Wavelength Transmission Line," Microwave Conference Asia Pacific, pp. 1405-1408, Dec. 2006.

- [24] G. V. Eleftheriades, “Design of generalized negative-refractive-index transmission lines for quad-band applications,” *IET Microwave Antennas and Propagation*, vol. 4, no. 8, pp. 977–981, Aug. 2010.
- [25] F. Martín, F. Falcone, J. Bonache, R. Marques and M. Sorolla, “A new split ring resonator based left handed coplanar waveguide”, *Applied Physics Letters*, vol. 83, no. 22, pp. 4652-4654, Dec. 2003.
- [26] J. Bonache, J. Martel, I. Gil, M. Gil, F. Martín, I. Cairo and M. Ikeda, “Super compact ($<1\text{cm}^2$) band pass filters with wide bandwidth and high selectivity at C band”, *Proceedings of the 36th European Microwave Conference*, pp. 599-602, Sept. 2006.
- [27] M. Gil, J. Bonache, I. Gil, J. García-García, and F. Martín, “Miniaturization of planar microwave circuits by using resonant-type left handed transmission lines,” *IET Microwave Antennas and Propagation*, vol.1, pp. 73-79, Feb. 2007.
- [28] M. Gil, J. Bonache, J. Selga, J. García-García, and F. Martin “High-pass filters implemented by composite right/left handed (CRLH) transmission lines based on complementary split rings resonators (CSRRs),” *PIERS Online* Vol. 3, no. 3, pp. 251-253, Jan. 2007.
- [29] A. Belenguer, J. Cascon, A. L. Borja, H. Esteban and V. E. Boria, “Dual composite right-/left-handed coplanar waveguide transmission line using inductively connected split-ring resonators,” *IEEE Transactions on Microwave Theory and Techniques*, vol.60, no.10, pp.3035-3042, Oct. 2012.
- [30] J. V. Morro, H. Esteban, P. Soto, A. A. San Blas, V. E. Boria, and B. Gimeno “DESAFIO 1.0: A novel CAD tools for the automated design of inductively coupled rectangular waveguide filters”, *Proceedings of PIERS*, July 2002.
- [31] J. V. Morro, “Nuevas Estrategias de Diseño Automatizado de Componentes Pasivos para Sistemas de Comunicaciones de Alta Frecuencia”, PhD Thesis, Universitat Politècnica de València, 2011.
- [32] E. Diaz, “Efficient Analysis and Design of Devices in Substrate Integrated Waveguide (SIW) Technology”, PhD Thesis, Universitat Politècnica de València, 2013.
- [33] ANSYS DesignerRF and Nexxim 8.0, Ansys, Inc., Canonsburg, PA USA.
- [34] L. J. Roglá, J. E. Rayas-Sánchez, V. E. Boria and J. Carbonell, “EM-based space mapping optimization of left-handed coplanar waveguide filters with split ring resonators,” *IEEE MTT-S International Microwave Symposium Digest*, pp. 1241– 1244, June 2007.
- [35] Project TSI-020100-2010-169 METASINTESIS. Project Title: “Investigación y desarrollo de una herramienta CAD para la síntesis de circuitos compactos y

de altas prestaciones basados en metamateriales”, Ministerio de Industria, Turismo y Comercio, 2010-2012.

[36] Agilent Momentum, Agilent Technologies, Santa Rosa, CA USA.

[37] Sonnet em, Version 14.0, Sonnet Software, Inc., North Syracuse, NY USA.

[38] ANSYS Maxwell 3D, version 15.0, Ansys, Inc., Canonsburg, PA USA.

[39] ANSYS HFSS (High Frequency Structure Simulator), version 15.0, Ansys, Inc., Canonsburg, PA USA.

[40] CST Microwave Studio Suite, CST AG, Darmstadt, Germany.

[41] EMPIRE XCell™, IMST GmbH, Kampt-Linfort, Germany.

[42] MEFiSTo-3D Pro (Multipurpose Electromagnetic Field Simulation Tool), version 4.0, Faustus Scientific Corporation (Now ^{EM} Integrity), Victoria, BC, Canada.

[43] μ Wave Wizard· Version 7, Mician GmbH, Bremen, Germany.

[44] FEST-3D Version 6, AURORASAT S.L., Valencia, Spain.

[45] J. E. Rayas-Sanchez, “EM-based optimization of microwave circuits using artificial neural networks: the state-of-the-art,” *IEEE Transactions on Microwave Theory and Techniques*, vol. 52, no.1, pp. 420-435, Jan. 2004.

[46] H. Kabir, Y. Wang, M. Yu, and Q.J. Zhang, “Efficient neural network modeling techniques for applications in microwave filter design,” *IEEE Transactions on Microwave Theory and Techniques*, vol. 56, pp. 867–879, April 2008.

[47] V.M. Kureichik, S.P. Malioukov, V.V. Kureichik and A.S. Malioukov, “Genetic Algorithms for Applied CAD Problems”, Springer, Series: Studies in Computational Intelligence, vol. 212, 2009.

[48] G. Renner and A. Ekárt, “Genetic algorithms in computer aided design,” *Computer-Aided Design (ELSEVIER)*, vol. 35, issue 8, pp. 709-726, July 2003.

[49] J. E. Rayas-Sánchez, “Neural Space Mapping Methods for Modeling and Design of Microwave Circuits”, PhD Thesis, McMaster University, Canada, June 2001.

[50] J.W. Bandler, R.M. Biernacki, S.H. Chen, P.A. Grobelny and R.H. Hemmers, “Space mapping technique for electromagnetic optimization”, *IEEE Transactions on Microwave Theory and Techniques*, vol. 42, pp. 2536-2544, Dec. 1994.

Chapter 1. Introduction

- [51] M.A. Ismail, D. Smith, A. Panariello, Y. Wang and M. Yu, "EM based design of large-scale dielectric resonator multiplexers by space mapping," IEEE MTT-S International Microwave Symposium Digest., vol.1, pp.291-294, June 2003.
- [52] Q. S. Cheng, J. W. Bandler, S. Koziel, M. H. Bakr and S. Ogurtsov, "The state of the art of microwave CAD: EM-based optimization and modeling," International Journal of RF and Microwave Computer-Aided Engineering, vol.5, pp. 475-491, Sept. 2010.
- [53] OSA90/hope™, Optimization Systems Associates Inc. (now Agilent Technologies), Dundas, Ontario, Canada.
- [54] EMPIPE™, Optimization Systems Associates Inc. (now Agilent Technologies), Dundas, Ontario, Canada.
- [55] D. G. Swanson, "Optimizing a microstrip bandpass filter using electromagnetics". Int. J. Microw. Mill.-Wave Comput.-Aided Eng., vol. 5, no. 5, pp. 344-351, Sept. 1995.
- [56] John Bandler's Technical Achievement Milestones:
<http://www.bandler.com/mileston2.htm>
- [57] G. Gerini and M. Guglielmi, "Efficient integral equation formulations for admittance or impedance representation of planar waveguide junctions," IEEE MTT-S International Microwave Symposium Digest, vol. 3, pp.1747-1750, June 1998.
- [58] MATLAB, MathWorks, Natick Massachusset, USA.
- [59] Space Mapping Toolbox for MATLAB. Available in:
http://www2.imm.dtu.dk/~kajm/Space_Mapping_Toolbox.html
- [60] Surrogate Modeling (SUMO) Toolbox for MATLAB. Available in:
<http://www.sumo.intec.ugent.be/SUMO>
- [61] D. Gorissen, K. Crombecq, I. Couckuyt, T. Dhaene and P. Demeester, "A Surrogate Modeling and Adaptive Sampling Toolbox for Computer Based Design", Journal of Machine Learning Research, Vol. 11, pp. 2051-2055, July 2010.
- [62] SMF, ver. 0.9.1, Bandler Corporation, 2007.
- [63] S. Koziel and J.W. Bandler, "SMF: A user-friendly software engine for space-mapping-based engineering design optimization," in Proc. Int. Symp. Signals, Systems and Electronics, pp. 157-160, Montreal, Canada, July 2007.
- [64] Agilent ADS (Advanced Design System), Agilent Technologies, Santa Rosa, CA USA.

- [65] Qucs (Quite Universal Circuit Simulator), <http://qucs.sourceforge.net>, Qucs team, 2006.
- [66] R. Siragusa, H.V. Nguyen, E. Perret, P. Lemaitre-Auger, S. Tedjini and C. Caloz, "Automated design of CRLH structures using co-design synthesis computational approach", Asia-Pacific Microwave Conference, pp. 830-833, Dec. 2009.
- [67] R. Siragusa, E. Perret, H.V. Nguyen, P. Lemaitre-Auger, S. Tedjini and C. Caloz, "Control of the sensitivity of CRLH interdigital microstrip balanced structures using a co-design genetic algorithm approach", Applied Physics A, vol. 103, issue 3, pp. 709-714, June 2011.
- [68] A. Khalatpour, R.K. Amineh, Q.S. Cheng, J. W Bandler and N.K. Nikolova, "Adjoint-accelerated design framework for novel materials in microwave applications", Proceedings of the 41st European Microwave Conference, pp. 440-443, Oct. 2011.
- [69] X. Chen, C. Yin and C. Guan, "Design and optimization of CPW-based composite right/left-handed transmission line," International Journal of RF and Microwave Computer-Aided Engineering, vol. 21, pp. 421-431, July 2011.
- [70] P. J. Bradley, "Quasi-newton model-trust region approach to surrogate-based optimisation of planar metamaterial structures," Progress In Electromagnetics Research B, Vol. 47, pp. 1-17, 2013.
- [71] A. Rodriguez, J. Selga, M. Gil, J. Carbonell, V.E. Boria and F. Martin, "Automated synthesis of resonant-type metamaterial transmission lines using aggressive space mapping," IEEE MTT-S International Microwave Symposium Digest, pp. 209-212, May 2010.

CHAPTER 2

Metamaterials (MTMs)

2.1 General overview

2.2 Transmission lines based on MTM concepts

2.2.1 Resonant Approach

2.2.1.1 TLs based on SRRs

2.2.1.2 TLs based on CSRRs

2.2.1.3 TLs based on OSRRs and OCSRRs

References

*“If you are not willing to risk the unusual,
you will have to settle for the ordinary”*

Jim Rohn



2 METAMATERIALS

Metamaterials (MTMs) is a research topic which has attracted lot of attention in fields like physics and engineering, and still does. The growing interest on those materials, at the beginning of last decade, can be explained by the concurrence of different facts: first physical realization of a negative refraction material [1], their great potential applications (miniaturization of components, transparency, scattering properties, etc.), interesting novel contributions [2-4], and the development of micro-nanofabrication technologies. Nevertheless, the history of metamaterials can be traced back to the late part of the nineteenth century, when Bose published his work on the rotation of plane of polarization of electric waves by some twisted structures known nowadays as chiral structures [5]. But probably the most important seminal work is Veselago's paper [6], where he already predicts the possibility of materials which present simultaneously negative permittivity (ϵ) and permeability (μ), and as result show a negative refractive index (n). In that context, he introduces the term "left-handed" (LH) media, in order to refer to those materials where the electric and magnetic fields propagate in a direction opposite (backwards) to the conventional one, which is given by the left-handed rule (Poynting vector (\vec{P}) with opposite sign to the wave vector (\vec{k})), see Fig. 2.1. The nomenclature "metamaterial" is much more recent, dates from 1999, and it is attributed to Walser [7]. The prefix "meta" is a Greek term which means beyond, and emphasizes the fact that this field involves investigation beyond the limits of conventional materials. Anyway it is worth mentioning, that, even LH structures lie under the category of MTM, and they are probably the most popular ones; there are others engineered materials which are MTMs as well, and have only one of the two constitutive parameters (i.e. ϵ , μ) negative, present anisotropy, etc. As mentioned in Chapter 1 there is not a common standardized nomenclature, definition or classification for MTMs. This is a clear indicator of the complexity to unify criteria (different areas involved) and the controversy generated in different fields like microwave engineering. However, as time goes by and technology is more mature, reticence is smaller and main concepts are well established [8-11], and more unified criteria are available. Anyway, it is a subject under development with a lot of potential and multiple applications to offer [12].

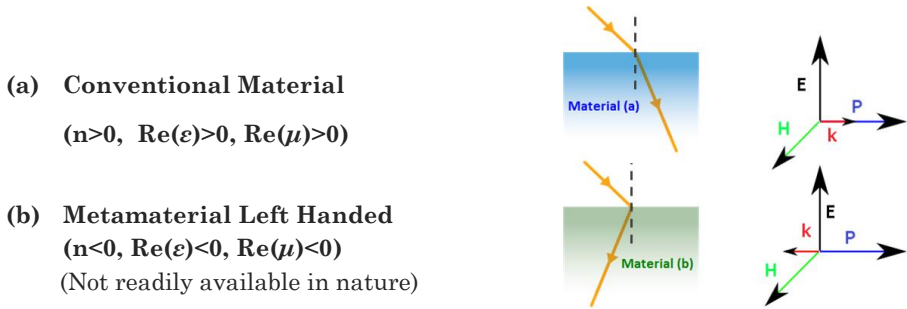


Fig. 2.1. - Conventional materials versus LH MTMs: light refracted by the material; orientation of the different vectors: electric field E, magnetic field H, Poynting vector P and wave vector k. Re() indicates real part.

2.1 General Overview

A metamaterial can be described as an artificially structured material which attains its properties from the unit structure rather than from constituent materials. Those novel properties not readily available in nature and not observed in the constituent materials are, but not limited to, negative refraction, negative permittivity and/or permeability, negative polarization and near-zero relative material parameters, in certain frequency bands. The unconventional response functions of these metamaterials are often generated by artificially fabricated inclusions or inhomogeneities embedded in a host medium, or connected to or embedded on a host surface [9], see Fig. 2.2.

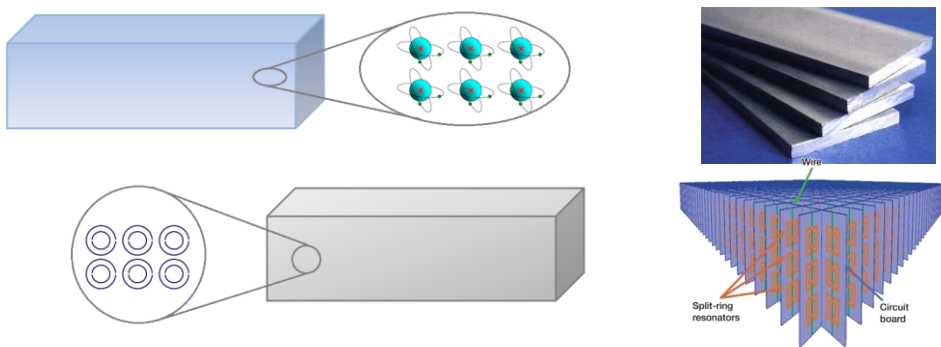


Fig. 2.2. - Conventional materials (properties derive from constituent atoms) versus metamaterials (properties derive from their constituent units).

It can be said that metamaterials are, above all, man-made materials, custom created to fulfil a given specs as for example certain given index of

refraction (hyperlenses). Most reported MTMs do follow a certain periodicity, but there are also some random composites -not periodic- which might be considered too, due to their electromagnetic responses [10].

The study of metamaterials is often related to the control of electromagnetic waves (optical and microwave regime), but it should not be forgotten those metamaterials which deal with acoustic waves [13-14]. The acoustic wave is longitudinal (defined by the pressure and particle velocity), while the electromagnetic wave is transverse (defined by the electric and magnetic fields), however they present similarities as it will be explained later.

James Maxwell in the 1800's demonstrated that light, magnetism, electricity are manifestations of the same phenomenon: electromagnetic fields. He formulated the equations describing the EM wave propagation within a material. Assuming an isotropic media at least for a given polarization of the electric (\vec{E}) and magnetic (\vec{H}) fields in a specific range of frequencies, relation between them can be expressed as:

$$\nabla \times \vec{E} = -\mu \cdot \frac{\partial \vec{H}}{\partial t} \quad (2.1)$$

$$\nabla \times \vec{H} = \varepsilon \cdot \frac{\partial \vec{E}}{\partial t} \quad (2.2)$$

It can be rewritten in the phasor form as:

$$\nabla \times \vec{E} = -j\omega\mu\vec{H} \quad (2.3)$$

$$\nabla \times \vec{H} = j\omega\varepsilon\vec{E} \quad (2.4)$$

Therefore, the constitutive parameters of a medium/material are considered the permittivity and permeability, and depending on the characteristics of the medium/material can be real (lossless) or complex, scalar (isotropic) or matrix, constant (homogeneous) or variable. Traditionally, these parameters have been considered to be positive real or complex quantities, but it is possible to design materials whose effective permittivity and/or permeability may exhibit negative real parts, in several frequency regimes. In the complex form, the most common notation of these parameters is:

$$\varepsilon = \varepsilon' - j\varepsilon'' = \varepsilon_0\varepsilon_r - j\varepsilon'' \quad (2.5)$$

$$\mu = \mu' - j\mu'' = \mu_0\mu_r - j\mu'' \quad (2.6)$$

where ε_0, μ_0 are the values of the permittivity and the permeability of free-space, the superscript prime stands for real part and the double prime for imaginary part. The real part represents how much energy is stored in a material from an external field, which is also characterized by given the corresponding relative value (ε_r, μ_r). The imaginary part ε'' , also known as the loss factor, can be a measure of how dissipative/lossy a material is to an external field.

The index of refraction is a magnitude of common use in optics, and is defined as the ratio of the phase velocity of a wave in vacuum (c) and the phase velocity (v_p) in the medium itself:

$$n = \frac{c}{v_p} \quad (2.7)$$

with:

$$v_p = \frac{\omega}{\beta} \quad (2.8)$$

where β is the phase constant, and ω the angular frequency of the wave. In the case of light:

$$n^2 = \varepsilon\mu \quad (2.9)$$

Most of materials in nature are characterized by a passive nature and a refractive index (n) equal or greater than the free space value. In the case of acoustics, the refractive index is defined as function of bulk modulus (K) and density (ρ) as follows:

$$n^2 = \frac{\rho}{K} \quad (2.10)$$

Hence, the inherent parameters for an acoustic media are: K and ρ . Different analogies between acoustic and EM variables can be established [13], as it can be observed in Table 2.1 (2D cylindrical Maxwell equations are also a solution to the 2D acoustic equations).

Table 2. 1. - ANALOGY BETWEEN ACOUSTIC AND ELECTROMAGNETIC VARIABLES AND MATERIAL CHARACTERISTICS.

Acoustics	EM (TE)	Analogy
$j\omega\rho_\phi v_\phi = -\frac{1}{r}\frac{\partial p}{\partial\phi}$	$j\omega\mu_r(-H_r) = -\frac{1}{r}\frac{\partial(-E_z)}{\partial\phi}$	
$j\omega\rho_r v_r = -\frac{\partial p}{\partial r}$	$j\omega\mu_\phi H_\phi = -\frac{\partial(-E_z)}{\partial r}$	
$j\omega\frac{1}{K}p = -\frac{1}{r}\frac{\partial(rv_r)}{\partial\phi} - \frac{1}{r}\frac{\partial v_\phi}{\partial\phi}$	$j\omega\varepsilon_z(-E_z) = -\frac{1}{r}\frac{\partial(rH_\phi)}{\partial r} - \frac{1}{r}\frac{\partial(-H_r)}{\partial\phi}$	
Acoustic pressure p	Electric field E_z	$-E_z \leftrightarrow p$
Particle velocity v_ϕ, v_r	Magnetic field H_ϕ, H_r	$H_\phi \leftrightarrow v_r$ $-H_r \leftrightarrow v_\phi$
Dynamic density ρ_r, ρ_ϕ	Permeability μ_r, μ_ϕ	$\mu_\phi \leftrightarrow \rho_r$ $\mu_r \leftrightarrow \rho_\phi$
Dynamic bulk modulus K	Permittivity ε_z	$\varepsilon_z \leftrightarrow 1/K$

The first acoustic metamaterial, called locally resonant sonic material was demonstrated in 2000 [14]. However, the first physical implementation of a structure with both constitutive negative parameters of an acoustic MTM is from 2007 [15].

According to the value of the real part of ε and μ , materials are classified as follows:

- Double Positive (DPS): both permittivity and permeability real parts are greater than zero; most of materials are under this nomenclature, being by far the most studied ones.
- Double Negative (DNG) or left handed (LH): both permittivity and permeability real parts are smaller than zero, being the resulting index of refraction a real number. Double negative and double positive materials support monochromatic plane-wave propagation, but DNG describes backward propagation since phase and group velocity have opposite sign, wave number \vec{k} is negative. Other peculiar properties that DNG materials exhibit are: negative refraction, reversal of Čerenkov radiation or Doppler shift.

Chapter 2. Metamaterials

- Single Negative (SNG): only ϵ' or μ' is negative. They just support evanescent waves (wave number is pure imaginary, as it is also n). There are divided in two main kinds: “ ϵ -negative” (ENG), and “ μ -negative” (MNG).
- Materials where the real part of one of the parameters is near zero are known as “ ϵ -near-zero” (ENZ) or “ μ -near-zero” (MNZ) materials (located near the two axes of Figure 2.3). If we compare them to negative-index materials, they may have relatively larger bandwidth of operation and presenting lower losses.

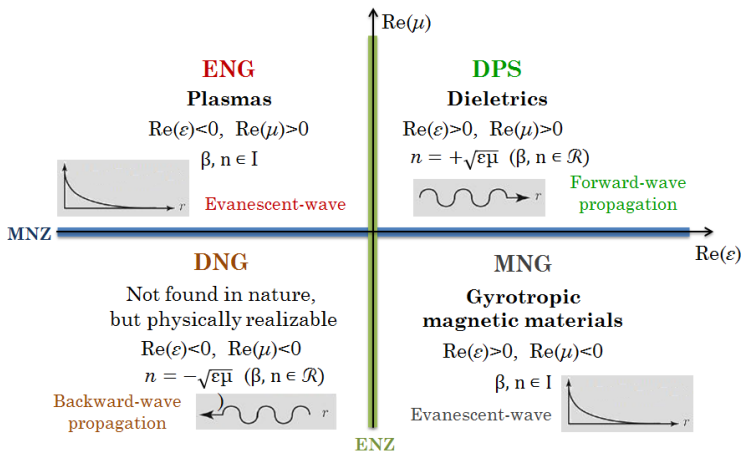


Fig. 2.3. - Classification of materials based on the permittivity (ϵ) and permeability (μ). $\text{Re}()$ indicates real part.

Similar classification could be done attending this time to the values of the bulk modulus and density, see the following figure:

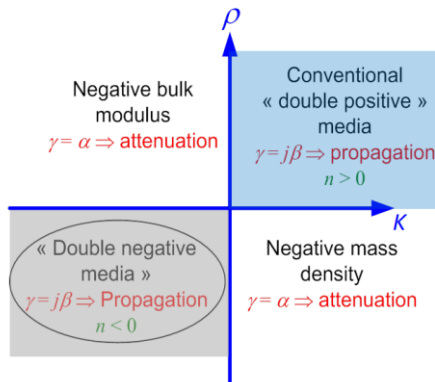


Fig. 2.4. - Classification of materials based on bulk modulus (K) and density values (ρ). $\gamma = \alpha + j\beta$ is the propagation constant (see section 2.2).

Electromagnetic MTMs are often classified as SNG or DNG, and depending on the working frequency, electromagnetic band gap materials (EBG) are included under this nomenclature too [9, 16]. If the effective-homogeneity condition is a requirement, i.e. the involved elements and distances between them are much smaller than a wavelength at the frequencies of interest, they will be considered as metamaterials, otherwise not. Actually, in an EBG the periodicity distances can be on the order of half the wavelength or even more, depending on the case, so in that case they cannot be considered as MTMs.

EBG structures exhibit frequency bands within which the waves are highly attenuated and the propagation is prohibited. While SNG or DNG media can be described by homogenization and effective media concepts, EBG are described by the Bragg reflection and other periodic media concepts as the Brillouin diagram, where the lattice topology plays a crucial role. The Brillouin diagram is employed to represent the dispersion characteristics of EBG materials, and is also an indirect way to determine the possible stop-bands between propagating modes. In general, they are periodic planar structures easy to fabricate on regular printed circuit board (PCBs), or on integrated circuit substrates. Some of the most common techniques used to fabricate planar MTMs are: milling and drilling, contact photolithography and electron beam lithography (for smaller and more detailed structures). EBG materials have been successfully applied to improve the behaviour of many microwave devices such as: spurious suppression in band-pass filters, optimization of the radiation pattern in microstrip antennas, and so on. Some of the many practical or potential applications of metamaterials are listed next:

- Cloaking. The term EM cloaking refers to the reduction of the total scattering cross section of an object, meaning in the ideal case that the object is made invisible to the impinging EM radiation [17]. It is based on the theory of transformation optics and quasi-conformal mapping, being similar concepts also extrapolated to the acoustic field. Cloaking presents several potential applications particularly from a military point of view (invisible planes, sonar blocking, and communications), but also sound proof rooms. The first experimental demonstration in the microwave field was performed in 2006 [18], and for the acoustic domain in 2008 [19]. Early systems were necessarily large, valid just for small objects and within the two dimensional limit, but many efforts towards the real application stage are being performed since then [20].

- Super lenses or hyperlenses [21] are lenses that use negative refractive index property to go beyond the diffraction limit. They have exciting potential in many areas of science and technology, such as: optical “nanoscope” (to extend the optical microscope into the nanometre scale), optical lithography to ultra-small scales, high-resolution clinical ultrasound imaging or improving underwater sonar sensing. Some breakthroughs in demonstration of the super-lensing effect have been already performed [22-24], but this technology is still on the path to real applications.
- Miniaturization: reducing antenna size or other microwave devices [25-27].
- Improvement of existing devices (better performance or providing novel functionalities): enhancement of antenna performance (i.e. suppressing surface waves [9]), spurious suppression in band-pass filters [28] among others.

2.2 Transmission Lines Based on MTM Concepts

The conventional transmission lines used in practice (microstrip, CPW, etc.) are homogeneous transmission media that exhibit a RH behaviour (phase and group velocity have positive values). They can be approximately described by a lumped-element circuit with series inductance and shunt capacitance when physical dimensions are much smaller than the wavelength, λ . The equivalent circuit for the lossless case is shown in Fig. 2.5.a.

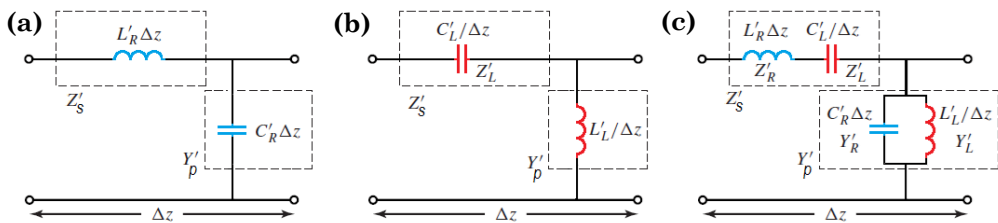


Fig. 2.5. - Simplified lumped-element equivalent circuit for: (a) RH TL; (b) LH TL; (c) CRLH-TL with L'_R, C'_R, L'_L and C'_L per-unit-length quantities.

The complex propagation constant in that line (γ), can be obtained from the distributed value of the series impedance Z'_s and the shunt admittance Y'_p as follows:

$$\gamma = \alpha + j\beta = \sqrt{Z'_s \cdot Y'_p} \quad (2.11)$$

where α and β are the attenuation and dispersion constant respectively. In this particular case α is zero (lossless media) and β results:

$$\beta_R = \omega \sqrt{L'_R C'_R} \quad (2.12)$$

where ω is the angular frequency, and L'_R and C'_R are the series inductance and shunt capacitance per unit length. The subscript R just indicates that is referred to the right-handed line, and the prime is used to emphasize the fact that it is a distributed magnitude. The wavelength is defined as follows:

$$\lambda = \frac{2\pi}{\beta} \xrightarrow{\text{yields}} \lambda_R = \frac{2\pi}{\omega \sqrt{L'_R C'_R}} \quad (2.13)$$

The line exhibits a forward transmission, since the phase velocity, v_p , and the group velocity, v_g are both positive:

$$v_p = \frac{\omega}{\beta} \xrightarrow{\text{yields}} v_{p,R} = \frac{1}{\sqrt{L'_R C'_R}} \quad (2.14)$$

$$v_g = \left(\frac{\partial\beta}{\partial\omega}\right)^{-1} \xrightarrow{\text{yields}} v_{g,R} = \frac{1}{\sqrt{L'_R C'_R}} \quad (2.15)$$

In addition, the index of refraction is positive too, calculated according to (2.7) is:

$$n_R = c \cdot \sqrt{L'_R C'_R} \quad (2.16)$$

The dual of a conventional transmission line, should be characterized by a series capacitance and a shunt inductance as illustrated in Fig. 2.5.b (for the lossless case). The dispersion constant is given then by:

$$\beta_L = -\frac{1}{\omega \sqrt{L'_L C'_L}} \quad (2.17)$$

As a result, the phase and group velocities have opposite signs:

$$v_{p,L} = -\omega^2 \sqrt{L'_L C'_L} \quad (2.18)$$

$$v_{g,L} = +\omega^2 \sqrt{L'_L C'_L} \tag{2.19}$$

and the index of refraction is negative:

$$n_L = -\frac{c}{\omega^2 \sqrt{L'_L C'_L}} \tag{2.20}$$

In other words, the line presents a backward transmission, i.e. a left-handed behaviour (LH). The subscript L is used in the previous expressions to distinguish the characteristic parameters of the LH-TL. The dispersion diagrams (also called $\omega - \beta$ diagrams) corresponding to the previous lines are shown in Fig. 2.6.

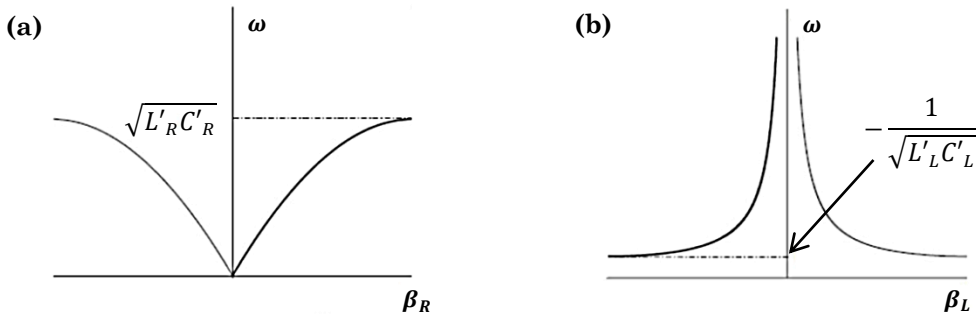


Fig. 2.6. - Dispersion diagrams: (a) RH TL (b) LH TL; with L'_R, C'_R, L'_L and C'_L per-unit-length quantities.

Making again the analogy between the propagation of a plane wave in a homogeneous and isotropic material, with the propagation in a transmission line and mapping the Telegrapher's equations and Maxwell equations, it follows:

$$Z'_s = j\omega\mu \tag{2.21}$$

$$Y'_p = j\omega\varepsilon \tag{2.22}$$

The sign of the series impedance and shunt inductance, is actually determining the sign of the constitutive parameters (i.e. ε, μ). As a consequence, TL can be classified following the same criteria used in previous section: DPS (conventional), SNG, and DNG (LH). The effective permittivity and permeability of pure RH and LH, can be approximated by:

$$\varepsilon_R = C'_R \qquad \mu_R = L'_R \qquad (2.23)$$

$$\varepsilon_L = -\frac{1}{\omega^2 L'_L} \qquad \mu_L = -\frac{1}{\omega^2 C'_L} \qquad (2.24)$$

As expected, both sign parameters are defined positive (DPS or RH-TL) or negative (DNG or LH-TL). The characteristic impedance Z_c can also be calculated:

$$Z_c = \frac{Z'_s}{\gamma} \xrightarrow{\text{yields}} Z_{c,R} = \sqrt{\frac{L'_R}{C'_R}} \qquad Z_{c,L} = \sqrt{\frac{L'_L}{C'_L}} \qquad (2.25)$$

LH line was hypothetical till few years ago. Theoretically it could be achieved by cascading large enough number of cells (N) of lumped-element ladder networks (of series capacitance and shunt inductance), being the length of a single unit cell cascaded $d=\Delta z$ much shorter than wavelength ($d/\lambda_g \ll 1$). In practice it cannot be implemented in a completely distributed manner, and there is not a pure LH-TL, which exhibit those properties in an infinite bandwidth. However, as demonstrated in [29], incorporating to a “host transmission line” (microstrip line) series interdigital capacitors and parallel shorted-stub inductors, LH behaviour can be observed for a certain frequency range. This type of line is most commonly known afterwards as composite right/left-handed (CRLH). The name derives from the fact that different elements dominate depending on the frequency range, being the propagation RH (at high frequencies where parasitic from the host line dominate) or LH (at low frequencies where the reactive elements introduced dominate), see Fig. 2.5.c.

To analyse periodic structures, as it is the case of TL-based on MTMs, it is commonly used an eigenmode analysis (most usually referred to as Bloch wave analysis [16, 30]). This technique, based on the Floquet’s Theorem, consists in determining the eigen-solutions that can exist in the infinite periodic structure without excitation. The Bloch wave analysis directly provides the dispersion relation, which means a straightforward identification of pass bands and stop bands, and as a consequence the location (in the frequency spectrum) of the LH bands.

The structure is modelled by the equivalent characteristic Bloch impedance (Z_B) and the complex propagation constant (γ_B), see Fig. 2.7. These quantities

can be expressed as function of the transmission (ABCD) matrix by making an analogy with the propagation along a uniform equivalent transmission line.

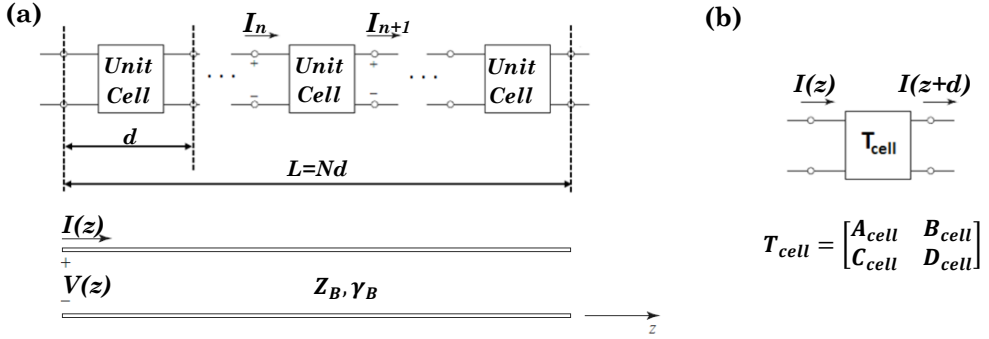


Fig. 2.7. - (a) Schematic for MTM TL, with N (reciprocal and symmetrical) unit cells with lattice constant d . (b) Every unit cell is characterized by the transfer matrix T_{cell} .

In the particular case of reciprocal and symmetric cells ($A=D$), the fundamental equations that characterize the periodic structure are:

$$T = \begin{bmatrix} A_{cell} & B_{cell} \\ C_{cell} & D_{cell} \end{bmatrix} \dots \begin{bmatrix} A_{cell} & B_{cell} \\ C_{cell} & D_{cell} \end{bmatrix} = T_{cell}^N = \begin{bmatrix} A & B \\ C & D \end{bmatrix} \quad (2.26)$$

$$\cosh(\gamma_B d) = A \quad \xrightarrow{\text{yields}} \quad \gamma_B = \pm \frac{1}{d} \cosh^{-1} A \quad (2.27)$$

$$Z_B = Z_c = \pm \sqrt{\frac{B}{C}} \quad (2.28)$$

where A, B, C, D are the four elements of the transmission matrix in (2.26).

In the circuit given in Fig. 2.5.c, the values of the distributed series capacitance and shunt inductance are:

$$Z'_{s_CRLH} = j \left(\omega L'_R - \frac{1}{\omega C'_L} \right) = j \frac{(\omega/\omega_s)^2 - 1}{\omega C'_L} \quad (2.29)$$

$$Y'_{p_CRLH} = j \left(\omega C'_R - \frac{1}{\omega L'_L} \right) = j \frac{(\omega/\omega_p)^2 - 1}{\omega L'_L} \quad (2.30)$$

with ω_s and ω_p being the series and shunt resonances respectively, defined as:

$$\omega_s = \frac{1}{\sqrt{L'_R C'_L}} \qquad \omega_p = \frac{1}{\sqrt{L'_L C'_R}} \qquad (2.31)$$

Using (2.11), or alternatively (2.27), it is obtained that:

$$\beta_{CRLH} = -\sqrt{\frac{1}{\omega^2 L'_L C'_L} (1 - (\omega/\omega_s)^2) (1 - (\omega/\omega_p)^2)} \quad \text{for } \omega < \omega_{01} \qquad (2.32)$$

$$\beta_{CRLH} = +\sqrt{\frac{1}{\omega^2 L'_L C'_L} (1 - (\omega/\omega_s)^2) (1 - (\omega/\omega_p)^2)} \quad \text{for } \omega > \omega_{02}$$

where

$$\omega_{01} = \min(\omega_s, \omega_p) \qquad \omega_{02} = \max(\omega_s, \omega_p) \qquad (2.33)$$

If ω_{01} is equal to ω_{02} it is said that the circuit is balanced ($L'_R C'_L = L'_L C'_R$). Otherwise the circuit is unbalanced, and there is a frequency gap between the RH and LH bands, see Fig. 2.8. The cutoff frequencies can be determined by identifying the frequencies where the Bloch impedance of the structure becomes imaginary. The characteristic impedance in a CRLH line is:

$$Z_{c_CRLH} = Z_{c_L} \sqrt{\frac{(\omega/\omega_s)^2 - 1}{(\omega/\omega_p)^2 - 1}} \qquad (2.34)$$

that becomes frequency independent [9] in the balance case, which is of special interest for a broadband matching:

$$Z_{c_CRLH}^{BAL} = Z_{c_R} = Z_L \qquad (2.35)$$

The dispersion equation can be also rewritten in the balanced case as:

$$\beta_{CRLH}^{BAL} = \beta_R + \beta_L = \omega \sqrt{L'_R C'_R} - \frac{1}{\omega \sqrt{L'_L C'_L}} \qquad (2.36)$$

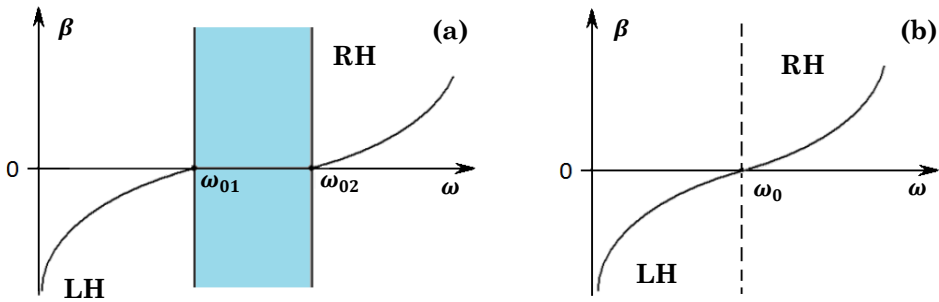


Fig. 2.8. - Dispersion diagrams for: (a) unbalanced CRLH-TL; (b) balanced CRLH-TL.

Many different transmission lines based on MTM concepts have been proposed since then. Similar strategies are based on loading with reactive elements (capacitors, inductors, and/or resonators) a host transmission line. In the literature, two main categories of MTM TLs regarding the type of loading elements [31] are distinguished:

- Planar non-resonant transmission lines, also called CL-loaded approach, since the loading elements are distributed inductors and capacitors. They are more easily synthesized than the resonant approach, and they usually exhibit a wider left handed band.
- Planar resonant transmission lines, sub-wavelength resonators are the loading elements. The presence of the resonators in the host line, originates a transmission zero located to the left of the LH passband. Such transmission zero can be useful in terms of filter selectivity, but can be also a drawback in other cases (limitation of operative bandwidth). This approach, of main interest for this work, is reviewed in more detail in next section 2.2.1.

It is worth noticing that this knowledge has also been applied to the area of acoustic metamaterials. Several types of acoustic transmission lines have been reported in [32-33], composed of an acoustic waveguide (for example a cylindrical pipe) periodically loaded with different structures such as Helmholtz resonators, side holes, membranes (as series capacitances) and/or transversal connected open channels (as shunt inductances), like in the example shown in Fig. 2.9.

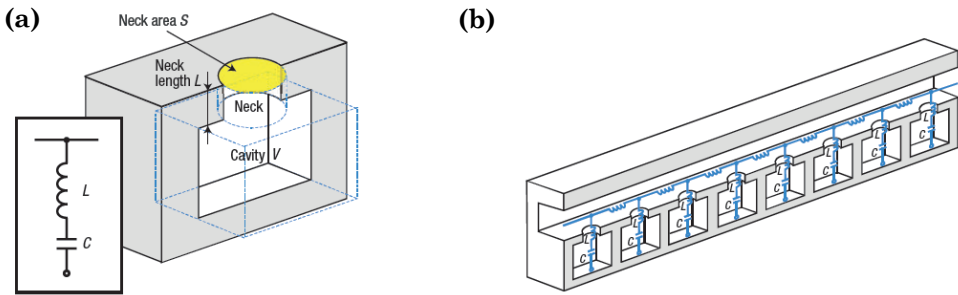


Fig. 2.9. - Cross-sectional view of a Helmholtz resonator (a). An acoustic TL ($K < 0$) that consists of an array of Helmholtz resonators (b). Picture extracted from [32].

Transmission lines based on EM MTM concepts present more design flexibility compared to conventional TLs, presenting the advantage that some electromagnetic properties may be controllable too. For instance, the characteristic impedance or the dispersion of the line can be tailored to some extent, in order to fulfil the specifications by designing the lumped elements. The losses in this technology are comparable to those of conventional transmission lines, and they are also compatible with microwave integrated circuits (MIC) and MMIC (monolithic MIC) in planar technology.

2.2.1 Resonant Approach

Resonators play an important role in the design of many microwave devices as filters, oscillators or amplifiers. In this approach, electrically small planar resonators are used to load a conventional transmission line; hence they are suitable for microwave device miniaturization (dimensions much smaller than the wavelength at their resonant frequency). The behaviour of these resonators can be explained in terms of an LC tank (see as an example in Fig. 2.13.b and Fig. 2.17.b). A review about the most popular used resonators is given next.

One of the most widely used resonators is the split ring resonator (SRR), proposed in 1999 [34], which allows to achieve a negative effective permeability ($\mu_{eff} < 0$) in a certain frequency range, above its resonant frequency. It became a very popular structure, since it was used in the demonstration of the first LH media [1].

There are several resonators inspired in the SRR layout, proposed with the aim of finding resonators of smaller size and/or minimizing some undesired effects such as cross polarization [35, 36]. Different strategies were applied, like

using: different number of splits on the ring to break the loop, different number of rings, different shapes (circular, square, rectangular) or multilayer-topologies. Between the multiples topologies proposed, we can mention:

- Double-slit SRR (DS SRR). The resonance frequency is twice the one of an SRR with identical dimensions -as defined in expression (2.47)-, but in this case cross-polarization is avoided. DS-SRR topology is depicted in Fig. 2.10.b. Note that the magnetic coupling effect is more dominant than the cross-polarization effect, so it can be neglected in a first approximation analysis [35].
- Spiral resonator (SR), depicted in Fig. 2.10.c. Its resonance frequency is reduced with respect to the one of an SRR with the same dimensions (equivalent circuit is similar to the SRR taking in account that $C_{SR} = 4C_S = C_0$, C_S and C_0 as defined later in section 2.2.1.1).
- Non-bianisotropic split ring resonator (NB-SSR), illustrated in Fig. 2.10.d, the equivalent circuit model and resonant frequency are identical to the SRR but with non-cross polarization effect.
- Multiple split ring resonators (MSRR). Increasing the number of rings yields to increase the capacitance, i.e. to decrease resonance frequency, or in other words, miniaturize the design. See Fig. 2.10.e, in this case the topology is square shape.

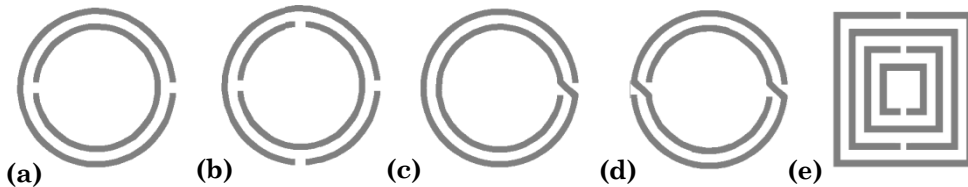


Fig. 2.10. - Sub-wavelength resonators: (a) SRR, (b) DS SRR, (c) SR, (d) NB-SRR, (e) MSRR. Metal parts are depicted in grey.

It is worth mentioning that a reduction in the particle size leads into a decrease of the bandwidth (stopband in negative permeability lines and passband in left-handed lines), so that effect should be taken into account when choosing the loading elements [37].

Most of the particles based on SRRs [35,38], as the ones previously mentioned, have a dual version, usually referred to as complementary since it is the result of removing the original particle from a metallic screen. Hence, a “C”

is added to name the derived particle in the acronym form (i.e. CSRR, CSR, DS-CSRR...). For instance, CSRR is the complementary particle of the split ring resonator; shown graphically in Fig. 2.11.b. Under real conditions some deviations from duality are observed (mainly due to the presence of the substrate that affects particularly to the capacitance value), and for example the resonance frequencies of an SRR and a CSRR of same dimensions are similar, but not equal.

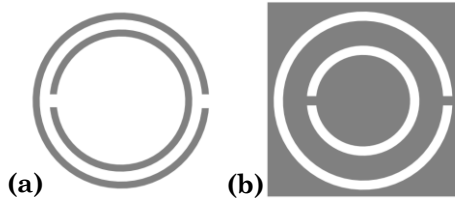


Fig. 2.11. - Topology of an SRR (a) and its dual particle CSRR (b). Metal parts are depicted in grey.

Other particles of practical interest also based on SRRs are the open resonators: the open SRR (OSRR) [39], and the open CSRR (OCSRR) [39]. In contrast to previous closed particles, these are opened by elongating the rings (re-shaped as hooks), see Fig. 2.12. “Open resonator” means that the particle exhibits two metallic terminals for excitation (through a voltage or current source), in contrast to previous particles (particle were magnetically/electrically excited). In a first order approximation, the OSRR can be modeled as an open series resonator and the OCSRR as an open parallel resonant tank. However, some phase shift occurs at resonance, due to the presence of the host line, and the accurate models should include these parasitic effects. Further details about TLs with OSRRs and OCSRRs can be found in section 2.2.1.3.

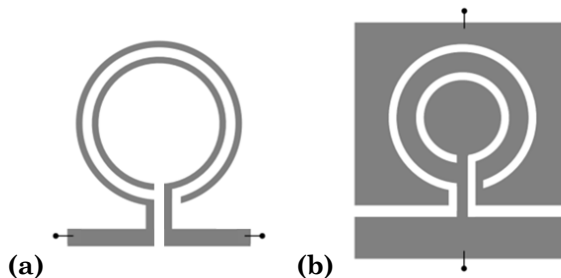


Fig. 2.12. - Sub-wavelength resonators: (a) OSRR, (b) OCSRR.

The equivalent circuits which properly model the behavior of the line are a very powerful tool used for the design and characterization of the line [41]-[42].

In general the unit cell is modelled by means of a T-circuit model or a π -circuit model, see Fig. 2.13. If cell is symmetric, which is the most usual case in MTM TLs, $Z_{s1} = Z_{s2}$ or equivalently $Z_{p1} = Z_{p2}$. Parameter extraction (PE) processes are used in order to determine the value of the lumped elements from simulations or measurements, as it is graphically illustrated in next figure. Sometimes circuital values are determined by optimization (the ones which make fit better the circuital simulation with the EM simulation). In other cases, by imposing several conditions (as many as the number of unknowns) to the extracted data from EM response (or measurements), they can be determined in a straightforward way. The PE procedure used to determine the lumped elements in the lines is automated as explained in Chapter 3.

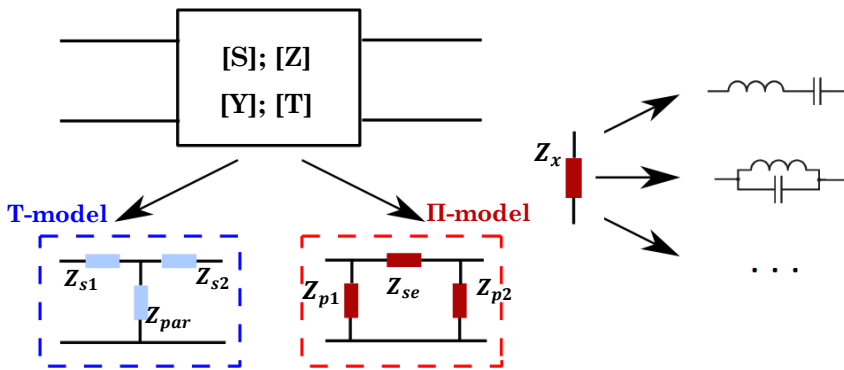


Fig. 2.13. - Parameter extraction process.

If we have a typical T-model, the Z parameters are related with the series and shunt impedance with the following expressions given in [43]:

$$Z_{se} = Z_{11} - Z_{12} \tag{2.37}$$

$$Z_{par} = Z_{12} \tag{2.38}$$

where Z_{se} and Z_{par} are the series and shunt impedances in the equivalent circuit. In the π -model the Y-parameters are frequently used:

$$Z_{se} = -Y_{12}^{-1} \tag{2.39}$$

$$Z_{par} = (Y_{12} + Y_{12})^{-1} \tag{2.40}$$

The characteristic impedance and dispersion characteristics are related with the transmission parameters through (2.27) and (2.28). But they can be also determined from Z_{se} and Z_{par} as follows:

$$Z_c = \sqrt{Z_{se}(Z_{se} + 2Z_{par})} \quad \dots \quad \text{in the } T - \text{model} \tag{2.41}$$

$$Z_c = \sqrt{\frac{Z_{se}^2 Z_{par}}{2Z_{par} + Z_{se}}} \quad \dots \quad \text{in the } \pi - \text{model}$$

$$\cosh(\beta d) = 1 + \frac{Z_{se}}{Z_{par}} \tag{2.42}$$

with d being the unit cell length.

Even we will focus more on filter structures there are many other useful applications that can be achieved by TLs based on MTMs concepts, such as power dividers or couplers. For those cases the electrical length of the line is forced ($\beta d = \pm 90^\circ$), as well as the impedance to a certain desirable value Z_a at two different frequencies f_1 and f_2 . So applying those constraints to (2.41) and (2.42) it follows:

$$Z_{se}|_{f_1} = j Z_a \tag{2.43}$$

$$Z_{se}|_{f_2} = -j Z_a \tag{2.44}$$

$$Z_{par}|_{f_1} = -j Z_a \tag{2.45}$$

$$Z_{par}|_{f_2} = j Z_a \tag{2.46}$$

So if the series and shunt impedances of the CRLH line are known, the element values of the circuit model can be inferred. A practical application example is shown later in chapter 4.

Several kinds of resonant transmission lines have been proposed, coupling different kind of resonators (mainly SRRs or CSRRs) in different ways to different transmission lines (microstrip, coplanar or stripline), and in combination with different additional elements (varactors, shunt strips, series

gaps...). In the following subsections, the transmission lines based on SRRs, CSRRs, OSRRs and OCSRRs are presented in further detail.

2.2.1.1 TLs based on SRRs

The first resonant MTM transmission line was based on SRRs [44]. The original SRR is composed of two concentric open metallic rings, as shown in Fig. 2.14.a. At the resonant frequency ω_0 , defined as:

$$\omega_0 = \frac{1}{\sqrt{L_S C_S}} = \sqrt{\frac{2}{\pi r_0 L_S C_{pul}}} \tag{2.47}$$

the perimeter of the resonator is smaller than half the wavelength of the exciting wave. The resonator self-inductance L_S can be approximated to the inductance of a single ring with the mean radius of the SRR ($r_0 = r_{ext} - c - d/2$), and the width of the rings (c).

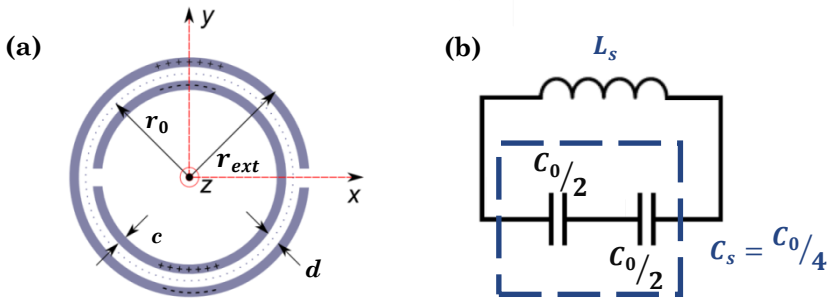


Fig. 2.14. - (a) Topology of a SRR with the relevant dimension: external radius (r_{ext}), mean radius (r_0), ring's width (c), distance between the metallic rings (d). (b) Equivalent circuit of a SRR.

On the other hand C_0 is the total capacitance between the rings:

$$C_0 = 2\pi r_0 C_{pul} \tag{2.48}$$

with C_{pul} being the capacitance per unit length originated between the rings. The capacitance of the SRR (C_S) is a quarter of C_0 , as depicted in Fig. 2.14.b. The closer the rings are, the lower the resonance frequency is and therefore the particle is electrically smaller. Analytical equations when a dielectric is present are published in [35]. It was also available a program from the web page of the

author, based on those equations [35, 45], that allowed to compute on-line the frequency of resonance and LC equivalent parameters of SRRs and CSRRs [46]. In fact this program, with some slight modifications, was used to calculate the initial dimensions of the resonators in our automated synthesis process, see Chapter 3 for more details.

In a rough approximation, SRR can be considered as a resonant magnetic dipole that can be properly excited by means of an axial magnetic field. This fact has to be taken under consideration when coupling SRRs to the host line. When coupled to a coplanar waveguide, SRRs are generally etched (in pairs) to the bottom side of the substrate, just underneath the slots of the structure, see Fig. 2.15.a. The resonators provide negative permeability, and if no extra loading elements are included, the structure shows a stopband behavior [41, 44]. The equivalent circuit associated is also depicted in Fig. 2.15.b. The parameters L and C represent the per-section inductance and capacitance of the CPW, respectively, whereas the SRRs are modelled as a parallel resonant tank (with inductance L_s and capacitance C_s) magnetically coupled to the line through a mutual inductance M .

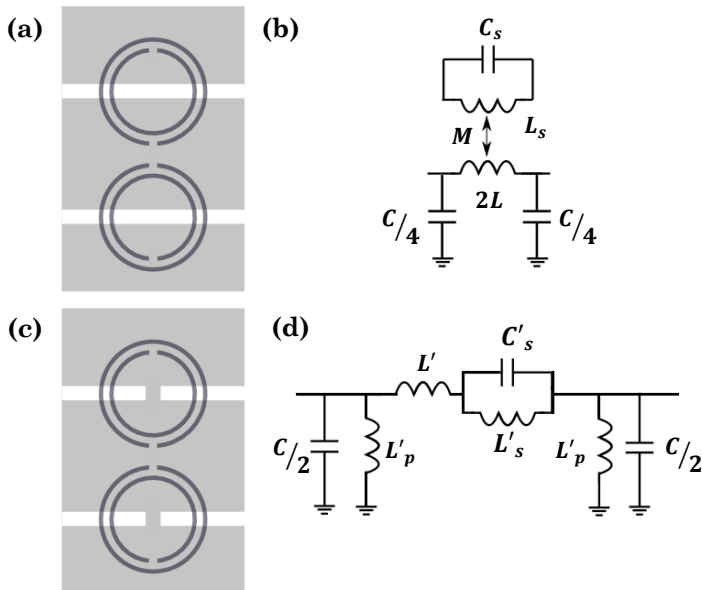


Fig. 2.15. - Topology of a basic unit cell of a CPW loaded with SRRs (a), with its equivalent circuit (b). Topology of a basic unit cell of a CPW with SRRs and shunt strips (c), and its equivalent circuit (d). SRRs in dark grey are on the bottom.

By introducing to the previous design shunt strips (thin metal wires that connect the signal line to the ground plane) centered with regard to the SRRs, see Fig. 2.15.c, left-handed behavior is observed above the resonant frequency [41, 44]. The frequency response is now band-pass, being the strips inclusion which provides a negative effective permittivity to the structure. The equivalent circuit of this topology, after applying a transformation to have a pi-model circuit (more convenient in order to analyze the TL behavior as explained in previous section), is shown in Fig. 2.15.d. This circuit model is an improvement of a previous equivalent circuit model proposed in [47].

Other topologies in CPW technology add to the former design in Fig. 2.15.a a series gap, shunt strips and series-gap or varactors [48]. The approach that introduce varactors and shunt strips, illustrated in Fig. 2.16.a, is very interesting since it enhances out-band rejection properties, and a reconfigurable filter is obtained, as it can be appreciated in Fig. 2.16.b. Another configuration in CPW, less frequently used, is achieved by etching the SRRs inside the slots [49].

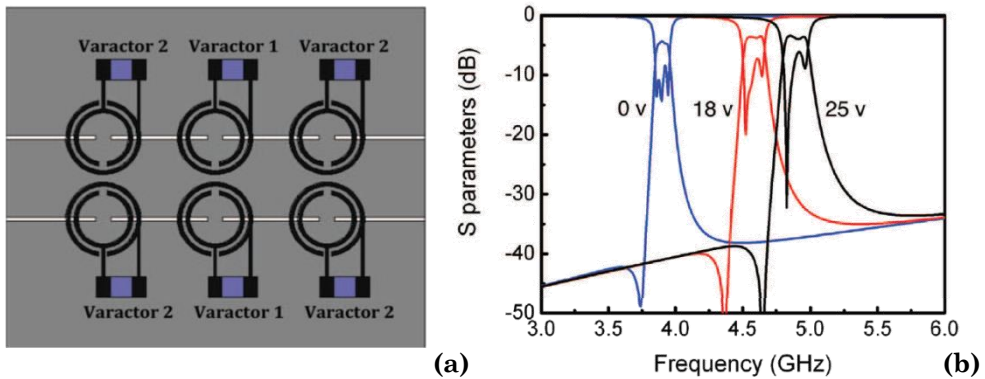


Fig. 2.16. - (a) Topology of a CPW loaded with SRRs, shunt strips and varactors; (b) simulated response of the 3-stage tunable filter [48].

In the case that the host line is microstrip, SRRs are etched on the upper substrate side (usually in pairs), adjacent to the conductor strip. Metallic vias, once introduced, are the responsible of the negative permittivity. In Fig. 2.17, different designs in microstrip technology are presented. In the first example, the line is periodically loaded with square shaped SRRs, placed very closely to the conductor strip, and metallic vias are used [50]. A square topology was chosen to enhance the magnetic coupling between line and SRRs. As result a narrow band pass filter with small size dimensions is obtained. In the second

example, SRRs are introduced in a microstrip coupled line band pass filter, in order to suppress spurious resonances out of band. Another possible application of a microstrip line loaded with SRR, shown in Fig. 2.17.c, is to provide conjugate matching between the antenna and the integrated circuit in typical RFID-tags [51].

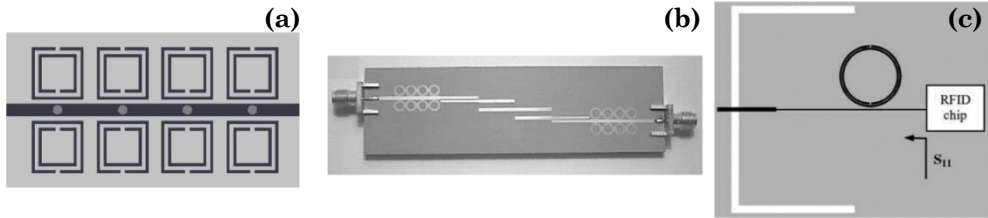


Fig. 2.17. - (a) Topology of microstrip line loaded with SRRs, and metallic vias [50]. (b) Prototype that demonstrates application to spurious suppression [28]. (c) Schematic of dual-band matching network, including slot antenna [51].

2.2.1.2 TLs based on CSRRs

The CSRR is the result of applying the Babinet principle to the SRR structure [38]. It is a particle composed of two concentric open non-metallic rings of width c , as illustrates Fig. 2.18.a. Its equivalent circuit, described in [35], is also a resonant tank LC, see Fig. 2.18.b.

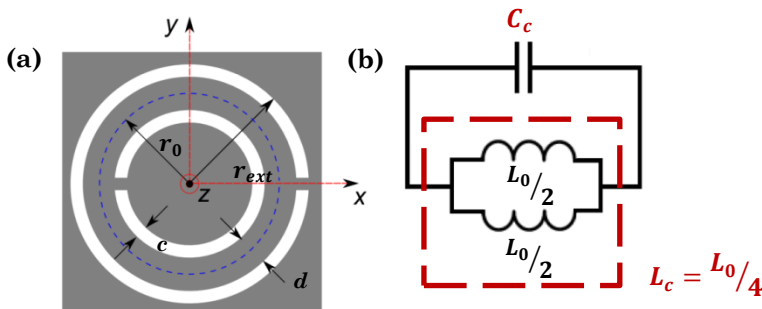


Fig. 2.18. - (a) Topology of a CSRR with its relevant dimensions. Metal regions are depicted in grey. (b) Equivalent circuit of a CSRR.

The capacitance of a CSRR is approximated to that corresponding to a metallic disk of radius $r_0 - c/2$ surrounded by a ground-plane at a distance c , being r_0 the averaged radius of CSRR, as stated in [35]. The inductance is given by the parallel connection of two inductances, of value $L_0/2$, originated by the metallic strips between the inner and outer metallic regions of the CSRR:

$$L_0 = 2\pi r_0 L_{pul} \tag{2.49}$$

with L_{pul} the per unit length inductance of a circular coplanar waveguide (of length $2\pi r_0$, strip width d , and slot width c) connecting the inner disk to the ground.

The properties of this particle are the dual ones of the SRR ones. Therefore, it can be said that CSRR behaves approximately as an electric dipole excited by an axial electric field, and exhibits a negative value of permittivity. CSRRs must be etched either in the conductor strip or in the ground plane, i.e. where the electric field is maximum. The most common case is to load a microstrip line with CSRRs on the ground plane (etched), as illustrates Fig. 2.19.a. The structure shows as result a stopband behavior. The equivalent T-circuit model proposed in [35] and depicted in Fig. 2.19.b, models the CSRR with the LC tank, the coupling with the host line is modeled with the capacitance C , and L represents the line inductance.

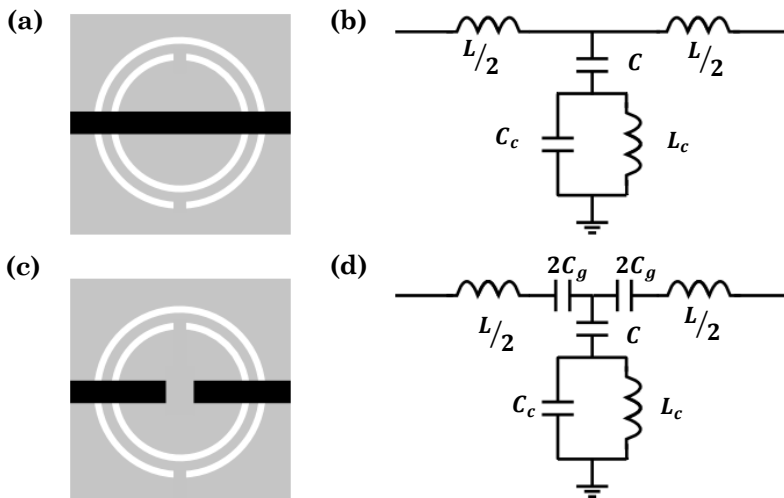


Fig. 2.19. – Basic unit cell of a microstrip loaded with CSRR (a), and equivalent circuit (b). Basic unit cell of microstrip loaded with CSRR and gaps(c), and equivalent circuit (d). The upper metallization is depicted in black and ground plane in grey.

The aforementioned stopband filter can be switched to a band pass/high pass performance by periodically etching capacitive gaps on the signal strip just above the resonators, see Fig. 2.19.c. These gaps provide the negative effective permeability up to a frequency that can be tailored by properly designing the

gap dimensions. The series gap is modelled in the equivalent circuit by the capacitance C_g , see Fig. 2.19.d In order to obtain balanced CRLH TL, bigger values of gap capacitance ($C_g \gg C$) are usually needed, and hence different shapes of gaps have been introduced, between them T-gaps or meandered [52]. By introducing additional elements (such as grounded stubs, that introduce a transmission zero), some limiting aspects as poor selectivity in upper band are minimized, so compact filters with good out-band performance can be achieved [53]-[54], an example of a unit cell is shown in Fig. 2.20.a. The grounded stubs are modeled by means of a shunt inductance L_p in the equivalent circuit model, see Fig. 2.20.b. Other examples where the host transmission line is a microstrip, can be found in [55].

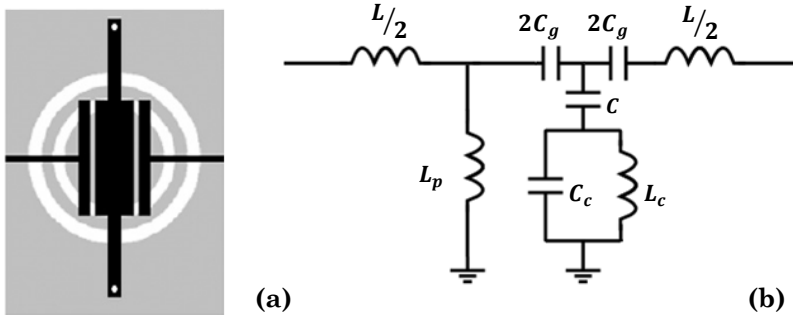


Fig. 2.20. - Basic unit cell, the two shunts are connected to ground by vias (a); equivalent circuit (b). The upper metallization is depicted in black and ground plane in grey.

It is worth mentioning that when CSRRs are etched very close, the capacitive coupling between adjacent cells should be taken into account for better accuracy, as stated in [56]. The semi lumped-element circuit models proposed including the capacitive coupling between adjacent resonators (ports R2 and L2) are shown in Fig. 2.21. They CSRR line is now described by a 4-port network, where C_R describes the coupling between adjacent resonators, and rest of parameters have same meaning of those in Fig. 2.19.

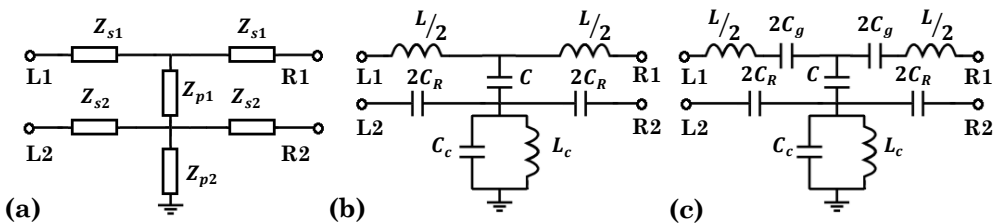


Fig. 2.21. - (a) Generalized impedance model; (b) Modified circuit model for topology depicted in Fig. 2.19.a, (c) Modified circuit model for topology depicted in Fig. 2.19.c. Models from [56].

In coplanar technology, fewer examples have been found. One of them shows how the bandwidth of the resulting TL can be increased by adding slots in the vicinity of the CSRRs [57] as it can be seen in the topology illustrated in Fig. 2.22.b (one is in the ground conductor and the other is placed in the center conductor). Other interesting example is a CPW structure with CSRRs etched in the central strip, that by adding RF-MEMs bridges on top of them, the stop-band structure is provided with tuning capability at Q-band [58].

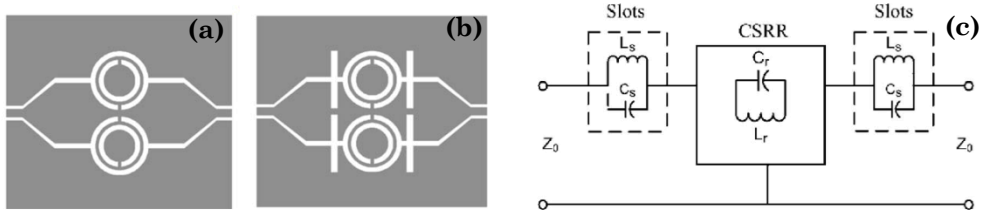


Fig. 2.22. - Basic unit cell of a CPW loaded with CSRRs positioned on the ground plane (a), idem with added slots in the center conductor (b), and equivalent circuit of the structure in (c). At the edges of the structure the tapers used to perform the measurements are depicted. Figures extracted from [59].

2.2.1.3 TLs based on OSRRs and OCSRrs

The OCSRr is obtained from the SRR topology by opening it and applying duality (as in CSRR), see Fig. 2.23.a. In a first approximation it can be modeled as a parallel LC resonator (Fig. 2.23.b), where C_p is equal to the capacitance of the CSRR, whereas the inductance L_p is four times the one of the CSRR, i.e. $L_p = L_0$ as it was defined in equation (2.49). Some additional elements, to model the frequency shift due to the access lines should be introduced [60], as it can be seen in Fig. 2.26.c.

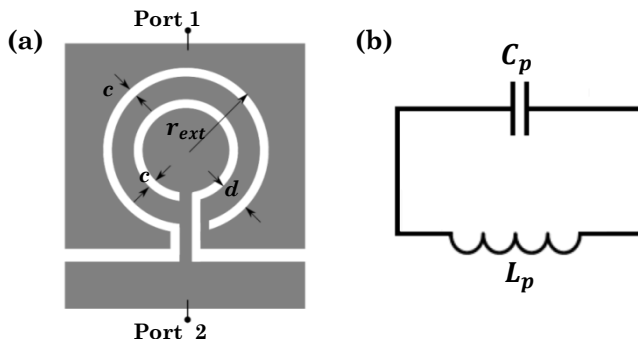


Fig. 2.23. - (a) Typical topology of an OCSRr (the two terminals/ports are indicated). (b) Equivalent circuit of an OCSRr.

The typical topology of an OSRR cell is depicted in Fig. 2.24.a. One of the rings is excited by the signal flowing through the transmission line conductor, while the other ring is excited by the displacement current flowing through the slot between both rings. The resonator was initially thought to be series connected to a microstrip line [39]. In a first order approximation it can be modelled as a series LC resonator (see Fig. 2.24.b), where L_s is identically to the inductance of an SRR with same dimensions, and $C_s = C_0$ is the distributed capacitance between the inner and outer rings, i.e. four times the one which presents an SRR, given by expression (2.48). From this, it follows that the resonant frequency is half of the resonant frequency of an SRR given by (2.47). To take into account the phase shift given by the access lines, it is used the equivalent circuit depicted in Fig. 2.24.c.

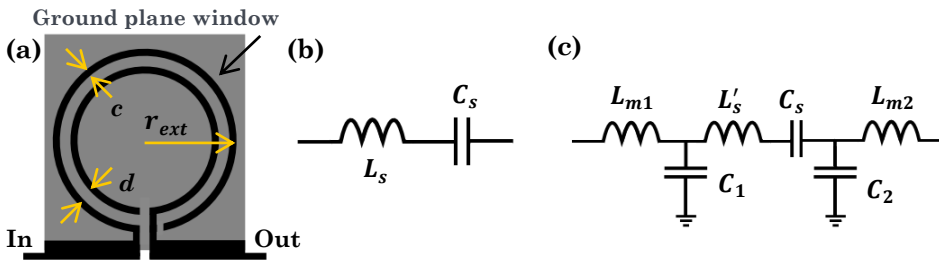


Fig. 2.24. - (a) Typical topology of an OSRR excited by a microstrip line. Ground plane window is practiced in order not to disturb the EM behavior of the OSRR. (b) Equivalent circuit of an OCSRR: 1st approach. (c) More accurate circuit model (taking into account access lines) with $L'_s = L_s + 2L$.

In the case of OSRR implemented in CPW technology, the equivalent circuit model can be simplified to the one illustrated in Fig. 2.25.b, since the resonator has much smaller phase shift [61]. The inductances L_{m1} and L_{m2} are neglected and the shunt capacitances are considered to be equal ($C_1 = C_2$).

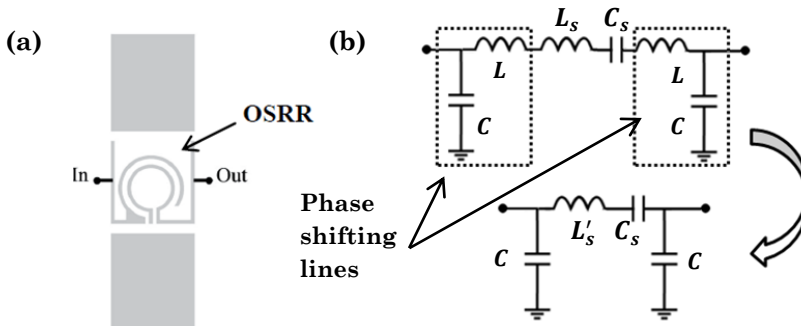


Fig. 2.25. - (a) Typical topology of an OSRR in CPW technology. Equivalent circuit of an OCSRR (b), simplified circuit model with $L'_s = L_s + 2L$.

When OCSRRs are coupled to a coplanar TL, usually they are symmetrically placed on the slots as illustrates Fig. 2.26.a. To avoid the presence of the slot mode of the CPW and the second resonance of the OCSRRs, it is necessary to connect the different ground plane regions of the CPW (by means of backside strips and vias). The equivalent circuit shown in Fig. 2.26.b, models the access line through series inductances (L) and shunt capacitances (C), being also shown for designing convenience the equivalent T-circuit model with $C'_p = 2C_p + 2C$ and $L'_p = L_p/2$. Since some discrepancies can appear at high frequencies between EM and circuitual simulations, sometimes the equivalent circuit of Fig. 2.26.c is used instead, in particular for wideband applications. A parasitic L_{sh} is introduced to take into account the effect of the connection between the central strip of the CPW TL and the inner metallic region of the OCSRR.

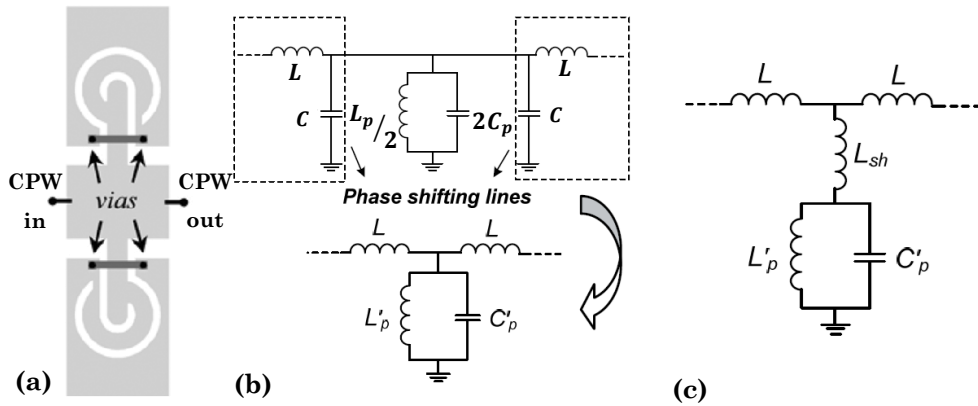


Fig. 2.26. - (a) Topology of OCSRRs loaded in CPW, (b) Equivalent circuit 1, (c) Equivalent circuit $L'_p = L_p/2$, $C'_p = 2 \cdot (C + C_p)$.

A direct application of this technology is a bandpass filter, since it can be easily achieved by cascading shunt connected parallel resonators coupled through admittance inverters [62], see Fig. 2.27.a.

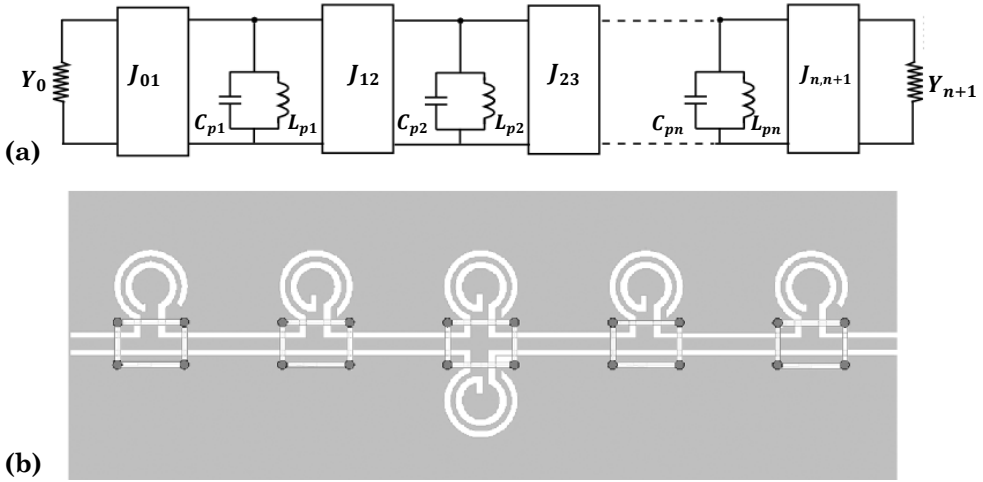


Fig. 2. 27. - (a) Typical network of a bandpass filter with admittance inverters and shunt LC resonators. (b) Layout of first bandpass filter implemented with OCSR [40].

In the same paper where the OCSR particle was introduced [40], an application example based on that approach was presented. A wide bandpass filter is obtained by cascading stages of one (or two) shunt connected resonator sandwiched between a pair of $\lambda/8$ and 50Ω lines; see Fig. 2.27.b.

A bandpass filter can be also obtained by coupling shunt OCSR in microstrip and admittance inverters (implemented with line sections), as demonstrated in [63], see Fig. 2.28. The measured bandwidth is smaller than the bandwidth of the ideal response, since the inverters strictly exhibit their functionality at the central filter frequency.

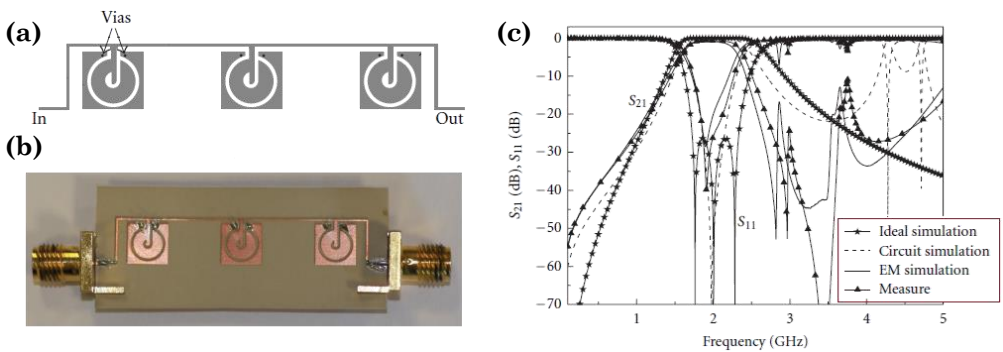


Fig. 2.28. - (a) Layout of a wide-band bandpass filter (b) Photograph of the prototype, (c) Frequency response (measured, EM simulation and circuit simulations) [63].

However, more compact broadband bandpass filters can be achieved alternating sections of host lines loaded with series connected OSRRs and shunt connected OCSRRs (no need of introducing line inverters), see Fig. 2.29 and Fig. 2.30.

The methodology followed to design a bandpass filter consists first in determining the values of the filter prototype in the canonical form (i.e. Chebyshev, Butterworth). The resulting filter can be obtained by alternately cascaded sections of LC series resonator (i.e. OSRRs) and LC parallel resonator (i.e. OCSRR), being the parasitic L , C illustrated in Fig. 2.29.c not considered in a first approach. The next step is to infer the values of the parasitic elements, by means of parameter extraction methods. Afterwards the resonators are tailored until specifications are satisfied at circuitual level (enhanced model of Fig. 2.29.c). Finally, layout is modified until circuit and EM simulation are similar. An example in coplanar technology of an order 3 Chebyshev bandpass filter (0.02 dB ripple) with central frequency 2.9 GHz is illustrated in Fig. 2.29, and reported in [64].

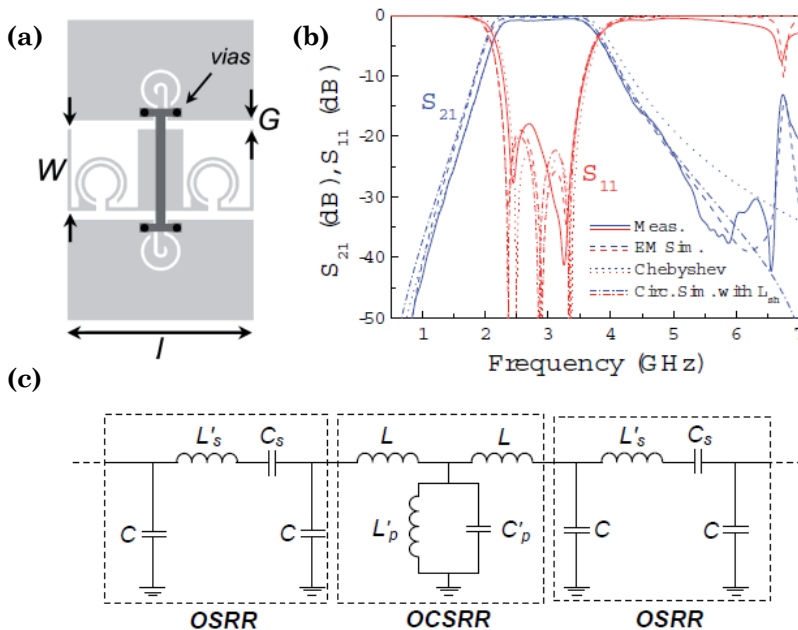


Fig. 2.29. - (a) Layout of a wide-band bandpass filter (order-3 Chebyshev), (b) Frequency response (measured, EM and circuit simulations) (c) Circuit model, including access line effect ($L'_s = L_s + 2L$, $L'_p = L_p / 2$, $C'_p = 2 \cdot (C + C'_p)$). Lsh can be included in the schematic for better accuracy.

The same procedure can be applied in microstrip technology, but the design is more complicated since the circuit model of a microstrip line section loaded with an OSRR is more complex, see Fig. 2.24.c, as well as the associated PE method [60]. An example of a 3-order Chebyshev bandpass filter (0.1 dB ripple) with central frequency 1.3 GHz is illustrated in Fig. 2.30 (originally published in [64]).

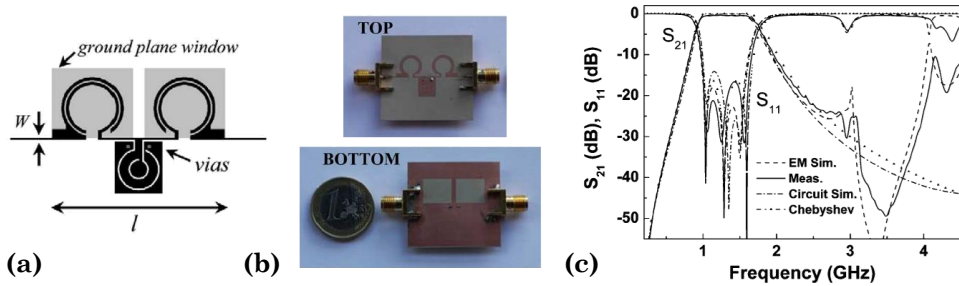


Fig. 2.30. - (a) Layout of a wide-band bandpass filter , (b) Photograph of the prototype, (c) Frequency response (measured, EM simulation and circuit simulations) [64].

The typical transmission zero present in the SRR- or CSRR-loaded lines is absent in OSRR and OCSRR based lines, so in general wider bandwidths can be achieved. Other examples related to the design of multiband microwave components based on OSRRs and OCSRRs can be found in [65]-[66].

References

- [1] D.R. Smith, W.J. Padilla, D.C. Vier, S.C. Nemat-Nasser, and S. Schultz, “Composite medium with simultaneous negative permeability and permittivity,” *Physical Review Letters*, vol. 84, pp. 4184-4187, May 2000.
- [2] J. B. Pendry, “Negative Refraction Makes a Perfect Lens,” *Physical Review Letters*, vol. 85, issue 8, pp. 3966-3969, Oct. 2000.
- [3] R. A. Shelby, D. R. Smith, and S. Schultz, “Experimental verification of a negative refractive index of refraction,” *Science*, vol. 292, pp.77-79, April 2001.
- [4] N. Engheta, “An idea for thin subwavelength cavity resonators using metamaterials with negative permittivity and permeability,” *IEEE Antennas and Wireless Propagation Letters*, vol. 1, issue 1, pp. 10-13, Jan. 2002.
- [5] J. C. Bose, “On the rotation of plane of polarization of electric waves by a twisted structure” *Proceedings of the Royal Society of London*, vol. 63, pp. 146-152, Jan. 1898.
- [6] V. G. Veselago, “The electrodynamics of substances with simultaneously negative values of ϵ and μ ,” *Soviet Physics Uspekhi*, vol. 10, no. 4, pp. 509-514, April 1968.
- [7] R. M. Walser, “Electromagnetic metamaterials,” *Proceedings SPIE*, 4467, *Complex Mediums II: Beyond Linear Isotropic Dielectrics*, July 2001.
- [8] C. Caloz and T. Itoh, *Electromagnetic Metamaterials: Transmission Line Theory and Microwave Applications. The Engineering Approach*, Wiley-IEEE Press, Dec. 2005
- [9] N. Engheta and R. W. Ziolkowski (Editors), *Metamaterials. Physics and Engineering Exploration*, Wiley-IEEE Press, June 2006.
- [10] W. Cai and V. Shavalev, *Optical Metamaterials*, Springer 2010.
- [11] T. J. Cui, R. Liu and D. R. Smith *Metamaterials: Theory, Design, and Applications*. Springer, New York, 2010.
- [12] A. Boardman, “Pioneers in metamaterials: John Pendry and Victor Veselago,” *Journal of Optics*, vol. 13, no. 2, Dec. 2010.
- [13] S. A. Cummer and David Schurig, “One path to acoustic cloaking,” *New Journal of Physics*, vol.9, pp 1-8, March 2007.
- [14] Z. Liu, X. Zhang, Y. Mao, Y. Y. Zhu, Z. Yang, C. T. Chan, and P. Sheng, “Locally resonant sonic materials,” *Science*, vol. 289, no. 5485, pp. 1734-1736, Sept. 2000.

- [15] Y. Ding, Z. Liu, C. Qiu, and J. Shi, "Metamaterial with simultaneously negative bulk modulus and mass density," *Physical Review Letters*, vol. 99, pp. 1-4, Aug. 2007.
- [16] F. Bongard, "Contribution to Characterization Techniques for Practical Metamaterials and Microwave Applications", PhD. Ecole Polytechnique Fédérale de Lausanne, 2009.
- [17] D. Schurig, J. J. Mock, B. J. Justice, S. A. Cummer, J. B. Pendry, A. F. Starr and D. R. Smith, "Metamaterial Electromagnetic Cloak at Microwave Frequencies," *Science* 10, pp. 977-980, Oct. 2006.
- [18] M. Farhat, S. Enoch, S. Guenneau, and A. B. Movchan, "Broadband cylindrical acoustic cloak for linear surface waves in a fluid," *Physical Review Letters*, vol. 101, pp. 134501(1)-134501(4), Sept. 2008.
- [19] P. Alitalo, and S. Tretyakov, "Electromagnetic cloaking with metamaterials," *Materials today*, vol. 12, no. 3, March 2009.
- [20] L. Zigoneanu, B. I. Popa and S. A. Cummer, "Three-dimensional broadband omnidirectional acoustic ground cloak," *Nature Materials*, vol. 3, pp.352-355, April 2014.
- [21] X. Zhang, and Z. Liu, "Superlenses to overcome the diffraction limit," *Nature Materials*, vol. 7, pp. 435-441, June 2008.
- [22] N. Fang, H. Lee, C. Sun, X. Zhang, "Sub-diffraction-limited optical imaging with a silver superlens," *Science*, vol. 308, no. 5721, pp. 534-537, April 2005.
- [23] J. Li, L. Fok, X. Yin, G. Bartal, and X. Zhang, "Experimental demonstration of an acoustic magnifying hyperlens," *Nature Materials*, vol. 8, 931-934, Oct. 2009.
- [24] J. Zhu, J. Christensen, J. Jung, L. Martin-Moreno, X. Yin, L. Fok, X. Zhang and F. J. Garcia-Vidal, "A holey-structured metamaterial for acoustic deep-subwavelength imaging," *Nature Physics*, vol.7, pp. 52-55, Nov. 2010.
- [25] K. Z. Rajab, R. Mittra, M. T. Lanagan, "Size reduction of microstrip antennas using metamaterials," *IEEE Antennas and Propagation Society International Symposium*, pp. 296-299, July 2005.
- [26] J. Bonache, I. Gil, J. García-García, and F. Martín, "Complementary split rings resonators (CSRRs): Towards the miniaturization of microwave device design," *Journal of Computational Electronics*, vol. 5, pp. 193-197, July 2006.
- [27] J. A. Marcotegui, J. M. Illescas, A. Estevez, and F. Falcone, "Compact ultra wide band microstrip bandpass filter based on multiple-mode resonator and

modified complementary split ring resonator”, *The Scientific World Journal*, Nov. 2013.

[28] J. Garcia-Garcia, F. Martin, F. Falcone, J. Bonache, I. Gil, T. Lopetegi, M.A.G. Laso, M. Sorolla and R. Marques, “Spurious passband suppression in microstrip coupled line band pass filters by means of split ring resonators,” *IEEE Microwave and Wireless Components Letters*, vol. 14, no. 9, pp. 416-418, Sept. 2004.

[29] C. Caloz, and T. Itoh, “Application of the transmission line theory of left-handed (LH) materials to the realization of a microstrip LH transmission line,” *IEEE Antennas and Propagation Society International Symposium*, pp. 412-415, June 2002.

[30] J. Perruisseau-Carrier and A. K. Skrivervik, “Bloch wave approach to the design of optimally matched non-effective medium composite right/left handed transmission lines,” *IET Microwave Antennas and Propagation*, vol. 1, no. 1, pp. 50–55, Feb. 2007.

[31] F. Aznar, M. Gil, J. Bonache, and F. Martin “Characterization of miniaturized metamaterial resonators coupled to planar transmission lines through parameter extraction,” *Opto-Electronics Review*, vol. 16, no. 3, pp. 226-236, Sept. 2008.

[32] N. Fang, D. J. Xi, J. Y. Xu, M. Ambati, W. Srituravanich, C. Sun, and X. Zhang, “Ultrasonic metamaterials with negative modulus,” *Nature Materials*, vol. 5, pp. 452-456, April 2006.

[33] S. H. Lee, C. M. Park, Y. M. Seo, Z. G. Wang, and C. K. Kim, “Composite acoustic medium with simultaneously negative density and modulus,” *Physical Review Letters*, vol. 104, pp. 1-4, Feb. 2010.

[34] J. B. Pendry, A. J. Holden, D. J. Robbins, W. J. Stewart, “Magnetism from conductors and enhanced non-linear phenomena,” *IEEE Transactions on Microwave Theory and Techniques*, vol. 47, pp. 2075-2084, Nov. 1999.

[35] J. D. Baena, J. Bonache, F. Martin, R. M. Sillero, F. Falcone, T. Lopetegi, M. A. G. Laso, J. Garcia-Garcia, I. Gil, M. F. Portillo, and M. Sorolla, “Equivalent-circuit models for split-ring resonators and complementary split-ring resonators coupled to planar transmission lines,” *IEEE Transactions on Microwave Theory and Techniques*, vol. 53, no.4, pp. 1451-1461, April 2005.

[36] R. A. Nutan, and S. Raghavan, “Split ring resonator and its evolved structures over the past decade: This paper discusses the nuances of the most celebrated composite particle (split-ring resonator) with which novel artificial structured materials (called metamaterials) are built,” *International Conference*

on Emerging Trends in Computing, Communication and Nanotechnology (ICE-CCN), pp.625-629, March 2013.

[37] F. Aznar, M. Gil, J. Bonache, and F. Martin, “On the effects of resonator's electrical size on bandwidth in resonant-type metamaterial transmission lines,” *Microwave and Optical Technology Letters*, vol. 52, issue 7, pp. 1526-1530, July 2010.

[38] F. Falcone, T. Lopetegi, M. A. G. Laso, J.D. Baena, J. Bonache, M. Beruete, R. Marqués, F. Martín, M. Sorolla, “Babinet principle applied to the design of metasurfaces and metamaterials”, *Physical Review Letters*, vol. 93, no. 19, pp. 197401(1)-114501(4), November 2004.

[39] J. Martel, R. Marqués, F. Falcone, J.D. Baena, F. Medina, F. Martín, M. Sorolla, “A new LC series element for compact band pass filter design,” *IEEE Microwave and Wireless Component Letters*, vol. 14, no.5, pp. 210–212, May 2004.

[40] A. Velez, F. Aznar, J. Bonache, M.C. Velázquez-Ahumada, J.Martel, F. Martín, “Open complementary split ring resonators (OCSRRs) and their application to wideband CPW band pass filters,” *IEEE Microwave Wireless and Component Letters*, vol. 19, issue 4, pp. 197–199, April 2009.

[41] F. Aznar, J. Bonache, and F. Martin, “Improved circuit model for left-handed lines loaded with split ring resonators”, *Applied Physics Letters*, vol. 92, pp. 043512(1)- 043512(3), Feb. 2008.

[42] J. Bonache, M. Gil, I. Gil, J. Garcia-Garcia and F. Martin, “On the electrical characteristics of complementary metamaterial resonators,” *IEEE Microwave and Wireless Components Letters*, vol. 16, no.10, pp.543-545, Oct. 2006.

[43] D. M. Pozar, *Microwave Engineering*, John Wiley & Sons, 3rd ed., 2005.

[44] F. Martín, F. Falcone, J. Bonache, R. Marques and M. Sorolla, “A new split ring resonator based left handed coplanar waveguide”, *Applied Physics Letters*, vol. 83, no. 22, pp. 4652-4654, Dec. 2003.

[45] R. Marqués, F. Mesa, J. Martel, and F. Medina, “Comparative analysis of edge- and broadside-coupled split ring resonators for metamaterial design: Theory and experiment,” *IEEE Transactions on Antennas and Propagation*, vol. 51, no. 10, pp. 2572–2581, Oct. 2003.

[46] SRR and CSRR calculator available from: <http://personal.us.es/marques/>

[47] L. J. Rogla, J. Carbonell and V.E. Boria, “Study of equivalent circuits for open-ring and split-ring resonators in coplanar waveguide technology”, *IET Microwaves, Antennas and Propagation*, vol. 1, pp. 170–176, Feb 2007.

- [48] A. L. Borja, J. R. Kelly, A. Belenguer, J. Cascon and V. E. Boria, “Compact coplanar waveguide metamaterial-inspired lines and its use in highly selective and tunable bandpass”, *Metamaterial*, Chapter 23, pp. 600-619, InTech, May 2012.
- [49] F. Falcone, F. Martin, J. Bonache, R. Marqués, M. Sorolla, “Coplanar waveguide structures loaded with split-ring resonators,” *Microwave and Optical Technology Letters*, vol. 40, no. 1, Jan. 2004.
- [50] I. Gil, J. Bonache, J. García-García, F. Falcone and F. Martin, “Metamaterials in Microstrip Technology for Filter Applications” *Antennas and Propagation Society International Symposium*, vol.1A, pp.668-671, July 2005
- [51] F. Paredes, G. Z. Gonzalez, J. Bonache, and F. Martin, “Dual-Band Impedance-Matching Networks Based on Split-Ring Resonators for Applications in RF Identification (RFID),” *IEEE Transactions on Microwave Theory and Techniques*, vol.58, no.5, pp.1159-1166, May 2010.
- [52] M. Gil, J. Bonache, J. Selga, J. García-García and F. Martín “High-pass filters implemented by Composite Right/Left Handed (CRLH) transmission lines based on complementary split rings resonators (CSRRs)”, *PIERS Online*, vol. 3, no. 3, 2007.
- [53] J. Bonache, M. Gil, I. Gil, J. Garcia-Garcia and F. Martin, ‘Limitations and solutions of resonant-type metamaterial transmission lines for filter applications: the hybrid approach,’ *IEEE MTT-S International Microwave Symposium Digest*, pp. 939-942, June 2006
- [54] J. Bonache, I. Gil, J. Garcia-Garcia, and F. Martin, “Novel microstrip band pass filters based on complementary split-ring resonators,” *IEEE Transactions on Microwave Theory and Techniques*, vol. 54, pp. 265–271, Jan. 2006.
- [55] M. Gil, J. Bonache and F. Martín, “Synthesis and applications of new left handed microstrip lines with complementary split-ring resonators etched on the signal strip,” *IET Microwaves, Antennas and Propagation*, vol.2, no. 4, pp. 324-330, Jan. 2008.
- [56] J. Naqui, M. Duran-Sindreu, A. Fernandez-Prieto, F. Mesa, F. Medina and F. Martin, “Multimode propagation and complex waves in CSRR-based transmission-line metamaterials,” *IEEE Antennas and Wireless Propagation Letters*, vol.11, no., pp. 1024-1027, Sept. 2012
- [57] I. A. I. Al-Naib and M. Koch, “Coplanar waveguides incorporating SRRs or CSRRs: a comprehensive study,” *Progress in Electromagnetics Research B*, vol. 23, pp. 343-355, 2010.

- [58] I. Gil, F. Martin, X. Rottenberg and W. De Raedt, "Tunable stop-band filter at Q-band based on RF-MEMS metamaterials," *Electronics Letters*, vol. 43, no.21, pp.1153-1154, Oct. 2007.
- [59] I. A. I. Al-Naib and M. Koch, "Coplanar waveguide metamaterials: The role of bandwidth modifying slots," *Applied Physics Letters*, vol. 91, pp. 113517 (1)-113517 (9), Sept. 2007.
- [60] M. Duran-Sindreu, P. Velez, J. Bonache, and F. Martin, "Broadband microwave filters based on Open Split Ring Resonators (OSRRs) and Open Complementary Split Ring Resonators (OCSRrs): improved models and design optimization," *Radioengineering*, vol. 20, no. 4, pp. 775–783, 2011.
- [61] M. Duran-Sindreu, "Miniaturization of Planar Microwave Components Based on Semi-Lumped Elements and Artificial Transmission Lines," PhD Thesis, Universitat Autònoma de Barcelona, 2011.
- [62] Jia-Sheng Hong and M. J. Lancaster, *Microstrip Filters for RF/Microwave Applications*, John Wiley & Sons, Inc., 2001.
- [63] P. Vélez, J. Naqui, M. Durán-Sindreu, J. Bonache, and F. Martín, "Broadband microstrip bandpass filter based on open complementary split ring resonators," *International Journal of Antennas and Propagation*, article ID 174023, Oct. 2012.
- [64] M. Duran-Sindreu, A. Velez, F. Aznar, G. Siso, J. Bonache and F. Martin "Applications of Open Split Ring Resonators and Open Complementary Split Ring Resonators to the Synthesis of Artificial Transmission Lines and Microwave Passive Components," *IEEE Transactions on Microwave Theory and Techniques*, vol.57, no.12, pp. 3395-3403, Dec. 2009.
- [65] M. Durán-Sindreu, G. Sisó, J. Bonache, F. Martin, "Planar Multi-Band Microwave Components Based on the Generalized Composite Right/Left Handed Transmission Line Concept," *IEEE Transactions on Microwave Theory and Techniques*, vol.58, no.12, pp. 3882-3891, Dec. 2010
- [66] F. J. Herraiz-Martínez, G. Zamora, F. Paredes, F. Martin, and J. Bonache, "Multiband printed monopole antennas loaded with OCSRrs for PANs and WLANs," *IEEE Antennas and Wireless Propagation Letters*, vol.10, pp. 1528-1531, Dec. 2011.

CHAPTER 3

Optimization

3.1 Introduction

3.2 Space Mapping

3.2.1 Concept and classical formulation

3.2.2 State of the art

3.3 Application Examples

3.3.1 Aggressive Space Mapping (ASM)

3.3.1.1 Determination of initial layout

3.3.1.1.1 TLs based on CSRRs

3.3.1.1.2 TLs based on OCSRRs

3.3.1.2 Parameter Extraction

3.3.1.2.1 TLs based on CSRRs

3.3.1.2.2 TLs based on OCSRRs

3.3.1.3 Automated Synthesis

3.3.1.3.1 TLs based on CSRRs

3.3.1.3.2 TLs based on OCSRRs

3.3.2 ASM + Line Search

3.3.3 Identification of a convergence region

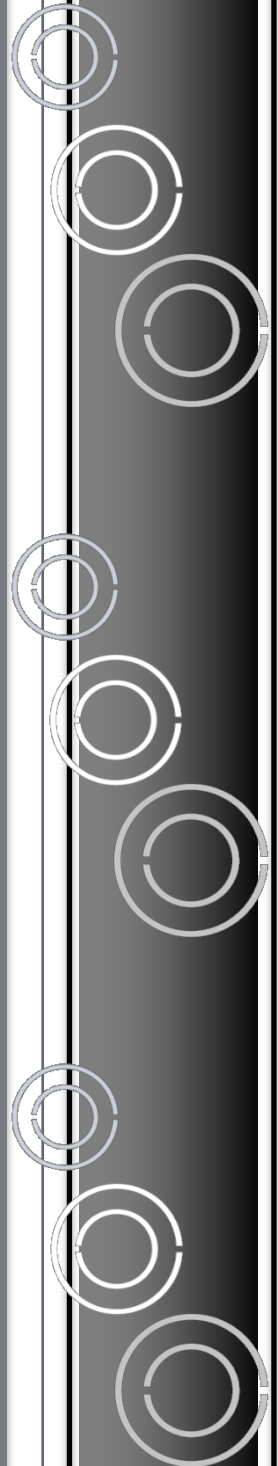
3.3.3.1 TLs based on CSRRs

3.3.3.2 TLs based on OCSRRs

References

*“Constrained optimization is the art of
compromise between conflicting objectives.
This is what design is all about”*

William A. Dembski



3 OPTIMIZATION

Optimization theory is the branch of mathematics focused on the quantitative study of optima and the different methods to reach them. The existence of optimization methods dates back to the times of Newton, Lagrange, and Cauchy. In spite of the optimization concept is automatically linked to mathematics; it is actually a multidisciplinary activity shared by many areas of knowledge as economics, physics or engineering. Daily expressions such as efficient energy consumption, time scheduling, profit maximization and internet routing do have inherent the concept of optimization (time, money, resources are limited), even we are not aware of it most of the time. In this chapter a small overview about optimization is given first (mainly from a design engineering point of view). Next we will focus on space mapping techniques (SM), since it is the methodology used to automate the synthesis of transmission lines based on MTMs concept, previously introduced in chapter 2. A brief explanation about Line Search (LS) algorithm is also given as it was an improvement introduced in some stage of the work in order to increase robustness and/or convergence of the SM algorithm. After discussing this approach, we describe an alternative technique for determining a suitable convergence region, which provides a very good starting point enhancing robustness and efficiency.

3.1 Introduction

Any problem in which certain parameters need to be determined to satisfy certain constraints can be formulated as an optimization problem. Basically, optimization can be described as the process to find the design vector $x = (x_1, x_2, \dots, x_n)$ that minimizes one or multiple cost/objective functions f_i :

$$\text{minimize } f_i(x), \quad (i = 1, 2, \dots, M) \tag{3.1}$$

constrained to

$$\begin{aligned} h_j(x), & \quad (j = 1, 2, \dots, J) \\ g_k(x) \leq 0 & \quad (k = 1, 2, \dots, K) \end{aligned} \tag{3.2}$$

where f_i , h_j and g_k are in general non-linear functions. If $M > 1$, the optimization is called multiobjective or multicriteria [1-2]. And only in the particular case

when $K=0$, it becomes an equality-constrained optimization problem. The parameters to optimize (design variables) are quite different according to the type of application or the nature of the problem. Starting from an approximate trial/analytical solution, the algorithm will gradually refine the solution until a predetermined level of precision has been reached. A good algorithm can be expected to converge to a maxima or minima when given a sufficiently good starting value. On many occasions, the optimization problem is determined by finding the maximum of the objective function/s instead of the minimum. Maximization problems can be cast into the form of equation (3.1) through the simple transformation:

$$\text{maximize } (f_i(x)) = \text{minimize } (-f_i(x)), \quad (i = 1, 2, \dots, M) \quad (3.3)$$

Objective functions that appear in design engineering, may come from computer simulations, since there is not an explicit analytical form, and the dependence of the objective function on design variables is complex and implicit. This type of simulations can be very demanding in terms of time and CPU consumption because the structures are often complex and the accuracy needed is high. Considering that almost all optimization algorithms are iterative, having a good optimization strategy can reduce in a significant way the global cost. In spite of great advances on computing power and even commercial software is often providing already parallel computation; robust and efficient optimization methodologies are still a must, or at least they lead to a more efficient way to use the resources.

Many optimization algorithms can be found in the literature [1-5], however there is no a single algorithm suitable to solve whatever problem. Optimization algorithms are classified according to different criteria: if the method is gradient-based (derivative-based) or not, trajectory-based or population-based, deterministic or stochastic, etc. Among the most relevant algorithms in literature, we highlight: Quasi-newton, minimax, simplex, sequential quadratic programming (SQP), trust-region methods, pattern search, genetic, neural network methods, space mapping, nature-inspired, etc. And at present time, new algorithms or different improvements/approaches are continuously arising.

Once the problem is properly formulated, there are different issues that should be taken into account before starting the optimization process, such as:

- Initial point calculation. The better starting point the sooner convergence is achieved. A bad initial point can even lead into the non-convergence of the algorithm. Therefore, it is a crucial step in the optimization process, especially in deterministic algorithms where the next candidate is determined based on the previously collected information (it is not a random decision), and algorithm may be trapped in local minima.
- Algorithm choice. The main way to reduce the number of evaluations of the objective function is to use an efficient algorithm. There are a wide variety of optimization algorithms, so it should be chosen according to the several characteristics/features that define the optimization problem. That means to study/identify if the problem: presents constraints, is linear, the objective functions are noisy, has a unique solution, is continuous... Sometimes, the choice of a proper combination of algorithms may lead to achieve better results (hybridization of algorithms) than just using a single algorithm for all the optimization process.
- Simulator choice. In terms of computation time and cost, the use of an efficient evaluator (or simulator) is very important. For engineering and industrial applications, a numerical simulator (e.g. an EM-solver) is usually employed to solve the objective function/s. Due to the high cost of complex simulations; optimization is sometimes performed in different stages. In first term, a fast and less accurate solver is used (e.g. for 2.5D structures), and when getting closer to the target/solution a more accurate tool but slower (for 3D structures) is used instead.

Optimization and computation advancements lead to solve problems more effectively than ever, and even some that previously were beyond of reach. However, applying optimization in a straightforward way, i.e., by applying direct optimization routines to EM simulation, can be unpractical and still very time consuming. This is the reason why different techniques that avoid direct optimization of the structure, as underlined in the first chapter, are widely used to synthesize complex microwave devices. These techniques can be globally referred as surrogate-model-based methods (SB) [5]. The optimization burden shifts from an expensive “fine” (high-fidelity) model to a cheap “coarse” (surrogate) model which is iteratively optimized and updated. The optimization process of these methods can be summarized as follows and graphically shown in Fig. 3.1:

1. Generate the initial surrogate model.

2. Obtain an approximate solution to the problem by optimizing the surrogate.
3. Evaluate the high-fidelity model at the approximate solution computed in Step 2.
4. Update the surrogate model using the new high-fidelity model data.
5. Stop if the termination condition is satisfied; otherwise go back to Step 2.

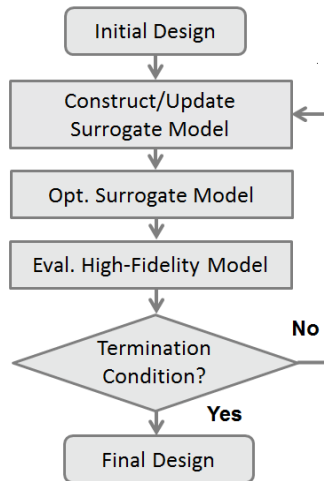


Fig. 3.1. - Flowchart of the Surrogate-Based Optimization process.

A lot of research effort has been focused on developing methods and techniques to construct appropriate surrogate models of high-fidelity simulation models, as well as in the enhancement of surrogate-based algorithms. Probably the most popular approach of SB optimization is space mapping (SM) [6]. Proof of this is that such topic is included in some sessions of many international conferences (e.g. IEEE International Microwave Symposium, IEEE International Symposium on Antennas and Propagation, etc.) and there is even an international workshop just focused on the space mapping techniques (SMSEO: “International Workshop on Surrogate Modelling and Space Mapping for Engineering Optimization” [7]).

A general overview of SM is giving in the next section, without going deep into details through every single version or enhancement published, due the high number of available publications and for the sake of brevity. Among the different versions, in order to automate the synthesis of artificial transmission lines, we have chosen to use Aggressive Space Mapping (ASM) [8]. It is a

conceptually simple approach and easy to implement. The use of a much more efficient initialization of the algorithm and the use of Broyden updates, results in a remarkable improved performance of the original SM algorithm.

3.2 Space Mapping

This year we celebrate the 20th anniversary of Space Mapping algorithm, which was firstly formulated by Bandler [6]. Several improvements or versions have been published since then [8-12], and even it was originally orientated to the optimization of microwave devices [11], its application fields are growing, being successfully used in electromechanics [13], automotive [14], aeronautics (structural optimization) [15] or (fluid) transport processes [16].

3.2.1 Concept and classical formulation

Space mapping techniques are intended for optimization problems which involve very expensive function evaluations. It is assumed that there are two different models that can describe the same physical system/structure. An expensive model of primary interest (known as fine model), and a cheaper (denoted coarse model) which is assumed to be less accurate but much faster. The coarse model is physics-based using a simplified representation of the microwave structure in question, for example, an equivalent circuit. In the case of microwave devices, when there is not an accurate/reliable circuit model (e.g., for complex structures), a less accurate EM simulation model can be employed instead (such as the use of a coarse mesh, less number of modes, discrete source versus waveguide port, etc.). Ideally, the evaluation cost of the coarse model should be negligible when compared to the evaluation cost of the fine model. However, the quality of the coarse model must be good enough, or close to the fine model, for a good performance of the algorithm; otherwise it can lead to the non convergence of the algorithm.

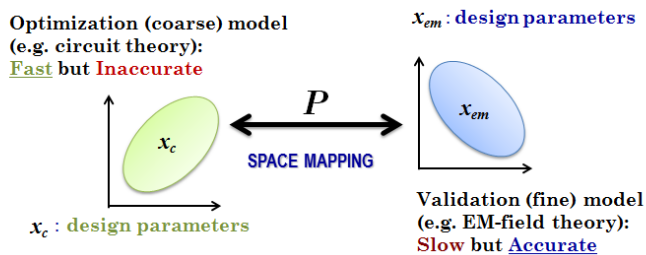


Fig. 3.2. – Concept of Space Mapping.

The idea behind space mapping is to find a mapping function “ P ” that relates the parameters of the coarse model (e.g. circuit values, denoted by vector x_c), and the parameters of the fine model (e.g. physical dimensions, denoted by vector x_{em}), and to use this mapping for finding an optimal set of parameters for the fine model, see Fig. 3.2. By exploiting the knowledge embedded in the coarse model, direct optimization of the fine model is avoided. In other words, the optimization burden is shifted to an inexpensive but reasonable accurate coarse model [6].

Expressed in a mathematical language, the target of SM is to find a mapping P relating the fine and coarse model parameters as:

$$x_c = P(x_{em}) \quad (3.4)$$

such that

$$R_c(P(x_{em})) \approx R_{em}(x_{em}) \quad (3.5)$$

in the region of interest. The vectors x_c and x_{em} are the design parameters in every space, being x_c and $x_{em} \in \mathcal{R}^{n \times 1}$, whereas R_c and R_{em} are the corresponding model responses, with R_c and $R_{em} \in \mathcal{R}^{m \times 1}$. Typically, R_{em} is evaluated just once for each iteration of the algorithm (for every new design $x_{em}^{(i+1)}$), and for EM applications it is usually chosen the magnitude of a transfer function at m chosen frequencies (e.g. $|S_{21}|$). After a small number of iterations, let us say K , it is likely to find a fine model vector that satisfies:

$$x_{em}^{(K)} = \overline{x_{em}} = P^{-1}(x_c^*) \quad (3.6)$$

where x_c^* is the target coarse model vector, determined with a coarse model optimization. The notation $\overline{x_{em}}$ is typically used when referring to the mapped fine model solution, in opposition to x_{em}^* , in order to remark that it can be just a good enough approximation of the optimum solution.

In this first approach of SM, an initial approximation of the mapping $P^{(0)}$ is obtained by performing fine model evaluations at a preselected set of m_0 points, with $m_0 \geq n + 1$. If the design parameters in both spaces are the same, the natural choice is to take one of the points as $x_{em}^{(0)} = x_c^*$. In case that the coarse model is an equivalent circuitual model, initial design parameters can be inferred by means of analytical formulas, which relate approximately the circuit values with real dimensions (solution should be not too far from the final

solution). The remaining $m_0 - 1$ base points are chosen by small perturbations (all points are in the neighborhood) around $x_{em}^{(0)}$. Next, a set of coarse model solutions is obtained by a parameter extraction process (PE):

$$x_c^{(j)} \triangleq \arg \min_{x_c} \|R_{em}(x_{em}^{(j)}) - R_c(x_c)\| \quad (3.7)$$

where $\|\cdot\|$ indicates a suitable norm.

It must be pointed out that for resonant type MTM TLs, the equivalent circuit is chosen as coarse model, and there is not real optimization in the optimization space, since straight forward parameter extraction techniques are used, as it will be explained later. This fact makes that the algorithm runs faster.

With the m_0 points evaluated, the first mapping approximation $P^{(0)}$ is established, which is function of some linear and predefined fixed functions f pondered by weighting factors to emphasize/minimize the influence of certain points. The SM is an iterative process, where a new mapping function $P^{(j)}$ is estimated at each iteration (based on the previous point evaluations and weights) which leads to the obtainment of a new design (point):

$$x_{em}^{(j+1)} = (P^{(j)})^{-1}(x_c^*) \quad (3.8)$$

If the new design suffices the following expression:

$$\|R_{em}(P(x_{em}^{(j+1)})) - R_c(x_c^*)\| < \eta \quad (3.9)$$

with η a fixed small positive constant ($\eta \rightarrow 0$), the algorithm converges where $P^{(j)}$ is the desired P . The algorithm continues iterating if the previous conditions is not satisfied, or the maximum number of iterations N_{max} of the algorithm is not reached ($j+1 < N_{max}$).

This algorithm, even useful in many cases, has some drawbacks that the different proposed enhancements have tried to minimize or solve, by combining SM with other optimization strategies. Some of the identified drawbacks are: high-cost to initiate the algorithm, no uniqueness in the PE process, lineal mapping (that cannot be a good choice when misalignment between models is high).

3.2.2 State of the art

In the first version of space mapping [6], the mapping P was estimated on the basis of some predefined weighted fundamental functions and the evaluation of different designs. One year later, Bandler et al. proposed Aggressive Space Mapping (ASM) [8], which is a more efficient version that solved the problem using the Broyden's method for non-linear equations [17]. Hence, ASM iteratively solves the non-linear system given by:

$$f(x_{em}) = 0 \quad (3.10)$$

where

$$f(x_{em}) = P(x_{em}) - x_c^* \quad (3.11)$$

Let $x_{em}^{(j)}$ be the solution of (3.11) at the j -th iteration. The next iterate $x_{em}^{(j+1)}$ is found by applying a quasi-newton step $h^{(j)}$:

$$x_{em}^{(j+1)} = x_{em}^{(j)} + h^{(j)} \quad (3.12)$$

where $h^{(j)}$ is calculated according to:

$$B^{(j)} \cdot h^{(j)} = -f(x_{em}^{(j)}) = -f^{(j)} \quad (3.13)$$

with $B^{(j)}$ an approximation of the Jacobian matrix J of the vector f with respect to x_{em} at the j -th iteration:

$$J(x_{em}^{(j)}) = \left[\frac{\partial f^T(x_{em})}{\partial x_{em}} \right] \Bigg|_{x_{em}=x_{em}^{(j)}} \quad (3.14)$$

but updated according to the classic Broyden formula in every iteration as:

$$B^{(j+1)} = B^{(j)} + \frac{f(x_{em}^{(j)} + h^{(j)}) - f(x_{em}^{(j)}) - B^{(j)} \cdot h^{(j)}}{h^{(j)T} h^{(j)}} h^{(j)T} \quad (3.15)$$

Incorporating (3.13) to (3.15), the previous expression can be simplified to:

$$B^{(j+1)} = B^{(j)} + \frac{f^{(j+1)} h^{(j)T}}{h^{(j)T} h^{(j)}} \quad (3.16)$$

This algorithm is presented in more detail in section 3.3, with its flowchart diagram, and some application examples. Anyway, the main novelties of the ASM published in [8] can be summarized as:

- PE is improved in order to add robustness to the algorithm.
- Initiation of the algorithm is more efficient (B matrix is typically initiated as the identity matrix).
- Determination of next design is generated not only in base to the base point for establishing the mapping, but also as a step forward to SM solution (quasi-Newton iteration).

In the same paper where ASM was introduced, i.e. [8], another version of SM called Frequency SM (FSM), and depicted in Fig. 3.3.b, was introduced. As it is graphically described, the frequency variable ω , as well as the design parameters x_{em} , are mapped being as a result an improvement of the parameter extraction process, and consequently of the whole optimization process. An enhancement of this method can be considered the generalized space mapping (GSM) [9], orientated to improve microwave device modelling.

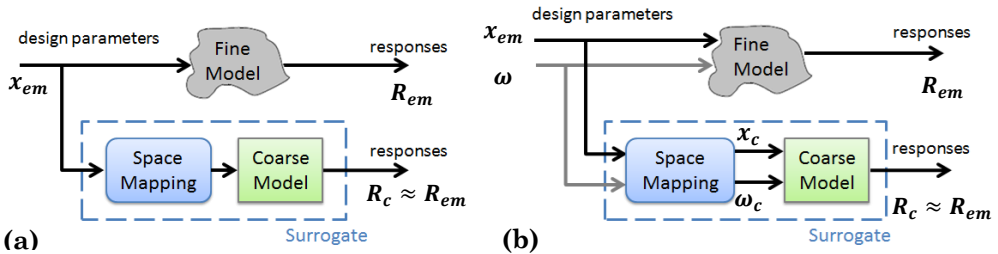


Fig. 3.3. – (a) Space Mapping Concept. (b) Frequency Space Mapping Concept (first introduced in [8]).

Afterwards, Bakr et al. introduced trust-region methodology to enhance the global convergence properties of ASM [10]. This enhancement is known as TRASM in acronym form, but there are also others approaches of SM which includes trust region methods, being most of them summarized in [18]. The idea of trust-region methods is to adjust the length of the step taken at each iterate according to how well the model predicts the objective function. A trust-region sub-problem is solved within a certain trust region, to minimize $\|f^{(j+1)}\|$. At every iteration j , a linear function $L^{(j)}$ is used to locally approximate $f(x_{em}^{(j)})$, such that:

$$L^{(j)}(x_{em}^{(j)} + h^{(j)}) = f(x_{em}^{(j)}) + B^{(j)} \cdot h^{(j)} \quad (3.17)$$

The approximated model is trusted to represent the objective function only within a region of specific radius around the current j -th iteration. Hence, $h^{(j)}$ is determined by solving a trust-region sub-problem given by

$$h^{(j)} = \arg \min_h \|L^{(j)}(x_{em}^{(j)} + h)\| \quad (3.18)$$

subject to

$$\|h\| \leq \delta^{(j)} \quad (3.19)$$

where $\delta^{(j)}$ is the trust-region size. Hence the step length is constrained to the region size. The new iterates are accepted only if they are descent directions for $\|f\|$. If the model minimum achieves sufficient reduction in the objective function, the trust-region size is increased. If insufficient reduction is achieved, the trust region is reduced. Otherwise the trust region is kept unchanged. Solving equations (3.18) and (3.19) is equivalent to solve the following expression:

$$(B^{(j)T} B^{(j)} + \lambda I) h^{(j)} = -B^{(j)T} \cdot f^{(j)} \quad (3.20)$$

where λ can be chosen such that the step is identical to (3.17). The trust region method ensures that each iteration results in improved alignment between the coarse and fine models. The trust-region ASM also includes multipoint parameter extraction (MPE) that exploits the available information about the mapping between both spaces, improving the uniqueness of parameter extraction.

Thinking in cases where spaces are seriously misaligned, another improvement to ASM was introduced, which is known as Hybrid Aggressive Space Mapping (HASM). It exploits both the trust-region aggressive space-mapping (TRASM) strategy and direct optimization [19]. In the first phase a TRASM strategy is used. The second phase minimizes $\|R_{em}(x_{em}) - R_c(x_c^*)\|$ through direct least-squares optimization. It enables smooth switching from SM optimization to direct optimization if SM fails. The direct optimization phase utilizes all the available information accumulated by SM optimization about the mapping between the coarse and fine-model spaces (J_{em}). The

algorithm also enables switching back from direct optimization to SM if SM is potentially convergent (updating B), see Fig. 3.4.

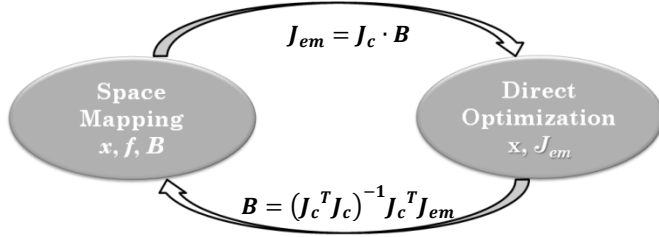


Fig. 3.4. – Connection between SM and direct optimization in HASM [19].
 J_{em} and J_c are the Jacobians of the fine and coarse models respectively.

SM optimization was also enhanced by using surrogate models introduced by the same research group, i.e. Bakr et al. [20]. Surrogate model-based SM optimization exploits a surrogate in the form of a convex combination of a mapped coarse model (MCM) and a linearized fine model (LFM). The algorithm employs the trust-region method, where the surrogate replaces the formal approximation to a linear or quadratic model. The accuracy of the surrogate model is improved using the generated fine-model simulations at every iteration of the algorithm. At the j -th iteration, the surrogate model response $R_s \in \mathcal{R}^{m \times 1}$ is given by:

$$R_s^{(j)}(x_{em}) \triangleq \lambda^{(j)} R_m^{(j)}(x_{em}) + (1 - \lambda^{(j)}) (R_{em}(x_{em}^{(j)}) + J_{em}^{(j)} \Delta x_{em}) \quad (3.21)$$

with $\lambda^{(j)} \in [0,1]$ and $J_{em}^{(j)} \in \mathcal{R}^{m \times n}$ an approximation of the Jacobian of the fine model responses at $x_{em}^{(j)}$. Moreover, $R_m^{(j)}(x_{em})$ is the mapped coarse model response and $(R_{em}(x_{em}^{(j)}) + J_{em}^{(j)} \Delta x_{em})$ is the linearized model response. Hence, the parameter $\lambda^{(j)}$ determines which model weights more. If $\lambda^{(j)}=1$, the surrogate becomes an MCM, that uses the linear frequency space mapping. On the contrary if $\lambda^{(j)}=0$ it becomes an LFM, that ensures that the algorithm will work even if the coarse model is poor. Initially $\lambda^{(0)}=1$, but later on it is updated to favor the more accurate model, based on the predicted errors.

The step $h^{(j)}$ at the j -th iteration is obtained by solving:

$$h^{(j)} = \arg \min_{h^{(j)}} U \left(R_s^{(j)}(x_{em}^{(j)} + h^{(j)}) \right), \quad \|h\| \leq \delta^{(j)} \quad (3.22)$$

where $U(R_S^{(j)}(x_{em}^{(j)} + h^{(j)}))$ is the value of the objective function evaluated using the surrogate model at $x_{em}^{(j)} + h^{(j)}$, and $\delta^{(j)}$ is the trust-region size. The point $x_{em}^{(j)} + h^{(j)}$ is accepted if it improves the fine-model objective function. Otherwise, the accuracy of $R_S^{(j)}(x_{em})$ should be improved. For more details, see [20].

Another interesting variation of SM is Neural SM, with its different approaches [11, 21]. The main idea is to construct a non-linear multi-dimensional vector mapping function P from the fine to the coarse input space using an artificial neural network (ANN). This can be done in a variety of ways, in order to make a better use of the coarse model information for developing the neuromodel. The implicit knowledge in the coarse model, that can be considered as an “expert”, not only allows to decrease the number of learning points needed, but also to reduce the complexity of the ANN and to improve the generalization performance.

In the Space Mapped neuromodeling (SMN) approach the mapping from the fine to the coarse parameter space is implemented by an ANN, see Fig. 3.5. We have to find the optimal set of the internal parameters of the ANN (weighting factors, bias, etc.), such that the coarse model response is as close as possible to the fine model response for all the learning points.

The mapping can be found by solving the following optimization problem:

$$\min_w \|[e_1^T, e_2^T \dots e_l^T]\| \quad (3.23)$$

where w is the vector which contains the internal parameters of the neural networks, l is the total number of learning samples, $\|\cdot\|$ denotes the Huber norm, and e_k is the error vector given by:

$$e_k = R_{em}(x_{em_i}, \omega_j) - R_c(x_c, \omega_j) \quad (3.24)$$

$$x_c = P(x_{em_i}) \quad (3.25)$$

with $i = 1, \dots, B_p$; $j = 1, \dots, F_p$ and $k = j + F_p(i - 1)$. The term B_p denotes the number of training base points for the input design parameters and F_p is the number of frequency points per frequency sweep.

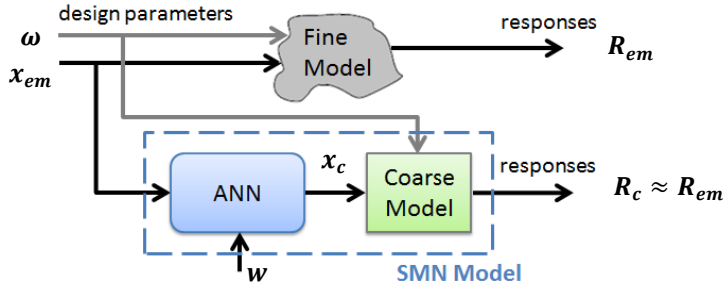


Fig. 3.5. – Space Mapped neuromodeling concept (SMN) [11]

Lately, the classical notation of space mapping has been reviewed and updated in order to accurately describe any SM process, and to unify the formulation with other surrogate model-based optimization processes formulation [22-24]. To enhance a coarse model response R_c , is created a surrogate model R_s , that using auxiliary mapping parameters (e.g. frequency), makes that R_s to be as similar as possible to R_c . So the standard model is defined as:

$$R_s(x) = R_s(x, p) \tag{3.26}$$

with x and p the design variables and model parameters respectively. So the generic space-mapping iteration is now described by:

$$x^{(j+1)} = \arg \min_x U(R_s(x, p^{(j)})) \tag{3.27}$$

with U being a suitable objective function. The vector of model parameters $p^{(j)}$ is obtained at iteration j using a parameter extraction procedure:

$$p^{(j)} = \arg \min_p \sum_{k=0}^j w_{j,k} \|R_{em}(x^{(j)}) - R_s(x^{(j)}, p)\| \tag{3.28}$$

where $w_{j,k}$ is the weighting factors that determine the contribution of previous iteration points to the parameter extraction process [22]. A common choice is to take $w_{j,k}=1$ for all j and all k . The surrogate model is normally the coarse model R_c composed with suitable transformations. Various SM surrogate models are available [11, 22], that can be categorized into four groups according to [24, 25] as follows:

- Models based on a distortion of the coarse model parameter, as for instance the input SM [22] where the coarse model is defined as $R_S(x, p) = R_S(x, B, c) = R_c(Bx + c)$.
- Models based on a distortion of the coarse model response, as it is the case of output SM [22], where $R_S(x, p) = R_S(x, d) = R_c(x) + d$.
- Implicit SM, where the parameters used to align the surrogate with the fine model are separated from the design variables [25], even though they are still physical variables, e.g. the height of the substrate.
- Custom model exploiting characteristics of a given design problem; the most typical example is frequency space mapping $R_S(x, p) = R_S(x, \omega) = R_c(x, \omega_c) = R_{c,f}(x, \omega)$, where $R_{c,f}$ is a frequency-mapped coarse model. The evaluated frequencies are different from the original frequency sweep of the fine model, see Fig. 3.3.b.

Since SM usually comprises several transformations, the model used in practice has the following generic form:

$$R_S(x, p) = R_S(x, A, B, c) = A \cdot R_{c,f}(Bx + c) + d \tag{3.29}$$

where $A = \text{diag}\{a_1, \dots, a_m\}$, B is an $n \times n$ matrix, c is an $n \times 1$ vector and d is an $m \times 1$ vector.

An important issue in SM approaches is also to choose the proper type of mapping. The SM techniques include input, implicit (pre-assigned parameters), and different variations of output space mapping, and also the mapping function (linear, nonlinear, neural). By combining these mappings in different configurations, one can adjust the flexibility of the space-mapping surrogate model, which is correlated with the number and type of space-mapping parameters. Figure 3.6 shows an example where implicit mapping is provided with an input and output mapping.

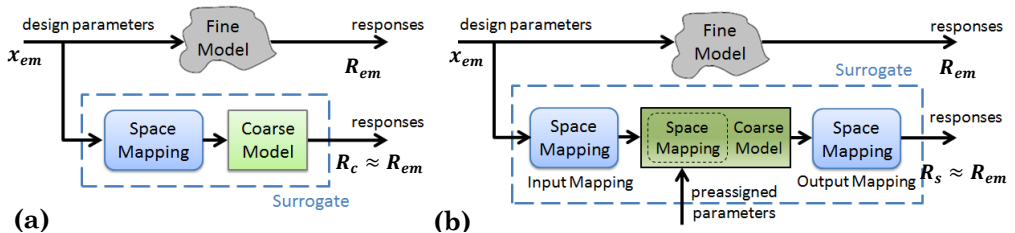


Fig. 3.6. - (a) Original Space Mapping, the mapping with the coarse model constitutes the “surrogate” [6]. (b) Implicit Space Mapping, with input and output mapping [25].

Some conventional SM algorithms have been also enhanced by using adjoint sensitivity [26-27]. This methodology helps to speed up the processes of SB model optimization process and PE, but also improves the matching between the surrogate and the fine model.

Before concluding this review about the state-of-the-art of SM, it is worth mentioning an expert approach called Tuning SM [28-29]. The Tuning space mapping (TSM) algorithm incorporates the port tuning method proposed for design using EM simulators [30]. They exploit physics-based tuning models (EM-simulated models plus tuning components such as capacitors, inductors or coupled-line models) as surrogates, see Fig. 3.7.a. These techniques involve a fine model (e.g., a full-wave EM simulation), auxiliary fine models (fine models with multiple internal tuning ports), a tuning model, and a calibration scheme that sometimes exploits an extra calibration (coarse) model. The corresponding flow chart of this kind of optimization is depicted in Fig. 3.7.b. There are different variants of TSM [29], which mostly differ in the construction of the tuning model, as well as in the calibration procedure.

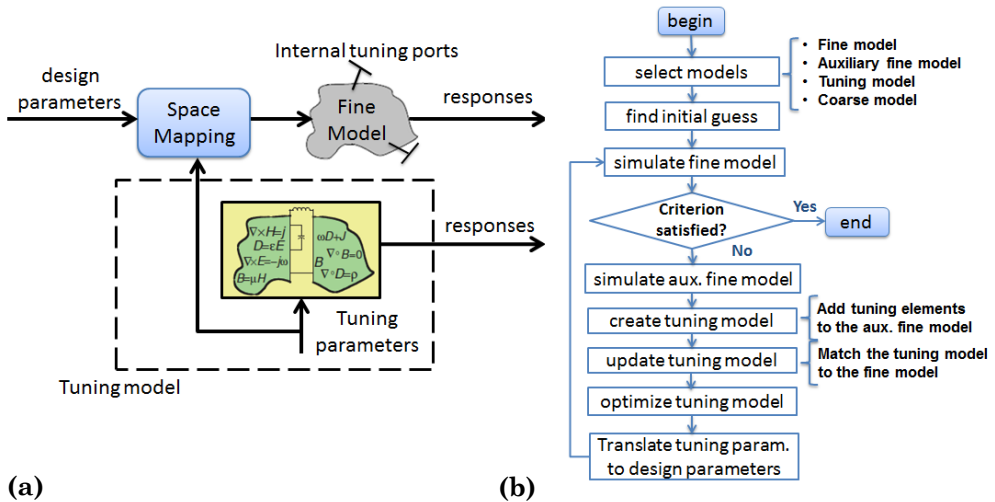


Fig. 3.7. - Tuning Space Mapping, (a) Concept diagram [28], (b) Flowchart [29].

Even SM is primarily used for optimization; it can be also used for modelling purposes [23, 31-32]. The most typical application of SM in this context is statistical analysis and yield estimation [31].

3.3 Application Examples

In the context of this work, we have applied ASM techniques to obtain automated synthesis of different unit cells of artificial transmission lines. As fine model, the full-wave EM model of the unit cell under study is used. On the other hand, the equivalent lumped circuit model of each cell is used as coarse model, because these equivalent circuits can accurately describe this kind of TLs in the working region. Such models have been widely studied in literature [33], and have been previously introduced in chapter 2.

In our application examples, we have considered the same number of parameters in both spaces (i.e. validation on optimization space) in order that the mapping matrix B (3.12-13) needs to be inverted, and in such a case we prevent the algorithm from potential instabilities. Hence, if the geometrical parameters that define the structure are bigger than the circuital parameters of the corresponding equivalent circuit, some of the physical dimensions are considered to have reasonable fixed values (e.g. diameter of via) or to be proportional to other geometrical variables included in the optimization. In the case represented in Fig. 3.8, the split of the rings is fixed to the value of the width of the slots (c), and the length of the strip is approximately set to twice the external radius of the CSRR (r_{ext}). This assumption is made taking into account that larger/smaller lengths of the line would lead to a different equivalent circuit models, and on the other hand that the CSRR sensitivity on the split size is not very high.

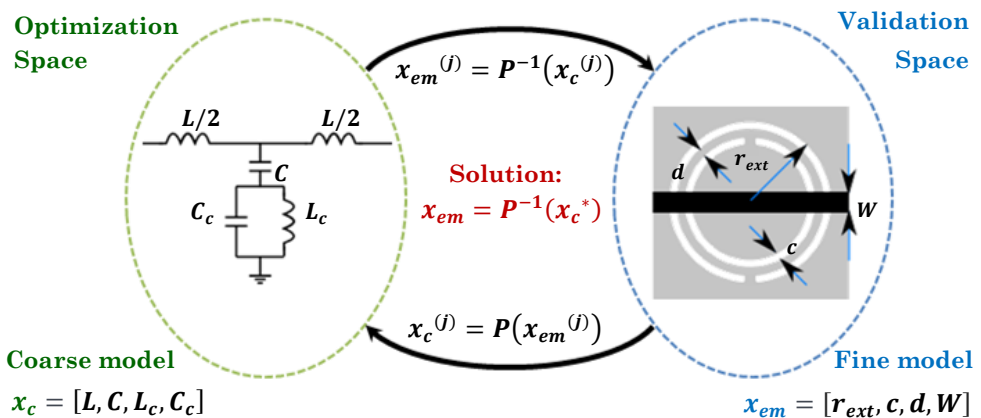


Fig. 3.8. - Application diagram for the negative permittivity unit cell. The coarse model is the equivalent circuit model, whereas the fine model is the EM model.

The first implemented cell is a microstrip line with a CSRR etched on the ground plane, just beneath the conductor strip as shown in the layout depicted in Fig. 3.8. Its equivalent circuit has already been presented in section 2.2.1.2, and can be seen in Fig. 3.8. It is a simple T-circuit model where the CSRR is modelled by a shunt LC tank of inductance L_c and capacitance C_c , then L is approximately the line inductance, and C is the coupling capacitance between the line and the CSRR. CSRR ohmic losses could be easily taken into account by just including a parallel resistance in the model [34], but in our case they were neglected. The corresponding series and shunt impedances are:

$$Z_{se_cell1} = j\omega L/2 \tag{3.30}$$

$$Z_{par_cell1} = j \left(\frac{\omega^2 L_c \cdot (C_c + C) - 1}{(1 - L_c C_c \omega^2) \cdot C \omega} \right) \tag{3.31}$$

This structure presents stop band behaviour over a narrow band, as it is shown in Fig. 3.9. The transmission zero is located at the frequency:

$$\omega_z = 2\pi f_z = \frac{1}{\sqrt{L_c(C_c + C)}} \tag{3.32}$$

With one of these unit cells, or by periodically cascading some of them, it can be implemented a notch (or stopband) filter [35-36]. Note that this line does not exhibit a right handed behavior, only a negative permittivity given by the presence of the CSRR.

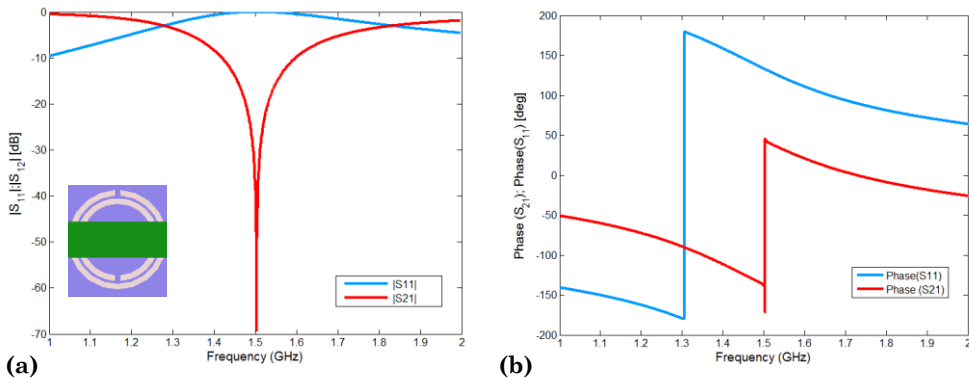


Fig. 3.9. - Typical magnitude (a) and phase (b) of the transmission coefficient of the CSRR-based artificial transmission lines shown in Fig. 3.8. $r_{ext}=4.46\text{mm}$, $c=0.44\text{mm}$, $d=0.23\text{mm}$, $W=3.10\text{mm}$.

The second implemented case is a modification of the example just presented, adding series gap to the host line, see Fig. 3.10.a. This is translated to the circuit model also by means of a π -model composed by two different capacitors, where C_s is the series capacitance and C_f represents the fringing capacitance; see Fig. 3.10.b. The other capacitance which appears in such figure is the capacitance of the line C_L . However, the equivalent circuit most commonly used is the simplified version shown in Fig. 3.10.c, obtained after applying a transformation from a π -model to a T-model reported in [37]:

$$2 C_g = 2 C_s + C_f + C_L \quad (3.33)$$

$$C = \frac{(C_f + C_L)(2 C_s + C_f + C_L)}{C_s} \quad (3.34)$$

As a result, the coarse model is defined by five parameters, i.e. $x_c = [L, C, L_c, C_c, C_g]$. On the other hand, the vector which defines the fine model is given by $x_{em} = [W, s, r_{ext}, c, d]$, the same set of parameters considered for the previous case, plus the length of the gap (s , see Fig. 3.10.a).

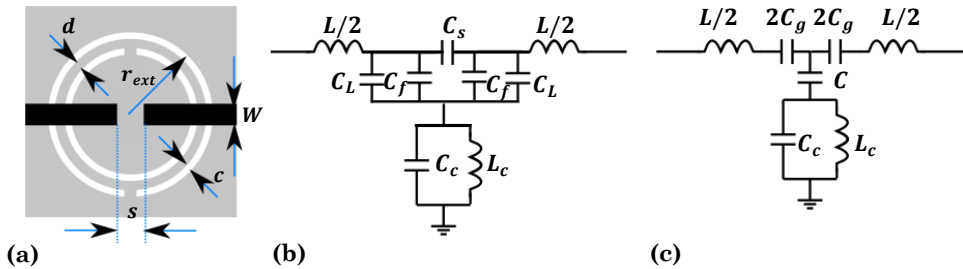


Fig. 3.10. - Layout (a), equivalent circuit (b), T-model transformation of the previous equivalent circuit (c).

According to schematic of Fig. 3.10.c, it follows that the series and shunt impedances for this unit cell are:

$$Z_{se_cell2} = \frac{j\omega L}{2} + \frac{1}{j\omega C_g} = j \frac{\omega^2 L C_g - 1}{2\omega C_g} \quad (3.35)$$

$$Z_{par_cell2} = Z_{par_cell1} = j \left(\frac{\omega^2 L_c \cdot (C_c + C) - 1}{(1 - L_c C_c \omega^2) \cdot C \omega} \right) \quad (3.36)$$

This structure does present a right-left handed behavior, which can be inferred from the study of the equivalent circuit and graphical representation of the dispersion phase characteristics (βd), see Fig. 3.11. The characteristic Bloch impedance, taking into account the expression (2.41), results:

$$Z_B = \sqrt{Z_{se}(Z_{se} + 2Z_{par})} = \sqrt{\frac{L}{C} \left(1 - \frac{\omega_{se}^2}{\omega^2}\right) + \frac{L}{C_c} \frac{\left(1 - \frac{\omega_{se}^2}{\omega^2}\right)}{\left(1 - \frac{\omega_{par}^2}{\omega^2}\right)} - \frac{L^2 \omega^2}{4} \left(1 - \frac{\omega_{se}^2}{\omega^2}\right)^2} \quad (3.37)$$

where $\omega_{se}^2 = 1/LC_g$ and $\omega_{par}^2 = 1/L_c C_g$ are the corresponding series and shunt resonance frequencies respectively. The upper limit of the left-handed band (LH) comes from the minimum of these frequencies, see Fig. 3.11. The transmission zero of the unit cell is at ω_z , which follows (3.32) expression, since the shunt impedance is identical for both structures. When there is no gap between the LH band and the RH band, i.e. the balanced case, then $\omega_{se} = \omega_{par} = \omega_0$, and expression (3.37) can be simplified to:

$$Z_B = \sqrt{\frac{L}{C} \left(1 - \frac{\omega_0^2}{\omega^2}\right) + \frac{L}{C_c} - \frac{L^2 \omega^2}{4} \left(1 - \frac{\omega_0^2}{\omega^2}\right)^2} \quad (3.38)$$

In that case a broad composite right-left-handed transmission band is achieved. The dispersion characteristic for the general case can be calculated according to (2.42) as:

$$\cosh(\beta d) = 1 + \frac{Z_{se}}{Z_{par}} = 1 + \frac{C}{C_g} \cdot \frac{(1 - \omega^2 L C_g)(1 - \omega^2 L_c C_c)}{(1 - \omega^2 L_c C_c)} \quad (3.39)$$

and in the balanced case, it can be simplified as follows:

$$\cosh(\beta d) = 1 + \frac{C(\omega^2 - \omega_0^2)^2}{2C_g \omega_0^4 (1 - \omega^2 L_c (C_c + C))} \quad (3.40)$$

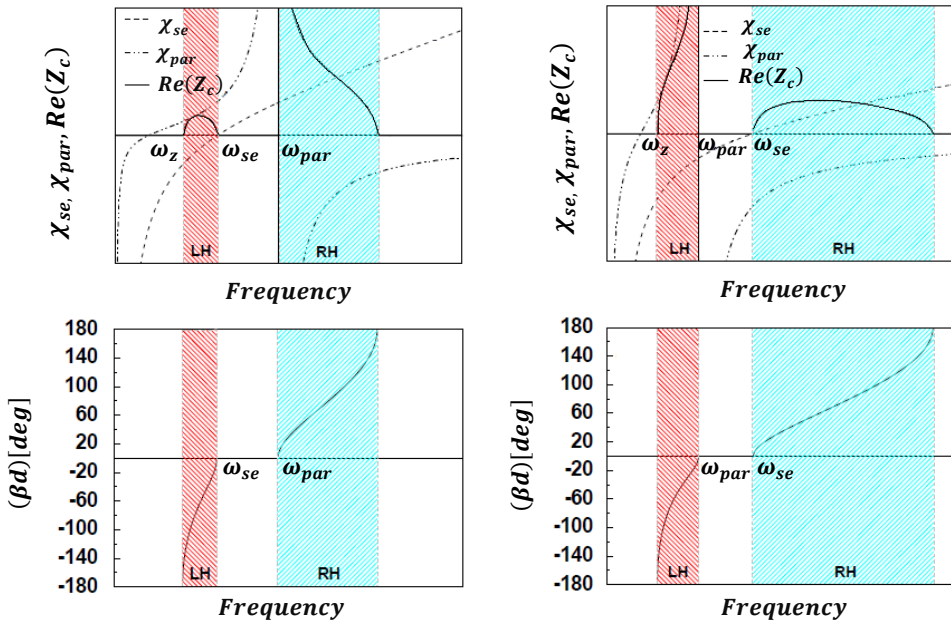


Fig. 3.11. - Representation of the series (χ_{se}) and shunt (χ_{par}) reactance, the characteristic impedance (Z_c) and the phase (βd) of a unit cell in Fig. 3.10. Two different cases are represented: $\omega_{se} < \omega_{par}$ and $\omega_{se} > \omega_{par}$ [38].

It is worth mentioning that in some cases, for example in order to obtain a balanced cell, the capacitance value C_g which is required cannot be achieved in general by a simple series gap, and a T-shaped gap or interdigital capacitor (meander-shaped) is used instead [38-39], see Fig. 3.12.

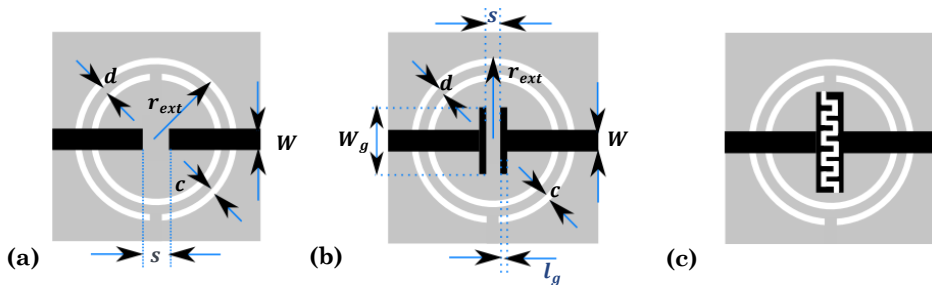


Fig. 3.12. - Layout of a CRLH unit cell where series gap presents different shapes: (a) flat, (b) T-shaped, (c) meandered.

The line with CSRRs and T-shaped gap was also automated with ASM, being the previous equivalent circuit and hence the PE method, valid for this cell too. In order to have also five variables in the validation space, the gap distance,

s , and the T-thickness, l_g , were set to a certain small value (as for example $l_g = s = 0.2\text{mm}$), and the width of the T-gap W_g is now an optimization variable. Another implemented option, was using, as we did before, s as optimization variable (Fig. 3.12.a) and considering l_g and W_g as a function of other optimization variables as follows: $l_g = r_{ext}/j$ and $W_g = kW$, where k and j are certain predetermined positive values.

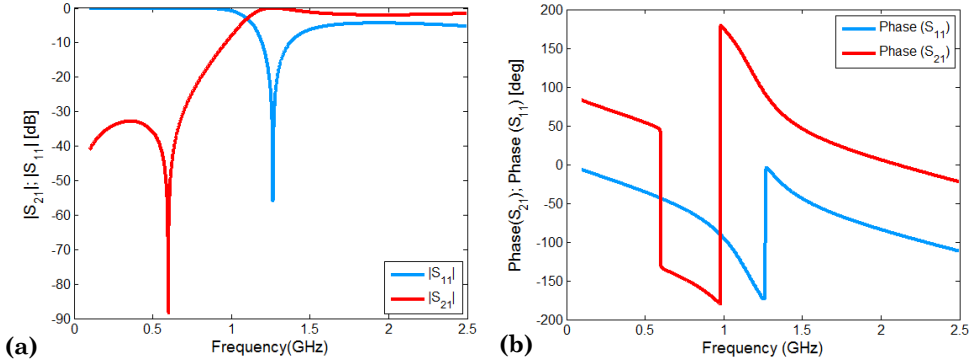


Fig. 3.13. - Typical magnitude (a) and phase (b) of the scattering parameters of a CSRR-based artificial transmission line like the one shown in Fig. 3.12.a.

A typical frequency response of the scattering parameters of this kind of cells is depicted in Fig. 3.13, which exhibits approximately a band-pass or high pass behavior. Usually several cells are cascaded in order to obtain a filter [39], but another possible application is to synthesize power dividers, where the required impedance inverters are implemented by means of single unit cells [40].

The third implemented example is an OCSRRL shunt connected to a microstrip line, as illustrated in Fig. 3.14.a. The circuit models of shunt-connected OCSRRL-loaded CPW and microstrip lines were outlined in section 2.2.1.3, but are discussed with more details in [41]. In microstrip technology, inductances present to model the phase shifting due to the host line are not necessary to be taken into account. The reason is that the reference ports are close enough to the contact point between the microstrip line and the OCSRRL, so the equivalent circuit of Fig. 2.26.c can be simplified to the one depicted in Fig. 3.14.b. Therefore, OCSRRL is modeled by the LC tank of inductance L_p and C_p , while L_{sh} models the presence of the strip between the inner metallic region of the OCSRRL and the ports (denoted as In and Out in the layout). The circuit simulation considering the parasitic element L_{sh} allows predicting both

the band-pass and the stop-band rejection. Three different parameters are considered as optimization variables at each space. The coarse model is defined by $x_c = [L_{sh}, L_p, C_p]$. In the validation space, just three of the geometrical dimensions are chosen as design variables, i.e. $x_{em} = [r_{ext}, d, e]$, and the rest ones are expressed as a function of the previous ones or taken as constant values. For example, the split of the inner ring is considered to be the minimum of the values for the width of the slots (c) and the width of the inner strip that opens the outer ring (e), i.e. $s_{inner} = \min(c, e)$. On the other hand, vias diameter is fixed to 0.4 mm or the width of the slots c is fixed to a small geometrical value, such as for instance $c = 0.2\text{mm}$.

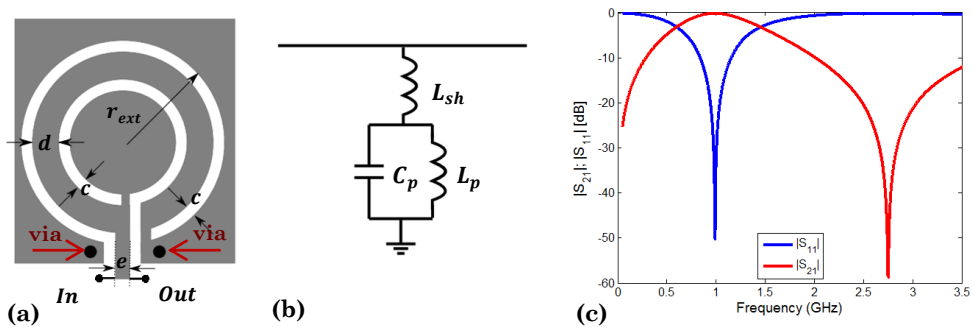


Fig. 3.14. - OCSR shunt connected to microstrip line. Unit cell layout (a), equivalent circuit (b), and frequency response of S-parameters magnitude (c).

Attending to the equivalent circuit, the frequency at which the transmission zero appears can be calculated as the frequency that makes the shunt impedance to be null, so:

$$\omega_z = 2\pi f_z = \sqrt{\frac{1}{C_p} \cdot \left(\frac{1}{L_p} + \frac{1}{L_{sh}} \right)} \quad (3.41)$$

The reflection zero frequency can be clearly identified too, as the frequency where the input admittance is zero, given by the following expression:

$$\omega_0 = 2\pi f_0 = \frac{1}{\sqrt{L_p C_p}} \quad (3.42)$$

A unit cell exhibits a band-pass response, as it is shown graphically in Fig. 3.14.c, followed by a stop-band. By concatenating several unit cells (as in previous cases), a wider band-pass filter can be achieved [42].

3.3.1 Aggressive Space Mapping (ASM)

The synthesis process of the abovementioned unit cells has been automated by means of a constrained version of ASM [31]. The use of constraints allows to avoid possible instabilities of the algorithm, as well as to reach unwanted solutions (from a practical realization point of view). In Fig. 3.15 the flowchart of the algorithm, particularized for our study cases, is depicted.

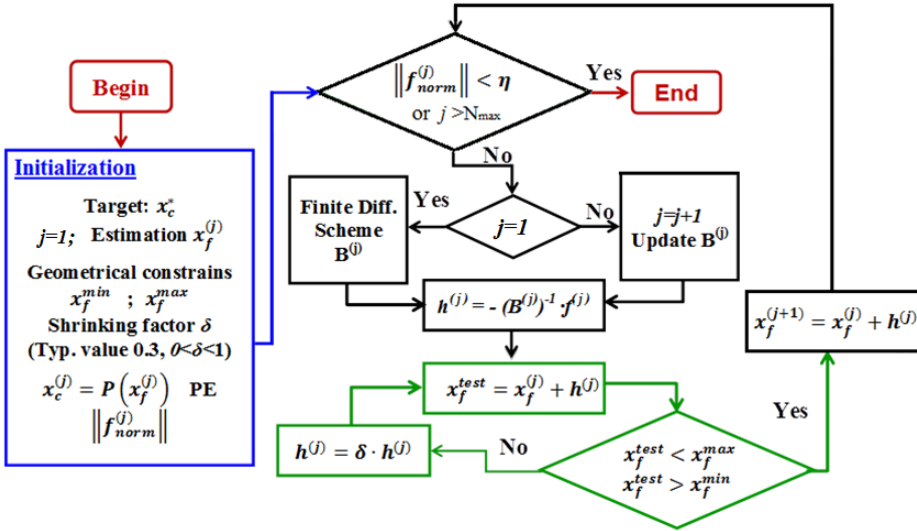


Fig. 3.15. - Illustration of the flow-diagram of the ASM algorithm with constrains.

Different colors are used in the above flow-diagram in order to clear distinguish the different stages involved:

- **Initialization** (blue). The vector x_c^* , which contains the electrical target parameters that describe the target response is considered to be data. Otherwise, it should be previously determined, by optimization, from certain given specs over the frequency target response (such as bandwidth, return losses, transmission zero, etc.), and even circuital (not all L_c/C_c ratios are implementable [37]) by optimization. The initial topology $x_f^{(1)}$ is estimated from x_c^* (further details can be found in subsection 3.3.1.1). Concerning to the constrained approach, some limits are imposed over the geometrical variables. The minimum reachable values are given by x_f^{min} . The limitation comes from the fact that too small dimensions may have an impossible implementation due to technological reasons. For instance, for the CSRR topology, the width of the slots (c^{min}) and the distance between them (d^{min})

are fixed to the minimum dimension achievable, and the external radius should be at least bigger than 3 times the slots width plus the distance between them ($r_{ext}^{min} > 3c+d$). On the other hand, the vector x_f^{max} imposes the upper limit of the variables since big dimensions will lead to the inaccuracy of the equivalent circuit model (used for the parameter extraction -PE- stage) [34], which is a critical issue for ASM convergence. The PE stage needed to obtain $x_c^{(j)}$ from $x_f^{(j)}$ simulation, and performed during the algorithm execution, is addressed in subsection 3.3.1.2.

- Core of ASM (black). The iterative process of the optimization algorithm was previously explained at the beginning of section 3.2.1. Some small considerations about the initialization of the matrix B (finite differences scheme) and the meaning of normalized error function (f_{norm}) are given later in this section (right after the next explanation about the constrained approach ASM).
- Constrained approach modification (green). When the next iterate $x_f^{test} = x_f^{(j+1)}$ exceeds the acceptable established limits, see Fig. 3.15, the step $h^{(j)}$ (3.12) is decreased in the same quasi-Newton direction by a shrinking factor δ ($0 < \delta < 1$). This factor is applied as many times as needed to $h^{(j)}$ until it becomes an acceptable solution. In the first implementations of the algorithm, as it is suggested in [31], the shrinking factor was set to 0.3 or 0.4. Afterwards, the value of delta was not fixed to a constant value during all the algorithm performance, and instead it was adjusted to the most limiting dimension, in order to make the solution x_f^{test} fulfill the allowed limits (δ_{min}). Note that the election of the shrinking factor can have a dramatically incidence in the evolution of the algorithm, as it is illustrated in Fig. 3.16. Therefore, choosing a bad value of δ can lead to a slow convergence of the algorithm. This effect can be somehow minimized with the introduction of line search, as it is shown in section 3.3.2.

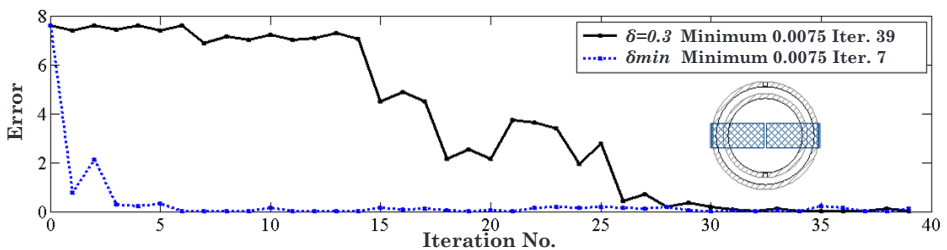


Fig. 3.16. - Illustration of the ASM algorithm evolution (error norm versus iteration number) in the case of a CSRR-based line (CRLH) using different shrinking factors. Target $x_c^* = [L, C, L_c, C_c, C_g] = [5.141\text{nH}, 14.841\text{ pF}, 2.635\text{ nH}, 2.812\text{ pF}, 0.773\text{ pF}]$.

The classical initialization of the ASM algorithm with the B matrix equal to the identity is not used, since different kinds of variables are handled (i.e. physical and electrical). A numerical derivative based approach has been used instead. To this extent, each geometrical parameter is slightly perturbed from the estimated initial value (perturbation smaller than 10%). The new layout is then simulated and the corresponding electrical parameters are extracted. Thus, to estimate the initial mapping matrix B , it is needed to perform as many EM simulations as parameters considered in the fine model. In the first case of study, the initial matrix is estimated as follows:

$$B^{(1)} = \begin{pmatrix} \frac{\partial L}{\partial W} & \frac{\partial L}{\partial r_{ext}} & \frac{\partial L}{\partial c} & \frac{\partial L}{\partial d} \\ \frac{\partial C}{\partial W} & \frac{\partial C}{\partial r_{ext}} & \frac{\partial C}{\partial c} & \frac{\partial C}{\partial d} \\ \frac{\partial L_c}{\partial W} & \frac{\partial L_c}{\partial r_{ext}} & \frac{\partial L_c}{\partial c} & \frac{\partial L_c}{\partial d} \\ \frac{\partial C_c}{\partial W} & \frac{\partial C_c}{\partial r_{ext}} & \frac{\partial C_c}{\partial c} & \frac{\partial C_c}{\partial d} \end{pmatrix} \quad (3.43)$$

where every element is obtained following a finite differences scheme. Hence, the first element of the matrix would be calculated as:

$$\frac{\partial L}{\partial W} \approx \frac{L^p - L^*}{(W^{(1)} + \Delta W) - W^{(1)}} \approx \frac{L^p - L^*}{W^p - W^{(1)}} \approx \frac{\Delta L}{\Delta W} \quad (3.44)$$

The superscripts p and $*$ are used to denote if it is a perturbation or target parameter, respectively. The same process is followed in every case of study, which leads to get a better starting point and a faster convergence of the algorithm (if compared to using the identity matrix initialization). Later on, the matrix B is updated with every iteration of the algorithm following expression (3.15).

The code has been implemented in MATLAB®. External calls to a microwave engineering CAD suite that allows full-wave EM simulations, in our case ANSYS DesignerRF, are done by using scripts. After each layout simulation, Matlab recovers the control and makes use of the S-parameters to extract the electrical lumped elements, in a straight-forward way, which will be explained in detail in section 3.3.1.2. The algorithm continues with normal evolution till the norm of the error function (3.11) is smaller than certain

positive value $\eta \ll 1$ or the maximum number of EM-simulations N_{max} (established by the user) is reached. In the first unit cell, the norm of the error function is equal to:

$$\|f^{(j)}\| = \sqrt{(L^{(j)} - L^*)^2 + (C^{(j)} - C^*)^2 + (L_c^{(j)} - L_c^*)^2 + (C_c^{(j)} - C_c^*)^2} \quad (3.45)$$

Afterwards, the stopping criterion was modified, and instead of using the condition $\|f^{(j)}\| < \eta$, it was changed to $\|f^{(j)}\| < \eta_1$ and/or $\|f_{norm}^{(j)}\| < \eta_2$, with η_1 and η_2 being small positive numbers close to zero, $\eta_1 < \eta_2 \ll 1$. With the term f_{norm} we refer to the normalized error function that we have defined for each k component as:

$$f_{norm}^{(j)}[k] = \frac{P(x_f^{(j)}[k]) - x_c^*[k]}{x_c^*[k]} \quad (3.46)$$

The norm of the normalized error function is a more descriptive value, since it evaluates the medium deviation between the extracted parameters and the target x_c^* . Hence, by multiplying $\|f_{norm}^{(j)}\|$ by 100, an approximation of the error in terms of a percentage is obtained. Particularizing expression (3.46) for the first implemented case, it results:

$$\|f_{norm}^{(j)}\| = \sqrt{\left(1 - \frac{L^{(j)}}{L^*}\right)^2 + \left(1 - \frac{C^{(j)}}{C^*}\right)^2 + \left(1 - \frac{L_c^{(j)}}{L_c^*}\right)^2 + \left(1 - \frac{C_c^{(j)}}{C_c^*}\right)^2} \quad (3.47)$$

Therefore, a full-automated tool that makes possible to synthesize these artificial transmission lines is available. As a consequence, the design process is shortened from many hours/days to several minutes/hours, and it does not require special designing skills of the user.

3.3.1.1 Determination of initial layout

The initial layout $x_{em}^{(1)}$ is inferred from x_c^* by means of analytical models (classical expressions for microstrip lines, gaps, CSRRs, OCSRRs) which relate the electrical parameters and the geometrical dimensions (coarse model is physics-based). Those expressions are suitable for modelling isolated components, and they just provide an initial solution (that is still far from the

final solution in many cases). The procedure followed in every cell is explained next.

3.3.1.1.1 TLs based on CSRRs

Depending on the presence or absence of the gap, a different model is used for the host transmission line (microstrip). In the simplest case (i.e. without gap, see Fig. 3.8), the characteristic impedance can be approximated by:

$$Z_c = \sqrt{\frac{L_{pul}}{C_{pul}}} = \sqrt{\frac{L^*}{C^*}} \quad (3.48)$$

where L_{pul} and C_{pul} are the per-unit length inductance and capacitance respectively, and L^* and C^* are the corresponding target values. Once estimated the characteristic impedance of the line, and knowing the characteristics of the substrate (dielectric constant ϵ_r , and the height h), the ratio of the line width (W) over the substrate height (h) can be calculated as:

$$\frac{W}{h} = \begin{cases} \frac{8e^A}{e^{2A} - 2} & \text{for } (W/h) < 2 \\ \frac{2}{\pi} \left[B - 1 - \ln(2B - 1) + \frac{\epsilon_r - 1}{2\epsilon_r} \left\{ \ln(B - 1) + 0.39 - \frac{0.61}{\epsilon_r} \right\} \right] & \text{for } (W/h) > 2 \end{cases} \quad (3.49)$$

where

$$A = \frac{Z_c}{60} \sqrt{\frac{\epsilon_r - 1}{2}} + \frac{\epsilon_r - 1}{\epsilon_r + 1} \cdot \left(0.23 + \frac{0.11}{\epsilon_r} \right) \quad (3.50)$$

$$B = \frac{377\pi}{2Z_c\sqrt{\epsilon_r}} \quad (3.51)$$

and as a result the line width of the initial layout is estimated.

In the case of a host microstrip line with a gap, according to [43] it can be modeled by means of a pi-circuit composed of three capacitors (C_s, C_f, C_L), as depicted in Fig. 3.10.b. Usually, in the parallel capacitance, C_{par} , defined as:

$$C_{par} = C_f + C_L \quad (3.52)$$

the value which dominates is the line capacitance (C_L), and in a first order approximation the fringe capacitance C_f can be neglected, hence $C_{par} \approx C_L$. Consequently, the line width W can be inferred following the previous methodology from the value of the characteristic impedance (3.48) determined by L^* and C_L . The capacitance of the line C_L is function of C_g^* and C^* :

$$C_L \approx C_{par} = \frac{2C_g C}{4C_g + C} \quad (3.53)$$

Once W is estimated, the substrate parameters are known (h and ϵ_r), and the value of C_s is determined as:

$$C_s = \frac{(2C_g)^2}{4C_g + C} \quad (3.54)$$

the gap separation s is calculated using the expressions for a microstrip gap reported in [43].

On the other hand, to estimate the CSRR initial dimensions, a simple optimization process (only two parameters involved) is performed. Since analytical formulas for the electrical parameters (L_c , C_c) of a given topology are known [33], optimal values of the topology are obtained by minimizing the error function from the obtained values (with analytical formulas) and the target ones, f_{error} , defined as follows:

$$f_{error} = \frac{\sqrt{(L_c - L_c^*)^2 + (C_c - C_c^*)^2}}{\sqrt{L_c^{*2} + C_c^{*2}}} \quad (3.55)$$

One of the CSRR geometry parameters is set to a fixed value, usually the width of the slot rings (for example $c = 0.25\text{mm}$), in order to find a deterministic solution for the initial layout and univocally determine the initial values of the CSRR: r_{ext} , c and d .

3.3.1.1.2 TLs based on OCSRrs

To calculate the parameters that define an OCSRr, the same expressions that models CSRR are used, taking into account that the inductance of an OCSRr is four times the one of a CSRR with same dimensions. The values of r_{ext} , c and d , which provide the minimum function error defined by (3.55), determine the initial layout (c is also fixed to certain small value). The parameter “ e ”, which is

the width of the strip present between the inner metallic region of the OCSRR and the access line port, see Fig. 3.14.a, is linked to the circuit parameter L_{sh} . The initial value of e is inferred by the expressions that characterize an electrically small and narrow strip section. The impedance of the strip of length l and width e is given approximately by:

$$Z_c = \frac{L_{sh}}{l \cdot \sqrt{\mu_0 \epsilon_0 \epsilon_{eff}}} \tag{3.56}$$

with μ_0 , ϵ_0 the permeability and permittivity of free space, and ϵ_{eff} the effective permittivity of the microstrip line.

3.3.1.2 Parameter Extraction

Once the EM response of a single unit cell is obtained, the parameters which define the equivalent circuit can be calculated in a straight-forward way using parameter extraction methods. From a practical point of view this is very interesting; since it widely reduces the computational time related the optimization process (there is no need of any additional optimization process). The parameter extraction techniques applied to this kind of artificial transmission lines have been proposed by the research group of Universitat Autònoma de Barcelona [44]. It is performed by imposing several conditions over the EM simulated response (representation of the reflection coefficient S_{11} in the Smith chart and the magnitude/phase of S -parameters). The number of requested conditions needed must be enough to univocally determine all parameters, which is at least equal to the number of the circuit parameters considered. The process followed for each unit cell is explained next, i.e. in subsection 3.3.1.2.1 for the host line loaded with CSRRs (with and without gap), and in 3.3.1.2.2 for TLs based on OCSRRs.

3.3.1.2.1 TLs based on CSRRs

The methodology to obtain the circuit parameters of these cells was proposed in 2006 [34], being the losses neglected in our case. Two frequencies can be clearly identified: the frequency ω_z which nulls the shunt impedance (3.32); and the frequency ω_o that nulls the shunt admittance (resonance frequency of the CSRR):

$$\omega_0 = 2\pi f_0 = \frac{1}{\sqrt{L_c C_c}} \tag{3.57}$$

To determine f_0 , the reflection coefficient (S_{11}) is represented in Smith Chart. It corresponds to the frequency where S_{11} intercepts with the normalized unit resistance circle, where the shunt path to ground is opened, and the input impedance seen from the ports is as result the series impedance, see Fig. 3.17 or Fig. 3.18 for clearance. In the case of the first unit cell, the value of L is obtained in a straightforward way as:

$$Z_{in}(f_0) = Z_0 + j2\pi f_0 L \tag{3.58}$$

where Z_0 is the reference impedance of the ports.

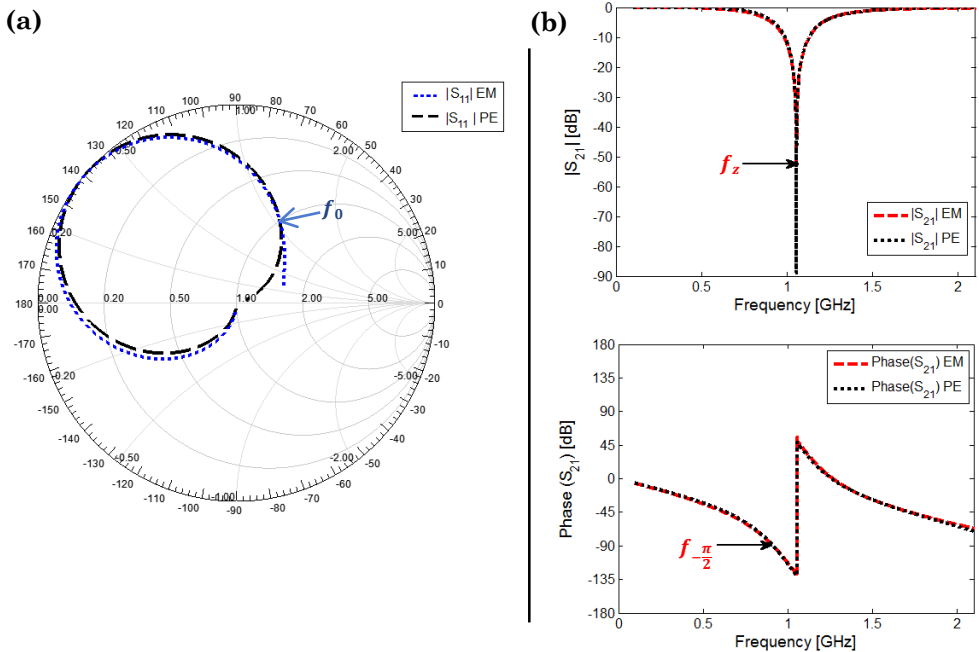


Fig. 3.17. - Comparison of electromagnetic and circuit simulations (PE) for the cell of negative permittivity. (a) S_{11} in Smith Chart (b) Frequency response of transmission coefficient S_{21} (magnitude and phase).

To univocally determine the other three parameters (shunt branch), that characterize the first unit cell; we need to force an additional condition:

$$Z_{se_cell1}(j\omega_{-\pi/2}) = -Z_{par_cell1}(j\omega_{-\pi/2}) \quad (3.59)$$

where Z_{se_cell1} and Z_{par_cell1} are the series and shunt impedances of the T-circuit model, and $\omega_{-\pi/2}$ is the angular frequency where the phase of the transmission coefficient S_{21} provides a value of $-\pi/2$ radians (-90 degrees). By solving the system of equations (3.32), (3.57) and (3.59), all the parameters of the circuit model of the first cell are finally determined.

An example for this cell has been simulated with ANSYS DesignerRF. The selected substrate is the Rogers RO3010 with a thickness $h=1.27\text{mm}$, a dielectric constant $\epsilon_r=10.2$ and a loss tangent $\tan \delta=0.0023$. Dielectric losses were not taken into account for the EM-simulation, and metal parts were considered as a perfect conductor (since we did not include a resistance in the equivalent circuit model). Geometrical dimensions of the unit cell are $x_{em} = [r_{ext}, c, d, W] = [5.75\text{mm}, 0.25\text{mm}, 0.4\text{mm}, \text{and } 4.5\text{mm}]$ The corresponding circuit parameters, determined using the parameter extraction method just outlined, were $x_c = [L, C, L_c, C_c] = [5.605 \text{ nH}, 4.182 \text{ pF}, 2.747 \text{ nH}, 4.088 \text{ pF}]$. In Fig. 3.17, both simulations, electrical and electromagnetic, are depicted, and the significant frequencies $f_0, f_{-\pi/2}, f_z$ involved in the PE process are also indicated. The agreement between circuitual (dash traces in black) and EM (blue traces) at the region of interest for the transmission coefficient is very good.

The equation (3.59) is not applied in the second case of study (CRLH cell), but a similar condition is imposed instead:

$$Z_{se_cell2}(j\omega_{\pi/2}) = -Z_{par_cell2}(j\omega_{\pi/2}) \quad (3.60)$$

with $\omega_{\pi/2}$ the angular frequency where the phase of S_{21} is $\frac{\pi}{2}$ radians. An extra equation is needed in order to obtain all the circuitual values, since this circuit model, see Fig. 3.14.c, has one parameter more than in the other case (C_g). The resonance frequency of the series branch f_s :

$$\omega_s = 2\pi f_s = \frac{1}{\sqrt{LC_g}} \quad (3.61)$$

can be calculated also by means of the representation of S_{11} in the Smith Chart which coincides with the value where S_{11} trace intercepts with the normalized

unit conductance circle (since the series impedance is rendered a short-circuit). In Fig. 3.18, an application example to show the good performance of the method in the working region for the CRLH unit cell is provided. The chosen substrate is the same one used for the other case, i.e. the Rogers R03010 ($\epsilon_r = 10.2$, $h = 1.27\text{mm}$).

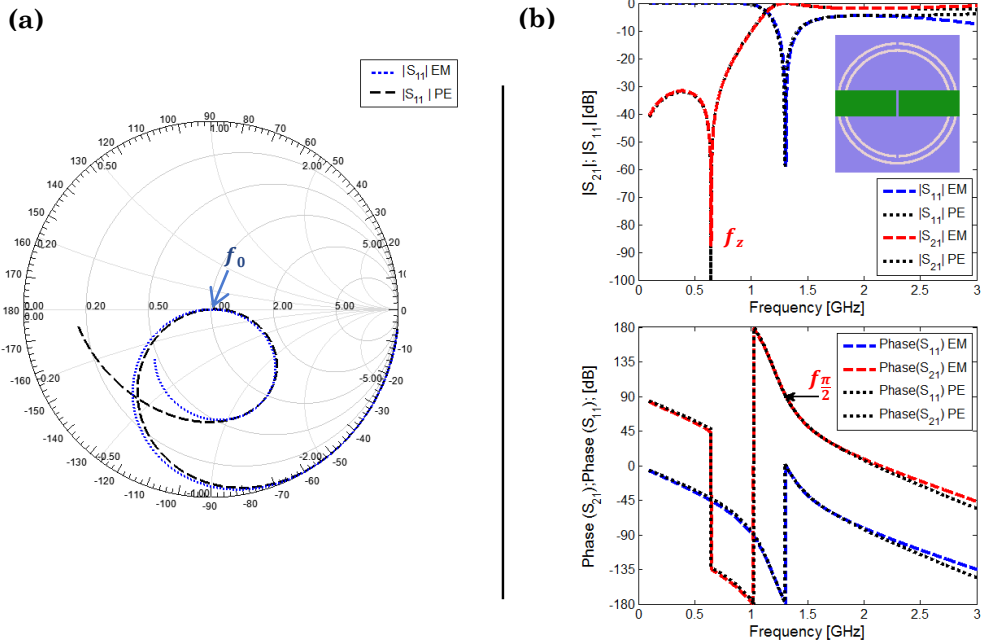


Fig. 3.18. - Comparison of EM simulation $x_{em}=[r_{ext}, c, d, W, s]= [5\text{mm}, 0.25\text{mm}, 0.3\text{mm}, 3.5\text{mm}, 0.3\text{mm}]$ and circuital simulation $x_c=[L, C, L_c, C_c, C_g] = [3.882\text{nH}, 18.647\text{pF}, 2.751\text{nH}, 3.282 \text{ pF}, 0.893 \text{ pF}]$ obtained by PE for a CRLH unit cell. (a) S_{11} in Smith Chart (b) Frequency response of S-parameters (magnitude and phase).

3.3.1.2.2 TLs based on OCSRrs

Concerning to the parameter extraction for the case of OCSRr in microstrip, three different conditions are considered. The position of the transmission zero frequency f_z given by expression (3.41), the position of the reflection zero frequency (or intrinsic resonance of the OCSRr) given by (3.42), and the last condition is given by the value of the susceptance slope parameter (b) at certain frequency of the working frequency range, as for example at the frequency f_z . All the circuit parameters can be easily inferred from the electromagnetic simulation and solving afterwards the system of equations similarly to previous structures.

An example showing the validity of the model and the PE extraction strategy in the working region is depicted in Fig. 3.19, where the traces in black, as in previous cases, stand for the circuitual simulation of the parameters determined by PE (corresponding to those of the circuit model in Fig. 3.14.b). The substrate used is Rogers R03010, ($\epsilon_r = 10.2$; $h = 0.254\text{mm}$).

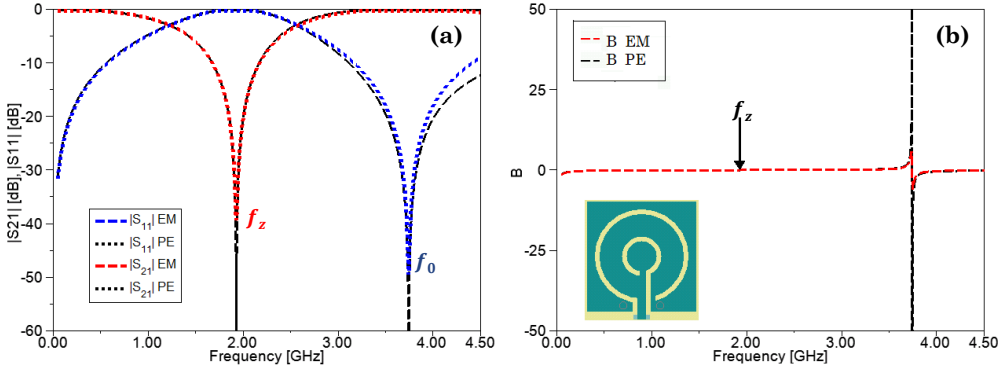


Fig. 3.19. - Comparison of EM simulation $x_{em} = [r_{ext}, d, e] = [2.5\text{mm}, 1.2 \text{ mm}, 0.5\text{mm}]$, with $c=0.25\text{mm}$ and circuitual simulation $x_c = [L_p, C_p, L_{sh}] = [1.612\text{nH}, 4.299\text{pF}, 0.584\text{nH}]$ obtained by PE for a shunt OCSRR in microstrip: (a) S-parameters (in magnitude); (b) susceptance (B). The susceptance slope parameter b is calculated according to expression (4.15).

3.3.1.3 Automated Synthesis

In order to demonstrate the capabilities of the proposed synthesis technique, different examples (one for each cell of study) are presented. The EM responses were simulated in ANSYS DesignerRF, even though other commercial software tool –i.e. Agilent Momentum- can be used obtaining satisfactory results as well [45]. The used substrate was again the commercial Rogers RO3010 of dielectric constant $\epsilon_r=10.2$. In case of TLs based on CSRRs the thickness is $h=1.27\text{mm}$ and for the case of OCSRRs $h = 0.254 \text{ mm}$.

3.3.1.3.1 TLs based on CSRRs

The target circuit parameters are given by the vector $x_c^* = [L^*, C^*, L_c^*, C_c^*]$ (see values in Table 3.1), which are the ones given for a topology extracted from ref. [34], where parameter extraction was introduced for this kind of cells.

The initial layout of the structure $x_{em}^{(1)}$ has been inferred from the target parameters following the methodology presented in subsection 3.3.1.1.1. The corresponding frequency response is shifted to upper frequencies, as illustrated in Fig. 3.21.

Table 3. 1. - COARSE PARAMETERS FOR CSRR UNIT CELL ($\epsilon < 0$)

	L [nH]	C [pF]	L_c [nH]	C_c [pF]	$\ f\ $
Target (x_c^*)	5.080	4.430	2.980	4.060	
Initial	8.201	2.793	2.672	4.109	3.5377
Final	5.076	4.420	2.986	4.063	0.0124

The final solution is achieved after 17 iterations of the algorithm, when the norm is smaller than 0.0150. Notice that the resulting circuit parameters (Table 3.1) are very close to the target parameters, as expected. Anyway, after the 10th iteration, the error is already quite small, as shows Fig. 3.20. The CPU effort to obtain a synthesis of this type of cell is around 30 minutes (using a standard computer of 3GB of RAM, 2.86GHz clock processor).

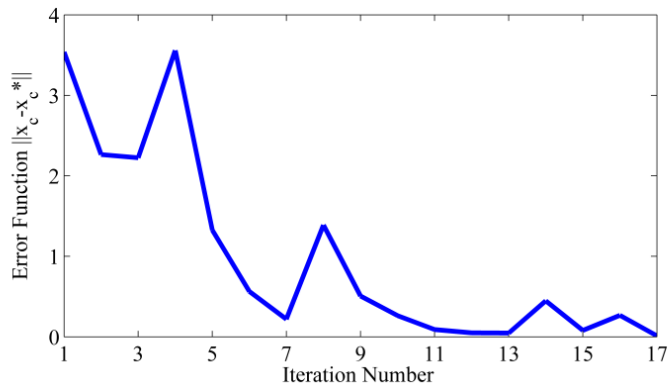


Fig. 3.20. - Evolution of the error function in norm ($\|f\|$) versus iteration number.

In Fig. 3.21, the EM full-wave simulations for the initial and final layouts are depicted, and also compared with the circuit target response. It can be seen a very good agreement between final and target response in the working frequency range shown. Far from this range, it can be observed some discrepancies, particularly at higher frequencies where coarse model is not accurate any more, since CSRR cannot be considered electrically small.

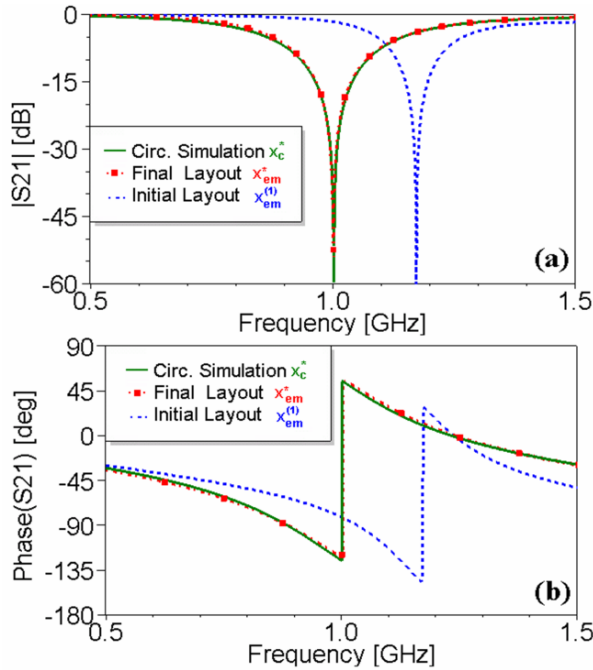


Fig. 3.21. - Frequency response of the transmission coefficient S_{21} in magnitude (a) and phase (b).

The initial and final dimensions of the layout are summarized in Table 3.2. Final solution dimensions are close to the ones published in [34] obtained manually. Differences can be attributed to geometrical parameter sensitivity, and also to the fact that more than one layout can fulfill specs, as we already stated in [46].

Table 3. 2. - FINE PARAMETERS FOR CSRR UNIT CELL ($\epsilon < 0$)

	r_{ext} [mm]	c [mm]	d [mm]	W [mm]
Initial ($x_{em}^{(1)}$)	6.39	0.25	0.95	2.43
Final	5.68	0.36	0.33	4.97
Topology article [34]	5.65	0.33	0.19	3.85

For the second case of study, the target parameters are those provided in Table 3.3. The initial layout is inferred from target parameters by means of analytical formulas, as it is explained in subsection 3.3.1.1.1.

Table 3. 3. - COARSE PARAMETERS FOR CSRR UNIT CELL (CRLH) AND ERRORS

	L [nH]	C [pF]	L_c [nH]	C_c [pF]	C_g [pF]	$\ f\ $	$\ f_{norm}\ $
Target (x_c^*)	3.850	21.530	2.830	3.380	0.920		
Initial	5.375	9.731	2.565	3.166	0.454	11.9115	0.8525
Final	3.856	21.453	2.841	3.393	0.922	0.0079	0.0069

The final layout is automatically obtained using ASM with a variable shrinking factor (adjusted to the most critical dimension), and the stopping criterion used in this case is $\|f_{norm}\| < 0.01$ and $\|f\| < 0.1$. As it was briefly underlined in section 3.3.1, the normalized error is considered as a stopping criterion, since all the circuit parameters are not in the same order of magnitude (C^* is bigger). The norm of the normalized error function is defined as follows:

$$\|f_{norm}^{(j)}\| = \sqrt{\left(1 - \frac{L^{(j)}}{L^*}\right)^2 + \left(1 - \frac{C^{(j)}}{C^*}\right)^2 + \left(1 - \frac{L_c^{(j)}}{L_c^*}\right)^2 + \left(1 - \frac{C_c^{(j)}}{C_c^*}\right)^2 + \left(1 - \frac{C_g^{(j)}}{C_g^*}\right)^2} \quad (3.62)$$

where the inductive and capacitive values are expressed in nH and pF, respectively. The final layout, summarized in Table 3.4, is achieved after just seven iterations of the algorithm, which means 12 EM simulations (5 are for the initialization of B matrix). For this example, the CPU effort was approximately 31 minutes (using now a computer of 8GB of RAM, Intel Core i5, 760@2.80GHz with 4 cores). Evolution of the norm of the error versus iteration number is depicted in Fig. 3.22.

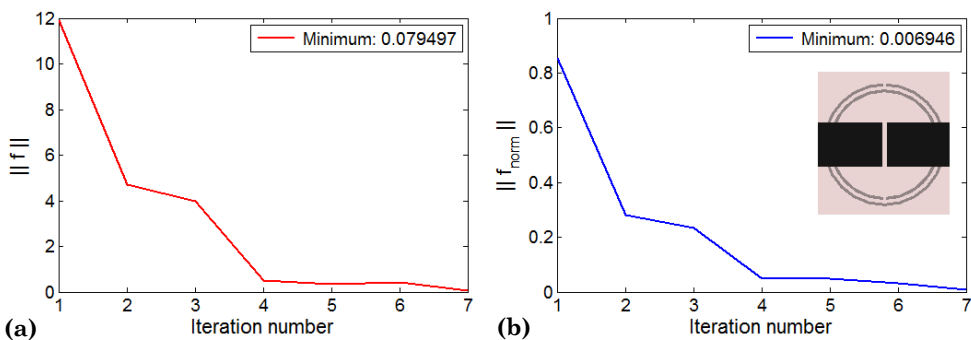


Fig. 3.22. - Evolution of the error function with the iteration number: (a) $\|f\|$; (b) $\|f_{norm}\|$.

There is a very good agreement between the EM simulation of the final layout and the target response, as Fig. 3.23 illustrates. In dashed light lines, the

traces corresponding to the EM simulation of the initial layout, which are still far away from the target response, are also depicted.

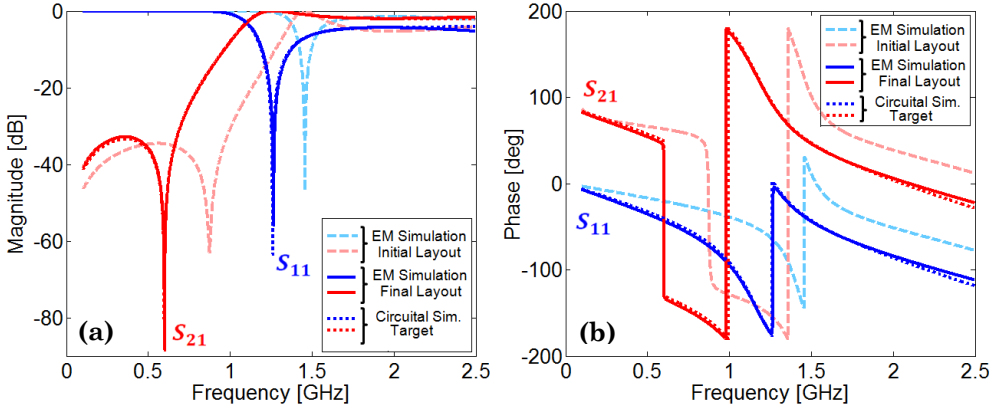


Fig. 3. 23. - Frequency response of the transmission S_{21} and reflection S_{11} coefficients in magnitude (a) and phase (b).

Table 3. 4. - FINE PARAMETERS FOR CSRR UNIT CELL (CRLH)

	r_{ext} [mm]	W [mm]	s [mm]	c [mm]	d [mm]
Initial ($x_{em}^{(1)}$)	4.91	1.20	0.15	0.20	0.41
Final	5.07	3.66	0.37	0.23	0.28

3.3.1.3.2 Tls based on OCSRRs

We have considered an example of an OCSRR with target values given by $L_p^* = 3.8$ nH, $C_p^* = 4.10$ pF and $L_{sh}^* = 0.5$ nH. The final layout is obtained when the normalized error function, given by:

$$\|f_{norm}^{(j)}\| = \sqrt{\left(1 - \frac{L_p^{(j)}}{L_p^*}\right)^2 + \left(1 - \frac{C_p^{(j)}}{C_p^*}\right)^2 + \left(1 - \frac{L_{sh}^{(j)}}{L_{sh}^*}\right)^2} \quad (3.63)$$

is smaller than 1%. For the present example, this means 9 iterations of the ASM algorithm (12 EM simulations), and a computational time of approximately 50 minutes (using a computer of 8GB of RAM, Intel Core i5, 760@2.80GHz with 4 cores). The evolution of the error norm along the execution of the algorithm is depicted in Fig. 3.24.

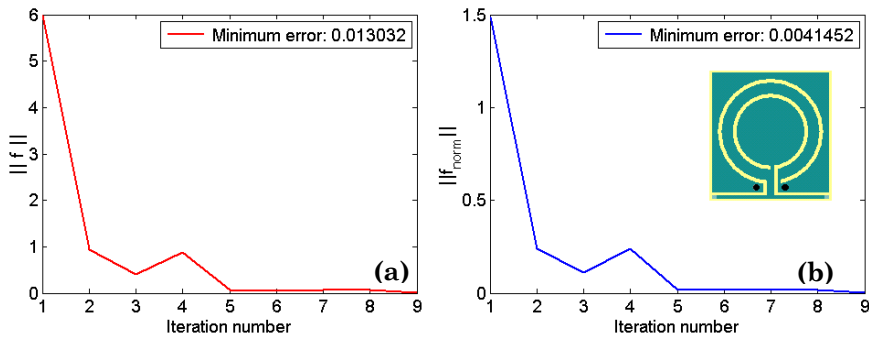


Fig. 3. 24. - Evolution of the error function (norm) with the iteration no.: a) $\|f\|$; (b) $\|f_{norm}\|$.

In Table 3.5, the values of the coarse model parameters for the target, initial and final layouts, together with the corresponding errors, are summarized.

Table 3. 5. - COARSE PARAMETERS FOR OCSR UNIT CELL AND ERRORS

	L_p [nH]	C_p [pF]	L_{sh} [nH]	$\ f\ $	$\ f_{norm}\ $
Target (x_c^*)	3.80	4.10	0.500		
Initial ($x_c^{(1)}$)	4.026	10.081	0.641	5.9868	1.4869
Final	3.789	4.093	0.501	0.0130	0.0041

The electromagnetic simulations of the initial and final layouts are depicted in Fig. 3.25, with their dimensions summarized in Table 3.6. As it can be seen, the agreement between the circuit (target) and optimized (final layout) EM simulation is excellent (almost undistinguishable) in the shown frequency range, except at higher frequencies.

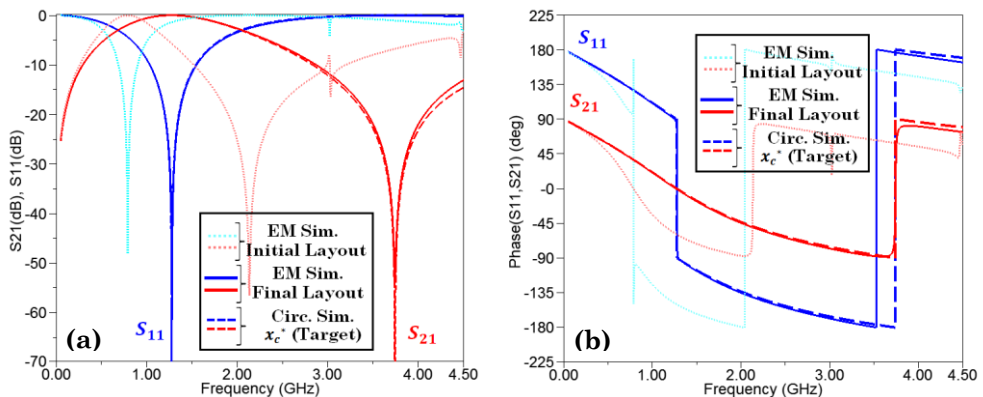


Fig. 3.25. - Comparison of EM simulation of initial layout (dot line in light colors) and final layout (solid line) and circuit simulation (dashed line) of target parameters $x_c^* = [3.8\text{nH}, 4.1\text{pF}, 0.5\text{nH}]$: S-parameters in magnitude (a) and phase (b).

Table 3. 6. - FINE PARAMETERS FOR OCSRR UNIT CELL

	r_{ext} [mm]	c [mm] (fixed)	d [mm]	e [mm]
Initial ($x_{em}^{(1)}$)	3.5	0.25	0.74	0.46
Final ($x_{em}^{(9)}$)	2.25	0.25	0.35	0.52

3.3.2 ASM + Line Search

In order to increase the robustness and/or to accelerate the convergence rate of the algorithm, some other enhancements have been introduced to the initial implemented solution of ASM (that was illustrated in Fig. 3.15). For instance, to avoid abrupt variations in the norm of the error function $\|f\|$ (that frequently appear in the algorithm execution), line search (LS) is added to the ASM update stage, as observed in Fig. 3.26. This leads to a smoother decreasing behaviour of $\|f\|$ until convergence of the algorithm is achieved [47].

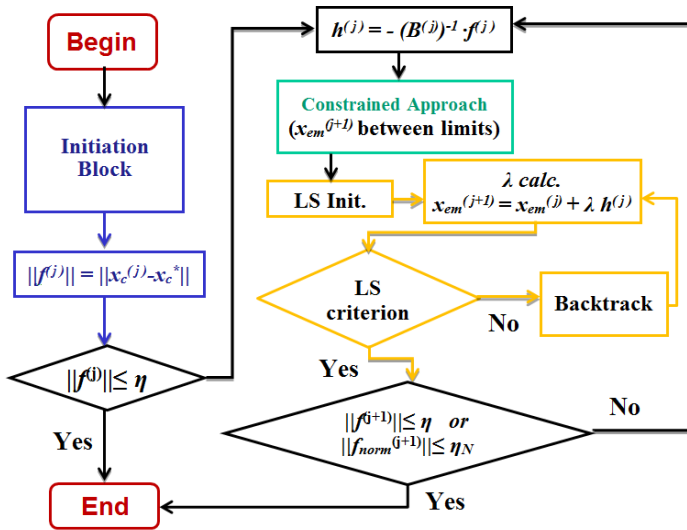


Fig. 3.26. - Flow-diagram of the ASM algorithm with Line Search (highlighted in yellow).

To some extent, line search can be considered to some extent dual to trust region methods. In trust region methods, a step size (equal to the size of the trust region) is chosen first, and then a step direction is selected, whereas for line search methods a step direction is firstly chosen, and then a step size is found. The direction of ASM algorithm is Newton-based, where the step $h^{(j)}$, as it was previously defined in (3.12)-(3.13), is shortened using line search by means of a factor λ :

$$x_{em}^{(j+1)} = x_{em}^{(j)} + \lambda \cdot h^{(j)}, \quad 0 < \lambda \leq 1 \tag{3.64}$$

when the error function is not sufficiently decreased with respect to the previous iteration. Hence, if the next solution $x_{em}^{(j+1)}$ does not meet the following criterion:

$$f(x_{em}^{(j+1)}) \leq f(x_{em}^{(j)}) + \kappa \cdot \nabla f(x_{em}^{(j)}) \cdot \lambda \cdot h^{(j)} \quad \text{with } \kappa = 10^{-4} \tag{3.65}$$

several backtracks (along the same quasi-Newton direction) are applied till the error function satisfies (3.65) or the layout obtained is equal to the one of previous iteration ($x_{em}^{(j+1)} \approx x_{em}^{(j)}$).

First λ is equal to the unit, i.e. the normal evolution of the ASM algorithm. Afterwards, if (3.65) is not satisfied the error function f will be modeled by a quadratic polynomial function (first backtrack), or by a cubic polynomial approach (if more backtracks are needed) to obtain a new value for λ . In both approximations, λ must lie between one tenth and a half of the calculated value of λ in the previous iteration. More details about the implementation of LS algorithm can be found in [4].

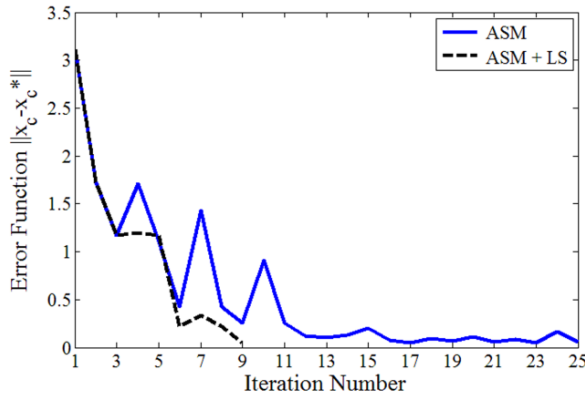


Fig. 3. 27. - Evolution of $\|f\|$ versus iteration number, using ASM with $\delta = 0.4$ (solid blue line) and ASM+LS (dashed black line).

One example where LS results in a clear improvement is shown in Fig. 3.27. The synthesized cell corresponds to a unit cell of first type, with a target response given by $x_c^* = [L^*, C^*, L_c^*, C_c^*] = [4.860 \text{ nH}, 1.640 \text{ pF}, 2.180 \text{ nH}, 2.890 \text{ pF}]$. The initial and final layouts are summarized in Table 3.7. Note that the final layouts are not exactly the same ones for the original ASM and for the ASM+LS, but they are very similar. The reason is that there is not a single/unique

solution, different layouts can satisfy the stopping criteria, in this particular case $\|f\| \leq 0.05$. The number of EM simulations needed to find the final synthesis is decreased from 29 to 18 when LS is used, being the computational time effort significantly reduced as a result. For the constrained approach of ASM, a shrinking factor of $\delta=0.4$ has been used.

Table 3. 7. - FINE PARAMETERS FOR CSRR UNIT CELL AND ERROR

	r_{ext} [mm]	W [mm]	c [mm]	d [mm]	$\ f\ $
Initial	4.83	0.99	0.25	0.93	3.105
Final ASM ($\delta=0.4$)	4.02	1.95	0.42	0.15	0.048
Final ASM+LS ($\delta=0.4$)	4.03	1.99	0.43	0.16	0.050

However, for those cases where ASM does not have an important variation, or the initial layout provides a big error, LS can derive in slow convergence. To avoid this issue, a modified criterion in the application of LS was proposed, that is summarized next for each kind of considered cell:

- Case 1 (Negative permittivity cell): only one backtrack is allowed till $\|f^{(j+1)}\| < 0.5$ in order to avoid initial slow convergence.
- Case 2 (CRLH): Backtrack is not performed if the normalized error function $\|f_{norm}^{(j+1)}\|$ defined in (3.45) has decreased, and only one backtrack is allowed till $\|f^{(j+1)}\| < 2.5$ in order to avoid initial slow convergence.

Using the same target response of the last example and applying ASM with different shrinking factor ($\delta=0.3$), it can be observed that ASM works much slower. Now it converges at 44th iteration (see Fig. 3.28), while previously it reached convergence at 25th iteration (see Fig. 3.27). The algorithm was forced to continue till 70th iteration, thus clearly appreciating the softer evolution of the algorithm when standard LS is applied. It can be concluded that standard LS converges very slow, whereas the convergence of the modified LS algorithm is speeded up, having already converged at iteration 13th. All solutions are collected in Table 3.8, with the corresponding final error values.

Table 3. 8. - FINE PARAMETERS FOR CSRR UNIT CELL AND ERROR

	r_{ext} [mm]	W [mm]	c [mm]	d [mm]	$\ f\ $
Initial	4.83	0.99	0.25	0.93	3.105
Final ASM ($\delta=0.3$)	4.02	1.93	0.42	0.18	0.0104
Final ASM+LS ($\delta=0.3$)	4.03	1.95	0.43	0.19	0.0137
Final ASM + LS mod ($\delta=0.3$)	4.02	1.93	0.40	0.18	0.104

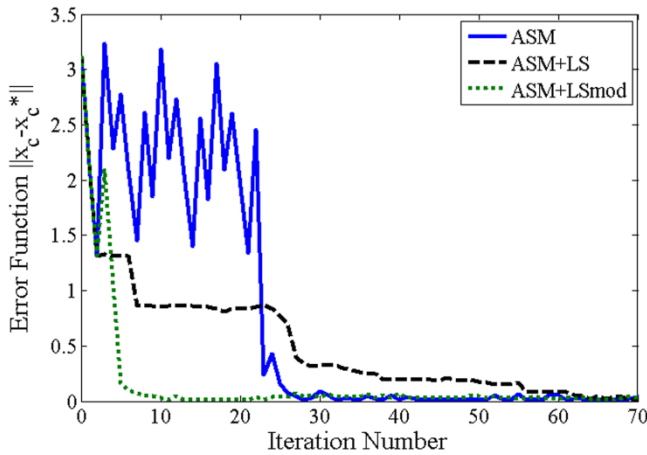


Fig. 3.28. - Evolution of $\|f\|$ versus iteration number, using ASM (solid blue line) and ASM+LS (dashed black line), and ASM+LS modified (dotted green line).

3.3.3 Identification of a convergence region

Although the techniques just explained before were able to successfully automate the transmission line synthesis, they were not able to guarantee if a given optimal coarse model solution could be physically implemented. In order to have a powerful practical synthesis tool, the previous issue is considered critical. To overcome this limitation, a previous stage which basically consists in the identification of a convergence region (CR) is introduced. If the target solution is inside the estimated convergence region, it means that there is an implementable solution. Hence, a more robust algorithm will be available.

3.3.3.1 TLs based on CSRRs

At this point, a different nomenclature is introduced to distinguish between the two cases of study involving CSRRs (as done in [48]). So from now and on, microstrip lines only loaded with CSRRs will be called as CSRR-loaded metalines, and those lines loaded with both CSRRs and series gaps will be named as CSRR-gap-loaded metalines.

Three different modules can be clearly distinguished in the new proposed algorithm, as indicated in Fig. 3.29:

- ASM Pre-optimization → This module is used to determine the convergence region. It is a simplified ASM scheme, where the target

parameters are reduced to those that mainly characterize the host transmission line, i.e. microstrip $x_{cr}^* = [L^*, C^*]$ or microstrip with series gap $x_{cr}^* = [L^*, C^*, C_g^*]$.

- Interpolation → Information obtained from the determination of the convergence region is used to establish a better initial layout for the ASM full-optimization stage. As a consequence, the convergence of the core algorithm (ASM full-optimization) is sped up. In some cases, the new layout is so close to the target, that no further ASM-based optimization is even needed.
- ASM-Full optimization → It is basically the previous reported algorithm of section 3.3.1, but with an improved initial seed (much closer to the target). Note that the vector of the geometrical dimensions x_f now uses the length of the line, instead of r_{ext} but those conditions are equivalent since are scaled dimensions ($r_{ext} = l/2$).

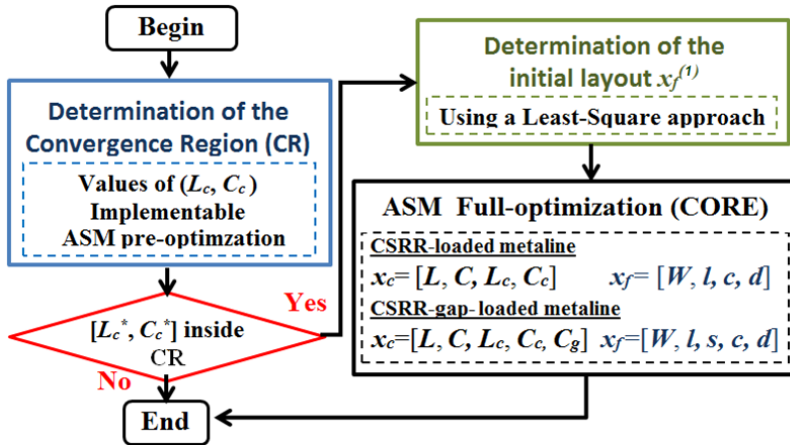


Fig. 3.29. - Schematic of the new proposed two-step ASM algorithm.

The implementable layouts of CSRR based lines are limited to certain combinations of the element values of the circuit models (L_c, C_c). Despite some efforts to establish those limits had been realized by means of parametric analysis [37], there is not a systematic procedure to determine them. We have proposed to estimate a convergence region with a simplified ASM scheme that for the CSRR-loaded metalines case is schematically illustrated in Fig. 3.30, and it was published for the first time in [49].

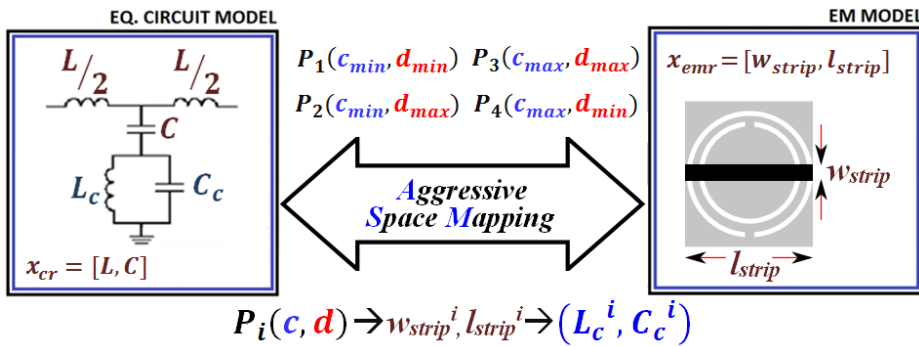


Fig. 3. 30. - ASM Pre-optimization diagram used to determine the convergence region for a CSRR-loaded metaline.

Having in mind the circuit model of the CSRR-loaded metaline, depicted in Fig. 3.30, L and C are physically implementable as long as these values are not too extreme, and a microstrip line with reasonable width and length results. Hence, given a pair of realizable values for L^* and C^* , a region which determines the implementable circuit values that model the CSRR is calculated by means of ASM. Since the dimensions of the CSRR are the limiting factor, four different scenarios are considered according to the range of acceptable values for the width slot (c_{min} - c_{max}) and for separation between the slots (d_{min} - d_{max}):

- $P_1 \rightarrow c = c_{min}; d = d_{min}$ (P_{c15d15} in Fig. 3.31.a)
- $P_2 \rightarrow c = c_{min}; d = d_{max}$ (P_{c15d40} in Fig. 3.31.a)
- $P_3 \rightarrow c = c_{max}; d = d_{max}$ (P_{c40d40} in Fig. 3.31.a)
- $P_4 \rightarrow c = c_{max}; d = d_{min}$ (P_{c40d15} in Fig. 3.31.a)

The higher number of points to determine the region, the higher accuracy for the convergence region will be. Nevertheless, in the structure under study, four points are considered enough to obtain a good estimation of such region, although more points are needed to be taken into account for CSRR-gap-loaded metalines, as it will be explained later. For each combination of the limiting values of c and d , $P_i(c, d)$, a synthesis solution (w_{strip}^i, l_{strip}^i) providing the requested L^* and C^* values is found. After performing these simple synthesis problems (involving only 2 optimization variables to recover the optimal coarse solution), a set of values for the elements L_c and C_c of the equivalent circuit model are found. The graphical representation of this set of values (L_c, C_c) gives the desired convergence region corresponding to the target parameters L^* and C^* , as it can be seen in Fig. 3.31.a for a particular example. In Fig. 3.31.b, different regions calculated for the same target response, but considering different

constraints, are depicted, thus showing that the shape of such regions is kept similar but with different sizes.

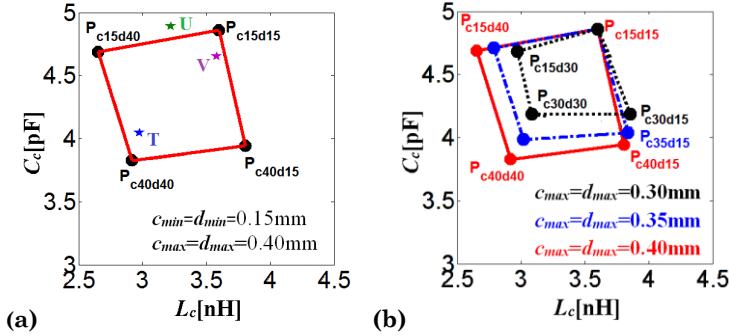


Fig. 3.31. - (a) Convergence region for $x_{cr}^* = [L^*, C^*] = [5.08 \text{ nH}, 4.43 \text{ pF}]$, defined by 4 vertices. (b) Regions defined with different constraints for the same x_{cr}^* .

It is worthy of noticing that, that with the aim of accelerating the computation of the cited vertexes, the solution layout calculated for a point is used as the starting layout to solve the next one (i.e. line dimensions: w_{strip}, l_{strip}). Additionally the matrix B is initialized with the one obtained after the execution of the previous vertex (that reduces the initializing cost of the algorithm to 1 EM simulation, instead of the 3 EM simulations needed for the first vertex, where the finite difference scheme of section 3.3.1 is followed). Table 3.9 includes the effort requested (in number of iterations or EM simulations) to determine the convergence region for a case with lower constrains fixed to the fabrication limit ($c_{min} = d_{min} = 0.15\text{mm}$) and the upper ones chosen as $c_{max} = d_{max} = 0.35\text{mm}$, which is depicted in Fig. 3.31.b with blue dash line.

Table 3.9. - CONVERGENCE REGION VERTICES AND REQUIRED ASM ITERATIONS

Limiting Layouts	L_c [nH]	C_c [pF]	Iter. No
$P_1 \rightarrow c[\text{mm}]=0.15, d[\text{mm}]=0.15$	3.651	4.384	7 (9 EM Sim.)
$P_2 \rightarrow c[\text{mm}]=0.15, d[\text{mm}]=0.35$	2.789	4.688	3 (3 EM Sim)
$P_3 \rightarrow c[\text{mm}]=0.35, d[\text{mm}]=0.35$	2.958	4.012	5 (5 EM Sim)
$P_4 \rightarrow c[\text{mm}]=0.35, d[\text{mm}]=0.15$	3.891	4.004	4 (4 EM Sim)

Once the convergence region is determined, obtaining the initial layout is almost straightforward. Since every vertex of the region is linked to a known physical solution, a two dimensional interpolation is applied. Each geometric variable (i.e. W, l, c and d), referred generically as z , is function of L_c and C_c . A

first order polynomial function approximation can model this behavior as follows:

$$z = f(L_c, C_c) = a_0 + a_1 L_c + a_2 C_c + a_3 L_c C_c \quad (3.66)$$

In order to find the coefficients of the previous polynomials, a system of equations which minimizes the least-squares error must be solved:

$$\frac{\partial f_{error}}{\partial a_i} = 0 \quad (3.67)$$

The error function is given by:

$$f_{error} = \sum_{j=1}^{N_V} \left(z_j - f(L_{c_j}, C_{c_j}) \right)^2 \quad (3.68)$$

where the subscript j denotes the vertex number, being z_j the corresponding value of z in that vertex. Therefore, the resulting system of equations for the case of study is:

$$\begin{pmatrix} 4 & \sum_{j=1}^4 L_{c_j} & \sum_{j=1}^4 C_{c_j} & \sum_{j=1}^4 L_{c_j} C_{c_j} \\ \sum_{j=1}^4 L_{c_j} & \sum_{j=1}^4 L_{c_j}^2 & \sum_{j=1}^4 L_{c_j} C_{c_j} & \sum_{j=1}^4 L_{c_j}^2 C_{c_j} \\ \sum_{j=1}^4 C_{c_j} & \sum_{j=1}^4 L_{c_j} C_{c_j} & \sum_{j=1}^4 C_{c_j}^2 & \sum_{j=1}^4 C_{c_j}^2 L_{c_j} \\ \sum_{j=1}^4 L_{c_j} C_{c_j} & \sum_{j=1}^4 L_{c_j}^2 C_{c_j} & \sum_{j=1}^4 C_{c_j}^2 L_{c_j} & \sum_{j=1}^4 C_{c_j}^2 L_{c_j}^2 \end{pmatrix} \cdot \begin{pmatrix} a_0 \\ a_1 \\ a_2 \\ a_3 \end{pmatrix} = \begin{pmatrix} \sum_{j=1}^4 z_j \\ \sum_{j=1}^4 z_j L_{c_j} \\ \sum_{j=1}^4 z_j C_{c_j} \\ \sum_{j=1}^4 z_j L_{c_j} C_{c_j} \end{pmatrix} \quad (3.69)$$

The next step is to apply the full-optimization algorithm. Thanks to the new initial seed (which is already quite close to the target), the final synthesis is obtained very fast. Actually in some cases the initial layout can be considered a solution if the error is sufficiently small. In order to illustrate the behavior of the proposed algorithm, three application examples are reported next in Table 3.10. Notice that all belong to the same convergence region, since they have the same values for L^* and C^* .

Table 3. 10. - OPTIMAL COARSE SOLUTIONS

	L [nH]	C [pF]	L_c [nH]	C_c [pF]
T	5.080	4.430	2.980	4.060
U	5.080	4.430	3.222	4.891
V	5.080	4.430	3.581	4.654

The first stage consists in determining whether the considered examples are physically realizable or not. Having a look to Fig. 3.31.a, it is observed that targets T and V are located inside the convergence area, but U is not. Since U is placed close to the convergence region, a possible solution for this case might have any of the dimensions out of the established limits (presumably c , due to the vicinity of U to the border line where c is equal to the fabrication limit).

The initial layouts for the different targets are summarized in Table 3.11. As it can be seen, the initial layouts obtained with the procedure based on analytical formulas present errors much higher than the ones obtained with the convergence region estimation. In the interpolated approach, normalized errors are always under 10%. In fact, in some cases like the first one (target T), the initial layout can already be considered a solution (normalized error is less than 2%, i.e. multiplying $\|f_{norm}\|$ by 100).

Table 3. 11. - FINE PARAMETERS FOR THE INITIAL LAYOUT AND ERRORS

	l [mm]	W [mm]	c [mm]	d [mm]	$\ f\ $	$\ f_{norm}\ $
T (analytical seed)	12.78	2.43	0.25	0.95	3.5377	0.7244
T (new seed: Inter.)	11.43	5.04	0.34	0.37	0.0779	0.0198
U (analytical seed)	15.38	2.43	0.25	1.37	5.4737	1.0858
U (new seed: Inter.)	11.81	4.49	0.12	0.24	0.2842	0.0800
V (analytical seed)	14.16	2.43	0.25	0.78	4.1730	0.8352
V (new seed: Inter.)	11.74	4.54	0.20	0.17	0.1229	0.0283

After applying the ASM-Full optimization algorithm (without Line Search in both cases), the evolution of the error for the considered cases is depicted in Fig. 3.32, being the corresponding layouts, error values and requested number of iterations collected in Table 3.12. Notice that the fact of using different initial layouts can lead to obtain different solutions, even though the variation of the dimensions is not significant (when convergence is achieved). The final layout obtained for the second example (U) is slightly out of the lower boundary ($c = 0.14\text{mm}$), as it was expected since target U was placed out of the convergence

Chapter 3. Optimization

region (the lower constraints of the algorithm were relaxed in order to verify this issue).

Table 3. 12. - FINE PARAMETERS FOR THE FINAL LAYOUT, ITERATION NUMBER AND ERRORS

	l [mm]	W [mm]	c [mm]	d [mm]	Iter. No.	$\ f\ $	$\ f_{norm}\ $
T (analytical seed)	11.34	4.93	0.33	0.34	17	0.0124	0.0032
T (new seed)	11.32	4.89	0.34	0.33	3	0.0176	0.0054
U (analytical seed)	11.84	4.46	0.14	0.21	26	0.0326	0.0065
U (new seed.)	11.82	4.48	0.14	0.21	15	0.0189	0.0040
V (analytical seed)	12.12	4.07	0.16	0.15	30	0.5649	0.1336
V (new seed)	11.76	4.49	0.17	0.17	3	0.0344	0.0089

It can be observed in Fig. 3.32 that using a better starting point accelerates the convergence rate. Furthermore, there are cases, as the one illustrated by third example (V), where the old initial layout does not converge to a final solution, whereas the new approach just converges in three iterations of the algorithm. In the second example (point U), the convergence is not so fast. This can be attributed to the fact that solutions is very close to the constraints, which typically slow down the optimization process (some instabilities can appear). Nevertheless, convergence is still achieved faster if we focus in the ASM-Full optimization, and the algorithm is more robust. Compared with a direct optimization of the cell in Ansys DesignerRF (using the available algorithms, GA is the one which offers better results) the simulation time is decreased at least in a factor of three in terms of time, and in many cases direct optimization is not able to find a suitable solution.

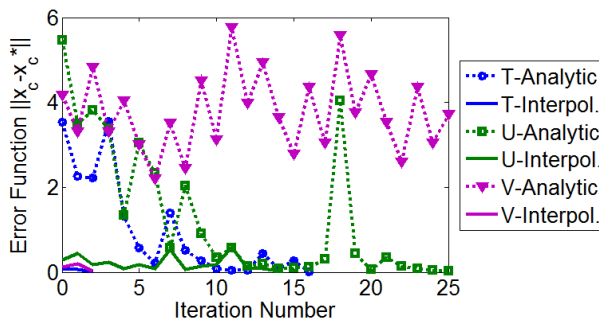


Fig. 3.32. - Evolution of the error with different analytical (dashed lines) and interpolated (solid lines) initial layouts: T (blue), U (green) and V (pink). Be aware that x-axis graphic starts in 0 instead of 1.

A very good agreement can be observed between the target and final layouts, as shown in Fig. 3.33. The frequency response of the first example (T) is

not reproduced again, since it was shown previously in section 3.3.1.3.1. In Fig. 3.33.b, for the case V, the initial layout is not depicted, because its response was so close to the target that traces were undistinguishable.

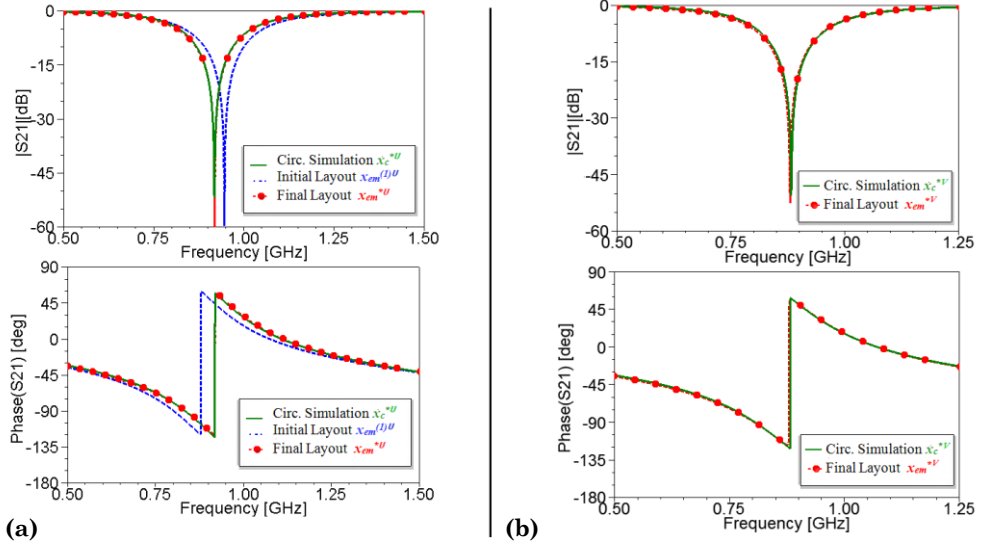


Fig. 3.33. - Frequency response of the transmission coefficient (S_{21}) in magnitude and phase: (a) Target U, (b) Target V

For the application of the algorithm to CSRR-gap-loaded metalinges, a differential aspect lies on the calculation of the convergence region. Different options were explored, as the determination with a 3D-convergence volume function of (L_c, C_c, C_g) as shown in Fig. 3.34.a, but finally a 2D- region function of (L_c, C_c) was chosen for simplicity (Fig. 3.34.b).

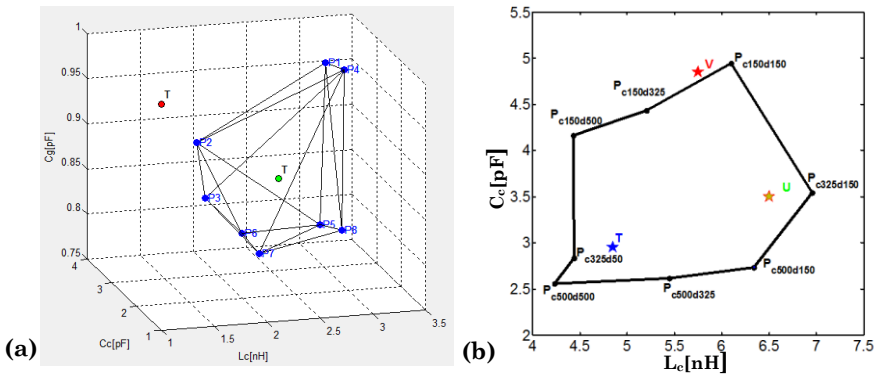


Fig. 3.34. - (a) 3D-Convergence region for $x_{cr}^* = [L^*, C^*] = [3.046 \text{ nH}, 12.144 \text{ pF}]$ (b) 2D-Convergence region for $x_{cr}^* = [L^*, C^*, C_g^*] = [9.45 \text{ nH}, 17.93 \text{ pF}, 1.01 \text{ pF}]$ cell with a T-shape gap. Substrate RO3010 $\epsilon_r = 10.2$. Thickness 1.27mm in (a), and 0.625mm in (b).

Therefore, the pre-optimization ASM algorithm involves three parameters, as shown in the schematic of Fig. 3.35. Consequently, the complexity is slightly increased, and also a bigger number of boundary points are needed to delimitate the convergence region accurately. The number of vertices is empirically estimated to be eight. Four of them are the same ones chosen for the CSRR-loaded metalines, plus the CSRR geometries given by $c_{min}-d_{mean}$, $c_{max}-d_{mean}$, $c_{mean}-d_{max}$, and $c_{mean}-d_{min}$, where $d_{mean}=(d_{min}+d_{max})/2$ and $c_{mean}=(c_{min}+c_{max})/2$. An illustrative example is shown in Fig. 3.34.b. considering $c_{min}=d_{min}=0.15$ mm and $c_{max}=d_{max}=0.5$ mm. Note that in the case of a cell with T-shaped-gap, the dimensions in the optimization space are changed from $x_{f_cr} = [l_{strip}, w_{strip}, s]$ to $x_{f_cr} = [l_{strip}, w_{strip}, w_g]$, since the gap length “s” is prefixed to certain small value.

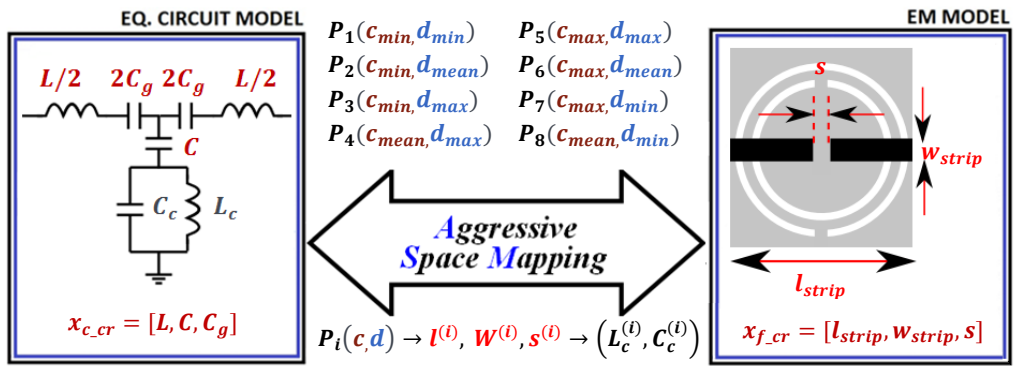


Fig. 3.35. - ASM pre-optimization diagram used to determine the convergence region for a CSRR-gap-loaded metaline.

The initial geometry derived from this procedure is very close to the final geometry, as it happened for the CSRR-loaded metalines. Proceeding in the same way as in we did with the previous unit cell, three different examples that share the same convergence region are reported. The different target vectors are summarized in Table 3.13, and are graphically depicted in Fig. 3.34.b, calculated for a T-shaped gap with $s = l_g = 0.2$ mm. Again, two of the points are placed inside the region of converge, while one (V) is placed outside the boundary limits.

Table 3. 13. - OPTIMAL COARSE SOLUTIONS

	L [nH]	C [pF]	C_g [pF]	L_c [nH]	C_c [pF]
T	9.45	17.93	1.01	4.85	2.95
U	9.45	17.93	1.01	6.50	3.50
V	9.45	17.93	1.01	5.75	4.85

After applying the ASM-full optimization, the final layouts collected in Table 3.14 are achieved (the stopping criterion for this case is $\|f_{norm}\| < 0.04$). It seems that now the process is not shortened as much as it was for CCSRR-loaded metalines, but depends on the case of study. Anyway, considering that the optimization process is unattended, the number of iterations is still a reasonable low number. As it is shown in Table 3.14, the point located out of the convergence region (i.e. target V) presents a final layout whose dimensions are not realizable with the proposed constraints ($c < 0.15$ mm).

Table 3. 14. - FINE PARAMETERS FOR THE FINAL LAYOUT, ITERATION NO. AND ERRORS

	l [mm]	W [mm]	c [mm]	d [mm]	W_g [mm]	Iter. No.	$\ f_{norm}\ $
T	14.2	0.87	0.34	0.40	7.13	6	0.0124
U	15.7	0.68	0.33	0.16	6.61	13	0.0292
V	17.1	0.56	0.13	0.21	6.07	13	0.0386

In Fig. 3.36, the frequency responses for the initial and final layouts (in this case, the considered full-wave electromagnetic solver for the CSRR-gap-loaded lines is Agilent Momentum), as well as for the circuit simulation of the target parameters, are shown for the T case. Results are in good agreement for the range of working frequencies (around 1GHz). However, at frequencies higher than 1.5 GHz, a mismatching between target and final layout are clearly observed, since the coarse model starts to be inaccurate.

This example constitutes the base for the implementation of a dual-band power divider application reported in next chapter. Actually, the target T coincides with the implemented cell for such an example (further details can be seen in section 4.2).

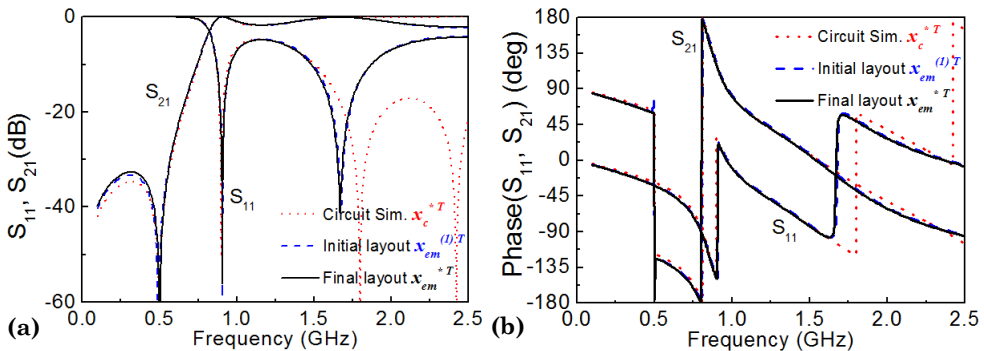


Fig. 3.36. - Comparison between the EM simulation of initial (blue dash line) and final layout (black solid line) and circuitual simulation (red dot line). (a) Magnitude and (b) phase of scattering parameters.

3.3.3.2 TLs based on OCSRRs

In the case of TLs based on OCSRRs, the convergence region is now used to determine if the particle is synthesizable but also an additional variable is included into the design: the width of the slot rings “ c ” that in previous version of the algorithm (see section 3.3.1) was fixed to a certain small value at the beginning of the optimization process. The schematic of the new proposed algorithm is shown below in Fig. 3.37. The initial layout is found by using an interpolation scheme, as we explained in the previous section. Hence, the most remarkable difference is that during the final optimization process r_{ext} is fixed, being the optimization variables: c , d and e .

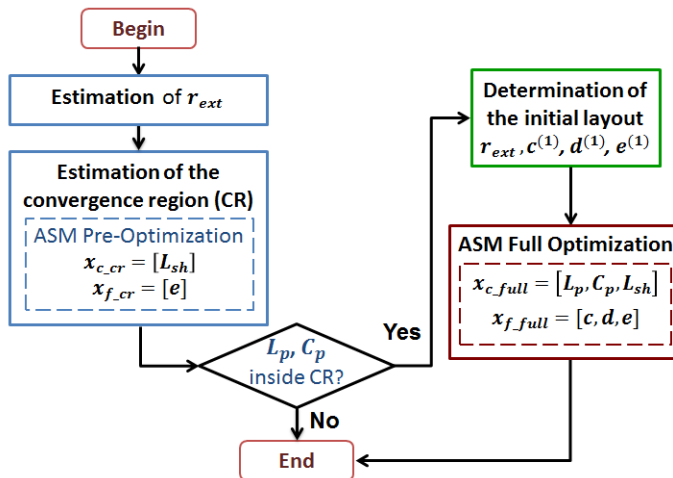


Fig. 3. 37. - Schematic of the new proposed ASM algorithm.

In first term, the convergence regions for different external radius values were calculated for the OCSRR unit cell, as shown in Fig. 3.38. It is observed, that the polygons are roughly scaled with the size of the radius. Obviously, the larger the external radius r_{ext} is, the larger the values of L_p and C_p at the vertexes of the polygon are. The boundaries (i.e. vertexes of the polygons) are determined through parameter extraction of the EM simulation responses at the limiting layouts. These layouts correspond to the extreme allowable values of the OCSRR dimensions (i.e. c and d), which mean four different combinations: (c_{min}, d_{min}) ; (c_{min}, d_{max}) ; (c_{max}, d_{min}) ; (c_{max}, d_{max}) . In the case of study (Fig. 3.38 and Fig. 3.40), the considered limiting boundaries are: $c_{min}=d_{min}=0.15\text{mm}$, $c_{max}=d_{max}=0.45\text{mm}$. To calculate the different convergence regions depicted in Fig. 3.38, no ASM optimization process was followed. They are just a rough

approximation (or fast approach), which considers “ e ”, the width of the strip present between the metallic region of the OCSR and the access line port (see detail in Fig. 3.40), a constant value which approximately provides the target value L_{sh}^* .

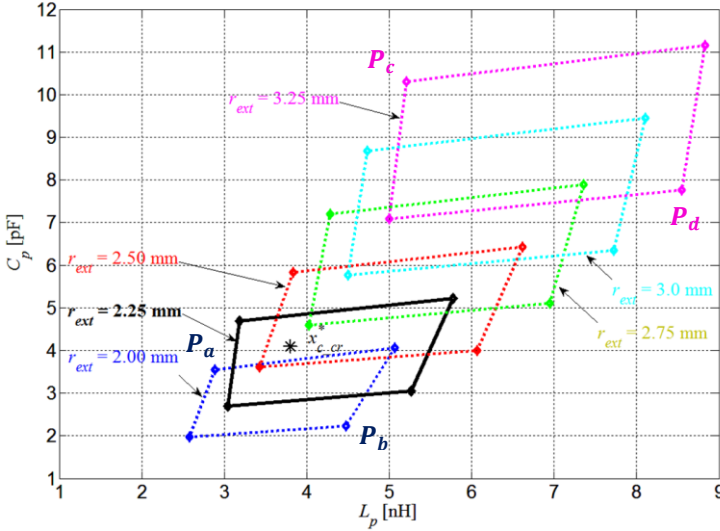


Fig. 3.38. - Estimated convergence regions calculated for external radius r_{ext} starting from 2 mm till 3.25 mm, in steps of 0.25 mm for an approximated target $L_{sh}^*=0.5$ nH, which corresponds to $e=0.277$ mm. The 4 vertexes are determined by the layouts obtained with the different combinations of the extreme values of c and d . $x_{c,cr}^* = [3.8$ nH, 4.1 pF].

There is an optimum radius for the considered target values of L_p and C_p (indicated by the symbol asterisk in Fig. 3.38), which is the smallest value that provides a polygon enclosing the target value of L_p and C_p . It is estimated to be around $r_{ext} = 2.25$ mm, being the corresponding polygon highlighted with solid black line.

The methodology proposed to obtain such radius (starting point of the algorithm in Fig. 3.37), considers the layouts corresponding to the following vertexes:

- $P_a \rightarrow r_{ext} = r_{min}; c = c_{min}; d = d_{max}$ (see Fig. 3.38 or Fig. 3.39)
- $P_b \rightarrow r_{ext} = r_{min}; c = c_{max}; d = d_{min}$ (see Fig. 3.38 or Fig. 3.39)
- $P_c \rightarrow r_{ext} = r_{max}; c = c_{min}; d = d_{max}$ (see Fig. 3.38 or Fig. 3.39)
- $P_d \rightarrow r_{ext} = r_{max}; c = c_{max}; d = d_{min}$ (see Fig. 3.38 or Fig. 3.39)

where r_{min} , r_{max} , c_{min} , c_{max} , d_{min} , d_{max} are certain reasonable values for the given topology. The values for the considered case are summarized in Table 3.16.

Table 3. 15. – VERTEXES FOR OCSRR RADIUS DETERMINATION

Limiting Layouts	L_p [nH]	C_p [pF]
$P_a \rightarrow r_{ext}[\text{mm}]=2.00, c[\text{mm}]=0.15, d[\text{mm}]=0.45$	2.8628	3.4824
$P_b \rightarrow r_{ext} [\text{mm}]=2.00, c[\text{mm}]=0.45, d[\text{mm}]=0.15$	4.5158	2.0932
$P_c \rightarrow r_{ext} [\text{mm}]=3.25, c[\text{mm}]=0.15, d[\text{mm}]=0.45$	5.2554	10.1826
$P_d \rightarrow r_{ext} [\text{mm}]=3.25, c[\text{mm}]=0.45, d[\text{mm}]=0.15$	8.6351	7.5822

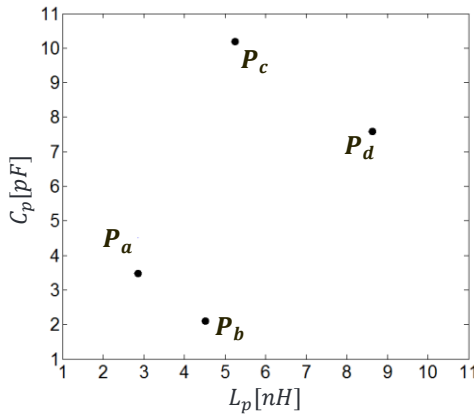


Fig. 3.39. – Graphical representation of the vertexes used for the OCSRR radius determination.

The radius (close to the optimum) can be estimated by interpolation. Assuming that each geometric variable (generically called z) has a linear dependence on L_p and C_p :

$$z = f(L_p, C_p) = a_0 + a_1 L_p + a_2 C_p + a_3 L_p C_p \tag{3.70}$$

where the constants a_i determine the functional dependence of the initial value of z with regard to L_p and C_p . To determine those constants, the expression (3.68) is minimized, but changing the dependence with L_c and C_c (characteristic of CSRR) to L_p and C_p (characteristic of OCSRR). The radius value has been found to be $r_{ext} = 2.198$ mm, and it will remain constant. The convergence polygon corresponding to such radius is depicted in Fig. 3.40, where the target value is also marked with a red dot. Notice that even the radius can be still optimized, the target point is very close to the diagonal of the polygon, so it can be considered a good value.

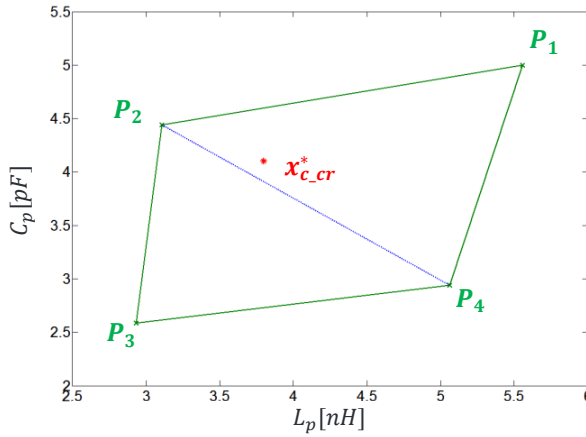


Fig. 3.40. - Estimated convergence region fixing the radius to $r_{ext}=2.198\text{mm}$. Red dot corresponds to the target given by: $L_p^*=3.8\text{ nH}$; $C_p^*=4.1\text{ pF}$.

For the sake of clarity, the procedure followed for the ASM Pre-Optimization is illustrated in Fig. 3.41. The initial value of e is that estimated by means of analytical formulas (see section 3.3.1.1.2).

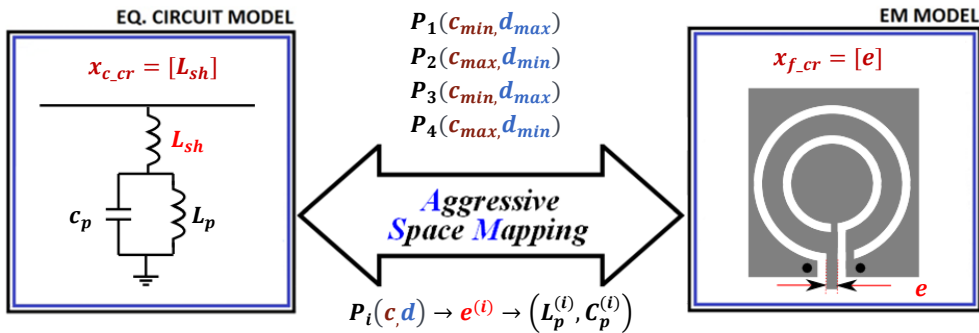


Fig. 3.41. - ASM Pre-optimization diagram for an OCSR-unit cell.

To determine the region in this particular case 13 EM simulations are needed (see Table 3.17). The matrix B is initialized, by perturbation of the initial layout (finite-difference scheme), only for the first vertex. For the next points B is that corresponding to the previous vertex.

Table 3. 16. - CONVERGENCE REGION VERTICES AND ASM ITERATIONS NEEDED

Limiting Layouts ($r_{ext}[\text{mm}] = 2.198$)	$L_p[\text{nH}]$	$C_p[\text{pF}]$	Iter. No
$P_1 \rightarrow c[\text{mm}]=0.15, d[\text{mm}]=0.15$	5.588	4.998	3 (4 EM Sim.)
$P_2 \rightarrow c[\text{mm}]=0.45, d[\text{mm}]=0.15$	3.105	4.443	4 (4 EM Sim.)
$P_3 \rightarrow c[\text{mm}]=0.15, d[\text{mm}]=0.45$	2.931	2.584	3 (3 EM Sim.)
$P_4 \rightarrow c[\text{mm}]=0.45, d[\text{mm}]=0.15$	5.062	2.938	2 (2 EM Sim.)

If the target is inside the convergence region, the initial layout is calculated similarly than in the procedure reported for CSRR-loaded lines. Actually, it is the interpolation procedure just described for the radius estimation, but now the limiting boundaries are those of the convergence region, summarized in Table 3.17. When the pair of values (L_p^* , C_p^*) coincides with any of the vertices of the polygon (in that particular case, the layout is already known, and, hence, no further optimization is necessary), though this step is not needed. The initial layout for the example (obtained by interpolation) can be found in Table 3.18.

Table 3. 17. - COARSE PARAMETERS FOR OCSRR UNIT CELL AND ERRORS

	$L_p[\text{nH}]$	$C_p[\text{pF}]$	$L_{sh}[\text{nH}]$	$\ f\ $	$\ f_{norm}\ $
Target (x_c^*)	3.800	4.100	0.500		
Initial ($x_c^{(1)}$)	3.696	3.981	0.511	0.1581	0.0451
Final	3.800	4.078	0.501	0.0239	0.0064

Once the parameters for the initial layout are determined, the ASM-full optimization process is applied. A solution is found when the norm of the error function is smaller than 1%. So, in the considered application example, just one iteration of the ASM-full algorithm is needed to find the optimum solution, see Fig. 3.42. The final layout dimensions are summarized in Table 3.17.

Table 3. 18. - FINE PARAMETERS FOR OCSRR UNIT CELL

	$r_{ext}[\text{mm}]$	$c[\text{mm}]$	$d[\text{mm}]$	$e[\text{mm}]$
Initial ($x_{em}^{(1)}$)	2.198	0.229	0.353	0.461
Final ($x_{em}^{(2)}$)	2.198	0.215	0.339	0.474
Final (section 3.3.1.3.2)	2.25	0.25	0.35	0.52

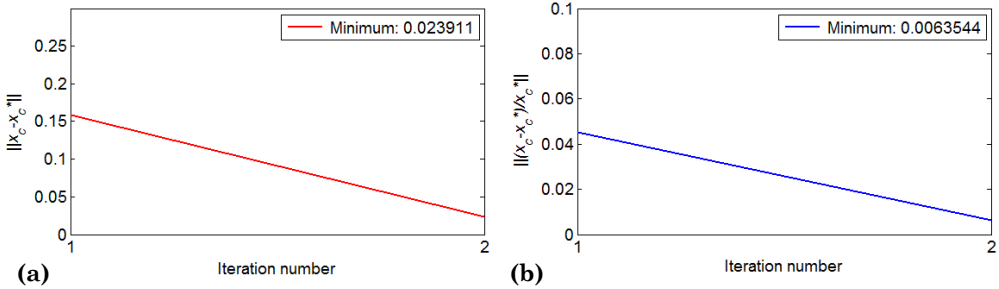


Fig. 3. 42. - Evolution of the error function with the iteration number: (a) $\|f\|$; (b) $\|f_{norm}\|$.

The circuit simulation of the target and the full-wave electromagnetic simulation of the generated layout are compared in Fig. 3.42. Again, the agreement is excellent, pointing out the validity of this alternative synthesis method. As compared to the OCSR synthesis reported in subsection 3.3.1.3.2, with identical target elements, the generated geometry with this new method has smaller values for the radius, as well as c and d dimensions, and hence a smaller OCSR size. For further details, an article focused on this topic [50] can be consulted.

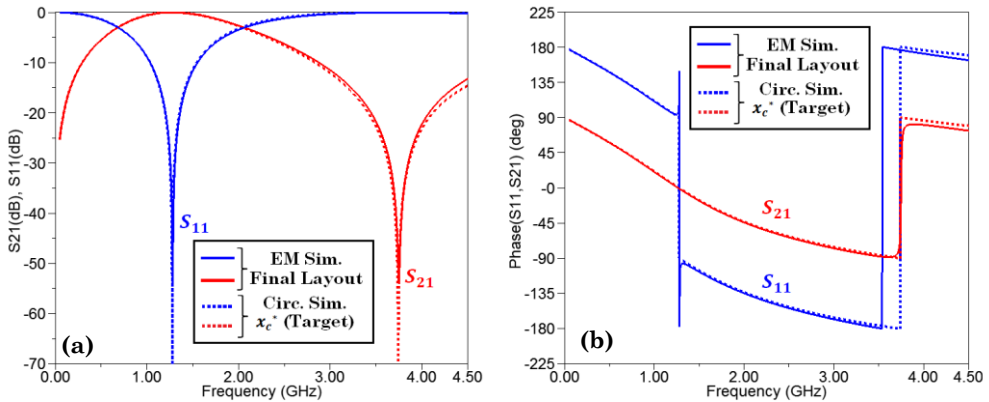


Fig. 3. 43. - Comparison of EM simulation of final layout (solid line) and circuit simulation (dot line) of target parameters: $x_c^* = [3.8\text{nH}, 4.1\text{pF}, 0.5\text{nH}]$; S-parameters in magnitude (a) and phase.

References

- [1] Y. Sawaragi, H. Nakayama, T. Tanino, *Theory of Multiobjective Optimization,* *Mathematics in Science and engineering*, vol. 176, Academic Press, London, 1985.
- [2] S. S. Rao, *Engineering Optimization: Theory and Practice*, Fourth Edition, John Wiley & Sons, Inc., Hoboken, NJ, USA, 2009.
- [3] A. Antoniou, Wu-Sheng Lu, *Practical Optimization: Algorithms and Engineering Applications*, Springer Science, New York 2007.
- [4] W. H. Press, S. A. Teukolsky, W. T. Vetterling, B. P. Flannery; *Numerical Recipes in C: The art of scientific computing*, Cambridge University Press, 2nd edition, 1992.
- [5] S. Koziel, D. Echeverría-Ciaurri, and L. Leifsson, “Surrogate-based methods,” in S. Koziel and X.S. Yang (eds.) *Computational Optimization, Methods and Algorithms, Series: Studies in Computational, Intelligence*, Springer-Verlag, pp. 33-60, Springer, 2011.
- [6] J.W. Bandler, R.M. Biernacki, S.H. Chen, P.A. Grobelny and R.H. Hemmers, “Space mapping technique for electromagnetic optimization,” *IEEE Transactions on Microwave Theory and Techniques*, vol. 42, pp. 2536-2544, Dec. 1994.
- [7] Third International Workshop on Surrogate Modelling and Space Mapping for Engineering Optimization. URL: <http://eomc.ru.is/smsmeo2012/>.
- [8] J.W. Bandler, R.M. Biernacki, S.H. Chen, R.H. Hemmers and K. Madsen, “Electromagnetic optimization exploiting aggressive space mapping,” *IEEE Transactions on Microwave Theory and Techniques*, vol. 43, no. 12, pp. 2874-2882, Dec. 1995.
- [9] J. W. Bandler, N. Georgieva, M. A. Ismail, J. E. Rayas-Sánchez, and Q. J. Zhang, “A generalized space mapping tableau approach to device modeling,” *IEEE Transactions on Microwave Theory and Techniques*, vol. 49, pp. 67–79, Jan. 2001.
- [10] M. H. Bakr, J.W. Bandler, R.M. Biernacki, S.H. Chen and K. Madsen, “A trust region aggressive space mapping algorithm for EM optimization,” *IEEE Transactions on Microwave Theory and Techniques*, vol.46, no. 12, pp. 2412-2425, Dec 1998.
- [11] J. W. Bandler, Q. Cheng, S. A. Dakroury, A. S. Mohamed, M. H. Bakr, K. Madsen, and J. Søndergaard, “Space mapping: The state of the art,” *IEEE*

Transactions on Microwave Theory and Techniques, vol. 52, no. 1, pp. 337–361, Jan. 2004.

[12] J.W. Bandler, Q.S. Cheng and S. Koziel, “Simplified space mapping approach to enhancement of microwave device models” *Int. J. RF Microw Comput-Aid Eng.* 2006.

[13] L. Encica, J. Paulides and E. Lomonova, “Space-mapping optimization in electromechanics: an overview of algorithms and applications,” *International Journal for Computation and Mathematics in Electrical and Electronic Engineering*, vol. 28, no. 5, 2009.

[14] S. J. Leary, A. Bhaskar and A. J. Keane, “A Constraint Mapping Approach to the Structural Optimization of an Expensive Model using Surrogates,” *Optimization and Engineering*, vol.2, issue 4, pp. 385-398, Dec. 2001.

[15] M. Redhe and L.Nilssonm, “Optimization of the new Saab 9-3 exposed to impact load using a space mapping technique,” *Structural and Multidisciplinary Optimization*, vol. 27, no. 5, pp. 411-420, July 2004.

[16] N. Marheineke and R. Pinnau, Model hierarchies in space-mapping optimization: feasibility study for transport processes,” *Journal of Computational Methods in Sciences and Engineering*, Special issue on Advances in Simulation-Driven Optimization and Modeling, vol. 12 Issue 1-2, pp. 63-74, Jan. 2012.

[17] C. G. Broyden, “A class of methods for solving non-linear simultaneous equations,” *Mathematics of Computation*, vol. 19, pp. 577–593, 1965.

[18] M. H. Bakr, J.W. Bandler, K. Madsen, and J. Søndergaard, “Review of the space mapping approach to engineering optimization and modeling,” *Optimization and Engineering*, vol. 1, no. 3, pp. 241–276, Sept. 2000.

[19] M. H. Bakr, J.W. Bandler, N. Georgieva and K. Madsen, “A hybrid aggressive space-mapping algorithm for EM optimization,” *IEEE Transactions on Microwave Theory and Techniques*, vol.47, no.12, pp. 2440-2449, Dec. 1999.

[20] M. H. Bakr, J.W. Bandler, K. Madsen, J. E. Rayas-Sanchez and J. Søndergaard, “Space-mapping optimization of microwave circuits exploiting surrogate models,” *IEEE Transactions on Microwave Theory and Techniques*, vol.48, no.12, pp.2297-2306, Dec. 2000.

[21] J. E. Rayas-Sanchez, “EM-based optimization of microwave circuits using artificial neural networks: the state-of-the-art,” *IEEE Transactions on Microwave Theory and Techniques*, vol.52, no.1, pp.420-435, Jan. 2004.

- [22] S. Koziel, J.W. Bandler and K. Madsen, "A Space-Mapping framework for engineering optimization: theory and implementation," *IEEE Transactions on Microwave Theory and Techniques*, vol.54, no.10, pp.3721-3730, Oct. 2006.
- [23] S. Koziel and J. W. Bandler, "Recent advances in space-mapping-based modeling of microwave devices," *International Journal of Numerical Modelling: Electronic Networks, Devices and Fields*, vol. 23, pp. 425-446, Jan. 2010
- [24] S. Koziel, L. Leifsson and S. Orgustov "Space Mapping for Electromagnetic-Simulation-Driven Design Optimization" in S. Koziel and L. Leifsson (eds.) *Surrogate-Based Modeling and Optimization, Application in Engineering*, pp. 1-25, Springer, 2013.
- [25] J.W. Bandler, Q.S. Cheng, N.K. Nikolova, and M.A. Ismail, "Implicit space mapping optimization exploiting preassigned parameters," *IEEE Transactions on Microwave Theory and Techniques*, vol. 52, no. 1, pp. 378–385, Jan. 2004.
- [26] A. Khalatpour, R. K. Amineh, Q. S. Cheng, M. H. Bakr, N. K. Nikolova, and J. W. Bandler, "Accelerating input space mapping optimization with adjoint sensitivities," *IEEE Microwave Wireless Components Letters*, vol. 21, no. 6, pp. 280–282, Jun. 2011.
- [27] S. Koziel, S. Orgustov , J.W. Bandler and Q.S. Cheng "Reliable Space-Mapping optimization integrated with EM-based adjoint sensitivities," *IEEE Transactions on Microwave Theory and Techniques*, vol.61, no.10, pp. 3493-3502, Oct. 2013.
- [28] J. Meng, S. Koziel, J. W. Bandler, M. H. Bakr and Q.S. Cheng, "Tuning space mapping: A novel technique for engineering design optimization," *IEEE MTT-S International Microwave Symposium Digest*, pp. 991-994, June 2008.
- [29] Q.S. Cheng, J.W. Bandler and S. Koziel, "Tuning space mapping: The state of the art", *International Journal of RF and Microwave Computer-Aided Engineering*, vol. 12, is. 16, Nov. 2012.
- [30] J.C. Rautio, "Perfectly calibrated internal ports in EM analysis of planar circuits," *IEEE MTT-S International Microwave Symposium Digest*, pp. 1373–1376, June 2008.
- [31] J.E. Rayas-Sanchez and V. Gutiérrez-Ayala, "EM-based Monte Carlo analysis and yield prediction of microwave circuits using linear-input neural-output space mapping," *IEEE Transactions on Microwave Theory and Techniques*, vol. 54, pp. 4528–4537, Dec. 2006.
- [32] S. Koziel, J.W. Bandler and Q.S. Cheng, "Reduced-cost microwave component modeling using space mapping-enhanced electromagnetic-based

kriging surrogates”, *International Journal of Numerical Modelling: Electronic Networks, Devices and Fields*, vol. 26, pp. 275-286, March 2013.

[33] J. D. Baena, J. Bonache, F. Martín, R. M. Sillero, F. Falcone, T. Lopetegi, M. A. G. Laso, J. Garcia-Garcia, I. Gil, M. F. Portillo, and M. Sorolla, “Equivalent-circuit models for split-ring resonators and complementary split-ring resonators coupled to planar transmission lines,” *IEEE Transactions on Microwave Theory and Techniques*, vol. 53, no.4, pp.1451-1461, April 2005.

[34] J. Bonache, M. Gil, I. Gil, J. Garcia-García and F. Martín, “On the electrical characteristics of complementary metamaterial resonators , *IEEE Microwave Wireless Component Letters*, vol. 16, pp. 543-545, Oct. 2006.

[35] F. Falcone; T. Lopetegi; J. D. Baena, R. Marqués; F Martín and M. Sorolla, “Effective negative- ϵ stopband microstrip lines based on complementary split ring resonators”, *IEEE Microwave and Wireless Components Letters*, vol. 14, no. 6, pp.280-282, June 2004.

[36] R. S. Kallapudi, S. S. Karthikeyan, “Stop band characteristics for periodic patterns of CSRRs in the ground plane”. *International Journal of Microwave and Optical Technology*, vol. 2, no. 3, pp. 210-215, July 2007.

[37] J. Bonache, M. Gil, O. Garcia-Abad, and F. Martín, “Parametric analysis of microstrip lines loaded with complementary split ring resonators”, *Microwave and Optical Technology Letters*, vol. 50, no. 8, pp. 2093-2096, Aug. 2008.

[38] M. Gil, “Resonant-type Metamaterial Transmission Lines and Their Application to Microwave Device Design”, PhD Thesis, Universitat Autònoma de Barcelona, 2009.

[39] M. Gil, J. Bonache, J. Selga, J. Garcia-Garcia, and F. Martín, “Broadband resonant-type metamaterial transmission lines”, *IEEE Microwave and Wireless Components Letters*, vol. 17, no. 2, pp. 97-99, Feb. 2007.

[40] M. Gil, J. Bonache, I. Gil, J. Garcia-Garcia, F. Martín “Artificial left-handed transmission lines for small size microwave components: application to power dividers,” *Proceedings of 36th European Microwave Conference*, pp.1135-1138, 10-15 Sept. 2006.

[41] M. Duran-Sindreu, A. Velez, F. Aznar, G. Siso, J. Bonache and F. Martín, “Application of open split ring resonators and open complementary split ring resonators to the synthesis of artificial transmission lines and microwave passive components,” *IEEE Transactions on Microwave Theory and Techniques*, vol. 57, pp. 3395-3403, Dec. 2009.

[42] P. Velez, J. Naqui, M. Duran-Sindreu, J. Bonache, and F. Martín, “Broadband microstrip bandpass filter based on open complementary split ring

resonators,” *International Journal of Antennas and Propagation*, article ID 174023, pp. 1-6, Oct. 2012.

[43] K. C. Gupta, R. Garg, I. Bahl and P. Bhartia, *Microstrip Lines and Slotlines*, 2nd edition, Artech House Microwave Library, 1996.

[44] F. Aznar-Ballesta, M. Gil, M. Duran-Sindreu, J. Bonache and F. Martín “Characterization of metamaterial transmission lines with coupled resonators through parameter extraction”, *Metamaterial*, Dr. Xun-Ya Jiang (Ed.), chapter 12, pp. 303-320, InTech, May 2012.

[45] J. Selga, A. Rodríguez, M. Gil, J. Carbonell, V. E. Boria, and F. Martín, “Synthesis of planar microwave circuits through aggressive space mapping using commercially available software packages”, *International Journal of RF and Microwave Computer-Aided Engineering*, vol. 20, no. 5, pp. 527-534, Sep. 2010.

[46] A. Rodriguez, J. Selga, M. Gil, J. Carbonell, V. E. Boria, and F. Martin, “Automated synthesis of resonant-type metamaterial transmission lines using aggressive space mapping”, *IEEE MTT-S International Microwave Symposium Digest*, Anaheim, CA, USA, pp. 209-212, May 2010.

[47] A. Rodríguez, J. Selga, F. Martín, and V. E. Boria, “On the implementation of a robust algorithm which automates the synthesis of artificial transmission lines based on CSRRs”, *Proceedings of International Congress on Advanced Electromagnetic Materials in Microwaves and Optics*, Barcelona, Spain, Oct. 2011.

[48] J. Selga, A. Rodriguez, V. E. Boria, and F. Martin, “Synthesis of split rings based artificial transmission lines through a new two-step, fast converging, and robust Aggressive Space Mapping (ASM) algorithm”, *IEEE Transactions on Microwave Theory and Techniques*, vol. 61, no. 6, pp. 2295-2308, June 2013.

[49] A. Rodriguez, V. E. Boria, J. Selga, and F. Martin, “A robust space mapping method for the practical synthesis of CSRR-based artificial transmission lines from equivalent circuit models”, *Proceedings of 42nd European Microwave Conference (EuMC)*, Amsterdam (The Netherlands), pp. 671-674, 28 Oct.-2 Nov. 2012.

[50] J. Selga, A. Rodriguez, M. Orellana, V. E. Boria, and F. Martin, “Practical application of space mapping techniques to the synthesis of CSRR-based artificial transmission lines,” *Applied Physics A*, pp. 1-9, Sept. 2014. Available already on line: <http://link.springer.com/article/10.1007/s00339-014-8703-x>

CHAPTER 4

Applications

- 4.1 *Band-stop filter based on CSRR-loaded metalines*
- 4.2 *Dual-band power divider based on CSRR-gap-loaded metalines*
- 4.3 *Band-pass filter based on OCSRRs transmission lines*

References

“Engineering is the art or science of making practical”

S. C. Florman

“A good idea, properly understood, always has a practical application”

Jimi Morgan



4 APPLICATIONS

As a validation of the synthesis techniques developed in this thesis work, several application examples have been designed, fabricated and measured. Three prototypes implemented on microstrip technology, based on the different cells of study considered in the past chapter (i.e. CSRR-loaded metalines, CSRR-gap-loaded metalines and OCSRRLs transmission lines) are presented.

4.1 Band-stop filter based on CSRR-loaded metalines

The first example is a band-stop filter that consists on cascading different unit cells of CSRR-loaded metalines, in this case just three cells as it is depicted in Fig. 4.1. The main application of this kind of filter is to reject the unwanted spurious band in the microwave range, and thanks to this technology it can be obtained by means of a planar and compact design.

The design process starts with the synthesis of the central unit cell. Since the central frequency of the stop-band is aimed to be 2.45 GHz, the transmission zero frequency (f_z) given by expression (3.32) is set to that frequency value. The other cells involved in the design will have similar target responses, and therefore very close transmission zero frequencies (i.e. 2.36 GHz and 2.53 GHz). Thus, the optimal coarse solutions for all the involved cells were forced to be placed in the same convergence region (i.e. with the same target parameters L^* and C^* , as it can be observed in Table 4.1), in order to speed up the design process as explained in section 3.3.3.1. The number of iterations to determine the region was approximately 3 by vertex (worst case 5, the best case only one).

Table 4. 1. - OPTIMAL COARSE SOLUTIONS (UNIT CELLS)

	L [nH]	C [pF]	L_c [nH]	C_c [pF]
$C_{2.36}$	3.194	1.363	1.009	3.143
$C_{2.45}$	3.194	1.363	0.941	3.120
$C_{2.53}$	3.194	1.363	0.882	3.125

It was observed that, by cascading the three cells directly, coupling effects between them appear, which the equivalent circuit or coarse model does not take

into account. For this reason transmission line sections are inserted between adjacent cells, in order to avoid- or minimize- that effect, see Fig. 4.1 and Fig. 4.2. The length of the transmission lines has been fixed to a certain small value (approximately half of the CSRR radius value), in our case we have used a length of 2.22 mm, which means approximately 3/4 of the CSRR radius, obtained after performing different EM solutions. With this separation between cells, the reduction of the rejection level and bandwidth of the resulting band-stop filter (due to undesired coupling effects) can be neglected.

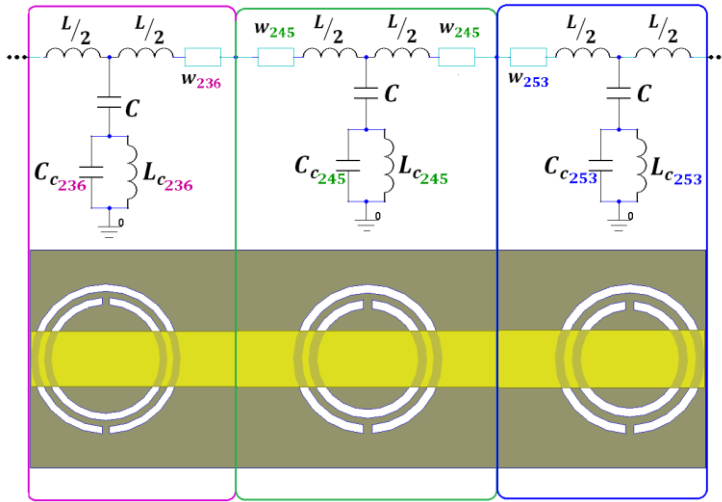


Fig. 4.1. - Equivalent circuit and layout of the implementer band-stop filter. The small blue rectangles correspond to lines of physical length equal to 2.22mm and width according to the calculated value for each unit cell (see Table 4.2).

The layout of the different cells is summarized in Table 4.2 with the number of iterations corresponding to the final ASM full-optimization process and normalized errors (all under 1%). The substrate used is Rogers RO3010 with thickness $h=1.27$ mm and dielectric constant $\epsilon_r=10.2$.

Table 4. 2. - FINE PARAMETERS FOR THE FINAL LAYOUT, ITERATION NO. AND NORMALIZED ERROR

Cell (f_z)	l [mm]	W [mm]	c [mm]	d [mm]	Iter. No.	$\ f_{norm}\ $
2.36 GHz	5.93	2.16	0.28	0.25	3	0.0074
2.45 GHz	5.91	2.23	0.34	0.27	1	0.0055
2.53 GHz	5.93	2.25	0.34	0.33	5	0.0069

In Fig. 4.2 the completed fabricated filter is shown. As it can be clearly seen in Fig. 4.2.b, tapers were introduced at both edges to perform the measurements (i.e. softer transitions to the 50Ω line). A prototype was fabricated in-house by using the commercial circuit board plotter LPKF ProtoMat S103.

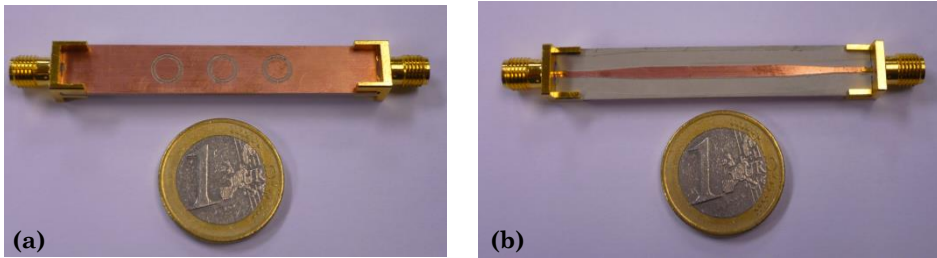


Fig. 4.2. - Manufactured prototype layout: (a) Ground. (b) Top.

Finally, for comparison purposes, the measured filter response (solid black trace), the EM simulated response (green dot-dot-dash line) and the circuitual model response (blue dash line) are displayed together in Fig. 4.3. The measured rejection level is better than 20 dB within a frequency band of 345 MHz. These results are in good agreement with the ones predicted by simulation in the band of interest. Some discrepancies are observed in the out of band frequency range which can be attributed to fabrication tolerances. The circuit simulation corresponds to the circuit illustrated in Fig. 4.1, which includes the line transmission line sections modelled as ideal microstrip lines (with width W and length $l=2.22$ mm).

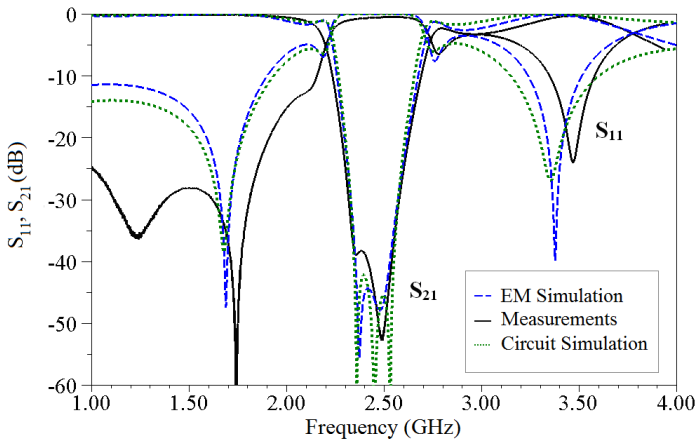


Fig. 4.3. - Magnitude of the scattering parameters S_{21} and S_{11} , in blue-dash line the circuitual simulation, in green-dot-dot-dash line the EM simulation, and in black-solid line the measurements.

All these results (successful comparison in the region of interest) fully validate the design process of the proposed band-stop filter and their constituent cells. All simulations were performed with ANSYS DesignerRF. More details about the design technique just presented can be found in [1].

4.2 Dual-band power divider based on CSRR-gap-loaded metalines

For the second example, a dual-band power splitter based on a dual-band impedance inverter, implemented by means of the CSRR-gap-loaded metaline, is considered. To achieve the dual-band functionality, the inverter must provide a phase shift of -90 and $+90$ degrees at the operating frequencies, f_1 and f_2 , respectively. Therefore, the composite right/left handed behaviour of the structure is exploited, being f_1 and f_2 located in the left-handed and right-handed regions, respectively (see chapter 2). The inverter impedance is set to 35.35Ω at both frequencies, in order to guarantee a good matching when the inverter output port is loaded with the two 50Ω access lines (terminated with a pair of matched loads) to implement the divider. Fig. 4.4 shows the schematic of the proposed dual-band power divider (where two section lines of characteristic impedance equal to 35.35Ω are introduced for practical implementation issues, see more details about it next and in [1]. The design operating frequencies of the inverter are set to: $f_1 = 0.9 \text{ GHz}$ and $f_2 = 1.8 \text{ GHz}$, because these are frequencies widely used in GSM-900 and GSM-1800 bands.

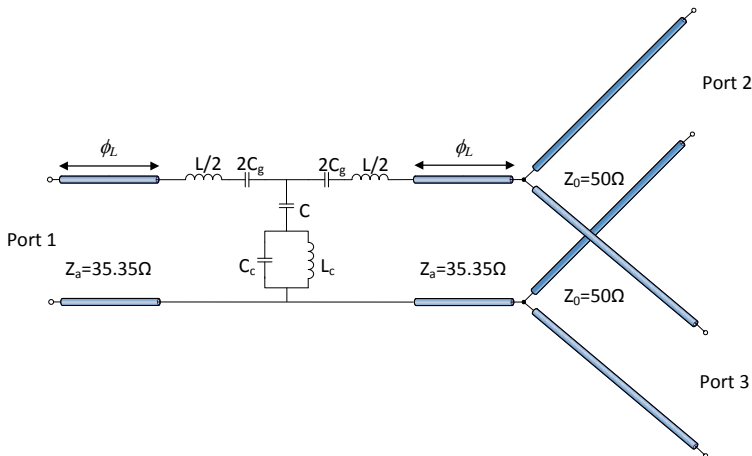


Fig. 4.4. –Schematic of the final prototype.

To univocally determine the five target parameters which define the CSRR-gap-loaded line (i.e. L, C, L_c, C_c, C_g see Fig. 4.4), we need to impose five different conditions. Four conditions are given by the system of equations (2.43)-(2.46), where Z_a is the inverter impedance, f_1 and f_2 the two inverter operation frequencies. The other condition comes from the transmission zero frequency, given by expression (3.32), which is forced to be $f_z = 0.5$ GHz. The calculated values are summarized in Table 4.3 (labeled as Initial Target Estimation). For completeness, resulting analytical expressions are given next:

$$L = \frac{2 Z_a}{\omega_2 - \omega_1} \tag{4.1}$$

$$C_g = \frac{1}{2} \cdot \frac{\omega_2 - \omega_1}{\omega_1 \omega_2 Z_a} \tag{4.2}$$

$$C = \frac{(\omega_z^2 - \omega_2^2) \cdot \omega_1^2 - \omega_1 \omega_2 \omega_z^2 + \omega_2^2 \omega_z^2}{\omega_1 \cdot \omega_2 \cdot \omega_z^2 Z_a \cdot (\omega_2 - \omega_1)} \tag{4.3}$$

$$C_c = \frac{((\omega_2^2 - \omega_z^2) \cdot \omega_1^2 + \omega_1 \omega_2 \omega_z^2 - \omega_2^2 \omega_z^2)(\omega_1 \omega_2 - \omega_z^2)}{(\omega_2^2 - \omega_z^2) \cdot (\omega_1^2 - \omega_z^2) \cdot \omega_1 \cdot \omega_2 Z_a} \tag{4.4}$$

$$L_c = \frac{(\omega_2^2 - \omega_z^2) \cdot (\omega_1^2 - \omega_z^2) \cdot \omega_1 \cdot \omega_2 Z_a}{(\omega_1^2 - \omega_z^2) \cdot \omega_2^2 + \omega_1 \omega_2 \omega_z^2 - \omega_1^2 \omega_z^2} \tag{4.5}$$

However, once the ASM pre-optimization technique described in previous chapter is applied to determine the convergence region for this cell, it is found that the inferred target element values cannot be not physically implementable (with the chosen substrate Rogers RO3010, of thickness $h= 0.635$ mm and dielectric constant $\epsilon_r=10.2$).

Table 4. 3. - OPTIMAL COARSE SOLUTIONS

	L [nH]	C [pF]	C_g [pF]	L_c [nH]	C_c [pF]
Initial Target Estimation	12.5	24.9	1.25	3.38	5.10
Final Target (T)	9.45	17.93	1.01	4.85	2.95

Nevertheless, by cascading two transmission line sections (of characteristic impedance Z_a) to the input and output ports of the proposed cell, the new element values of the unit cell are not so extreme, resulting in an implementable CSRR-gap loaded unit cell that has been synthesized by means of the algorithm

presented in section 3.3.3.1. The width of these line sections is 1.127 mm, corresponding to the indicated characteristic impedance ($Z_a = 33.35 \Omega$) in the considered substrate RO3010. Notice that by cascading such lines, the electrical length at the operating frequencies is the sum of the electrical lengths of the lines and of the CSRR-based cell. Thus, the phase condition that must satisfy the CSRR-gap loaded line is expressed by:

$$\phi_1 = -90^\circ - 2\phi_L(f_1) \quad (4.6)$$

and

$$\phi_2 = +90^\circ - 2\phi_L(f_2) \quad (4.7)$$

where ϕ_1 and ϕ_2 are the electrical lengths of the CSRR-based cell at the design frequencies f_1 and f_2 , and ϕ_L is the phase introduced by the line at the indicated frequencies. So the new system of equations to determine the target is given by:

$$Z_{se}|_{f_1} = j \frac{Z_a(\cos(\phi_1) - 1)}{\sqrt{1 - \cos^2(\phi_1)}} \quad (4.8)$$

$$Z_{se}|_{f_2} = -j \frac{Z_a}{\sqrt{1 - \cos^2(\phi_1)}} \quad (4.9)$$

$$Z_{par}|_{f_1} = -j \frac{Z_a(\cos(\phi_2) - 1)}{\sqrt{1 - \cos^2(\phi_2)}} \quad (4.10)$$

$$Z_{par}|_{f_2} = j \frac{Z_a}{\sqrt{1 - \cos^2(\phi_2)}} \quad (4.11)$$

instead of (2.43)-(2.46), plus the equation (3.32).

A parametric analysis, consisting on obtaining the element values of the CSRR-based cell for different values of the length of the additional cascaded transmission line sections (and hence $\phi_L(f_1)$ and $\phi_L(f_2)$), has been performed. As observed in Fig. 4.5, small values of $\phi_L(f_1)$ leads to large values of L and C , which are not implementable (large L means small W , which implies a small value for C). On the other hand, the values of L_c and C_c without cascaded line sections, i.e. $\phi_L(f_1) = 0^\circ$, produce extreme values of width and separation between the slot rings (large value of d and small value of c). So, to overcome this issue, a pair of transmission line sections with $\phi_L(f_1) = 15^\circ$, which means that the required electrical lengths for the CSRR-based cell at the operating

frequencies are according to expression (4.6) and (4.7): $\phi_1 = -120^\circ$, $\phi_2 = 30^\circ$. It is worth mentioning that C_g does not experience significant variations with $\phi_L(f_1)$.

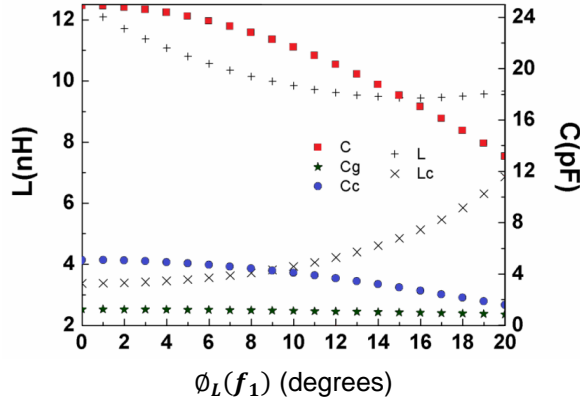


Fig. 4.5. –Dependence of the element values of the CSRR-gap loaded line with the phase of each cascaded transmission line section at f_1 .

The obtained target parameters can be found in Table 4.3 (labeled as Final Target). Since these target values correspond to one of the application examples of previous chapter (section 3.3.3.1), the corresponding physical dimensions are collected in Table 4.4.

Table 4. 4. - FINE PARAMETERS FOR FINAL CSRR-GAP-LOADED LINE UNIT CELL (T-SHAPE GAP)

l [mm]	W [mm]	c [mm]	d [mm]	W_g [mm]
14.2	0.87	0.34	0.40	7.13

The fabricated device is shown in Fig. 4.6, where access lines of 50Ω for connector soldering are observed. In this case, the prototype was fabricated using a photo/mask etching process in order to get better accuracy than with circuit board plotter.

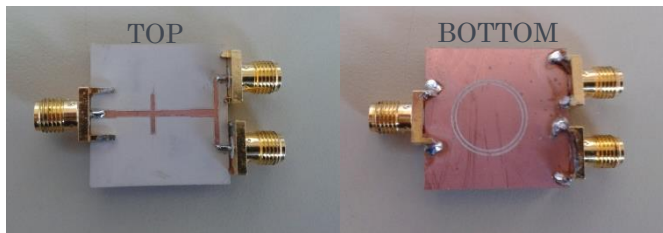


Fig. 4.6. – Photograph of the designed dual band power divider.

In Fig. 4.7, a graphic with the electrical length (βl) and the characteristic impedance (Z_a) of the inverter, obtained from EM and circuit simulations, are shown. There is a very good agreement for the left-handed band, even not so good for the right-handed one. This is due to the fact that the equivalent circuit model starts to be inaccurate as frequency is increased, as it was already known and expected. Anyway the phase shift and the characteristic impedance at f_2 are reasonably close to the nominal values, and hence it is expected that the functionality of the device at f_2 is preserved.

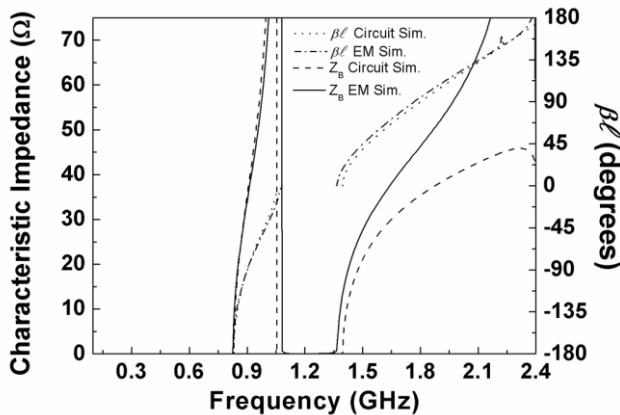


Fig. 4.7. – Comparison between the EM and circuit simulations corresponding to the characteristic impedance (Z_B) and electrical length (βl) of the designed prototype.

The frequency responses of the synthesized divider are shown in Fig. 4.8, where optimum matching occurs at f_1 and slightly below f_2 . The differences observed at high frequencies (in the right-handed band) can be attributed to the coarse model used, but not to the methodology. In order to achieve better results at high frequencies, a more accurate circuit model should be used to describe the unit cell. In this application example, the EM solver used in the design process was Agilent Momentum. This example, as well as the previous one (WIFI stop-band filter), are published in [1].

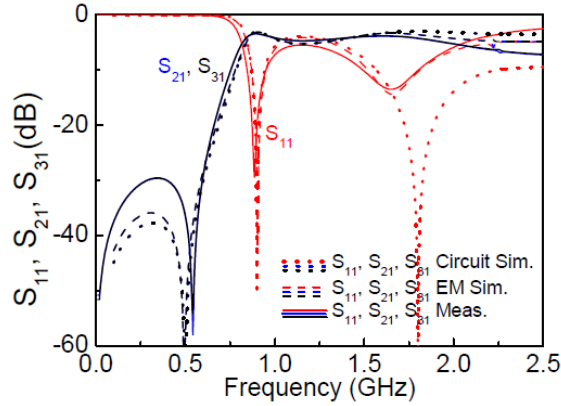


Fig. 4.8. –Frequency response (circuit and EM simulation and measurement) of the designed and fabricated dual-band power divider (magnitude of the scattering parameters).

4.3 Bandpass filter based on OCSRRs TLs

OCSRRs can be used for the design of wideband bandpass filters based on shunt resonators coupled through admittance inverters, as it was briefly outlined in chapter 2. The proposed filter synthesis is obtained by following the ASM method reported in section 3.3.1, without previous calculation of the convergence region for the target parameters as we did in the previous examples reported in this chapter.

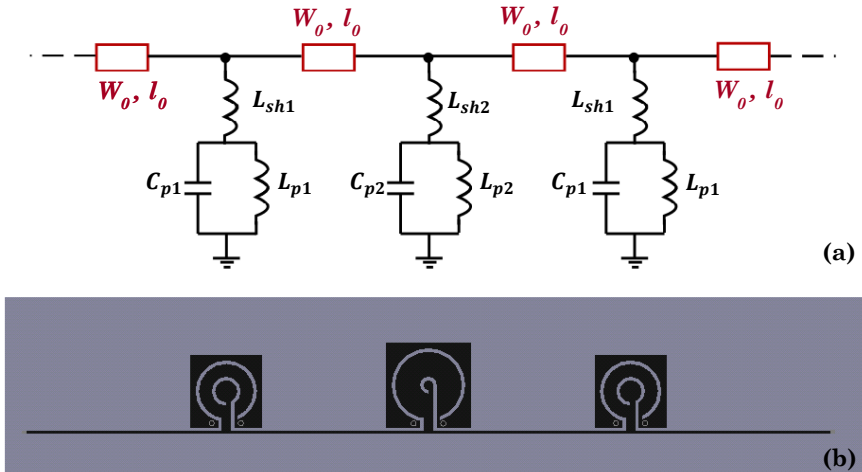


Fig. 4.9.- Schematic of the 3-order bandpass filter (a), and layout inferred after the synthesis process (b). The circuit target parameters are summarized in Table 4.6 and dimensions in Table 4.6. Microstrip line parameters: $w_0 = 0.211$ mm and $l_0 = 14.94$ mm.

Chapter 4. Applications

The layout of the proposed filter is described by the schematic depicted in Fig. 4.9.a, which roughly corresponds to a 3rd-order Chebyshev band-pass filter with a central frequency $f_0=2$ GHz, a fractional bandwidth $FBW= 30\%$, and 0.01 dB of ripple. The calculated target values using a commercial substrate *Rogers* RO3010 with dielectric constant $\epsilon_r=10.2$ and thickness $h= 0.254$ mm can be found in Table 4.5. Different OCSR resonators are considered, so inverters are forced to be $J_{01} = J_{12} = J_{23} = J_{34} = 0.02$ S. The inverters are implemented by means of $\lambda/4$ lines (being λ the wavelength at the filter central frequency) of characteristic impedance 50Ω . However, the limited functionality of these transmission lines as admittance inverters prevents from obtaining the ideal Chebyshev response at the schematic level with the present approach. Furthermore, the ideal Chebyshev response is also altered by the transmission zeros related to the inductances L_{sh_i} , which improve filter selectivity. Such transmission zeros are set to $f_z= 4.408$ GHz for the first resonator, and to $f_z= 3.588$ GHz for the second resonator (the third resonator is identical to the first one as it is shown in Fig. 4.9).

Table 4. 5. - OPTIMAL COARSE SOLUTIONS, REFLECTION AND TRANSMISSION ZERO FREQUENCIES

	L_p [nH]	C_p [pF]	L_{sh} [nH]	f_0 [GHz]	f_z [GHz]
C1, C3	1.813	3.479	0.472	2	4.408
C2	1.143	5.568	0.517	2	3.558

The final dimensions of the involved unit cells, together with the number of iterations needed to synthesize them and the normalized final error (all under 1.3%), are summarized in Table 4.6. The width of the slot rings was fixed to $c=0.25$ mm, and the dimensions of the strip line that models the $\lambda/4$ inverter (electrical length 90° at f_0) are $w_0= 0.211$ mm and $l_0 = 14.94$ mm.

Table 4. 6. - FINE PARAMETERS FOR OCSR UNIT CELL, ITERATION NUMBER AND ERRORS

		r_{ext} [mm]	d [mm]	e [mm]	Iter. No.	$\ f\ $	$\ f_{norm}\ $
C1,C3 ($c=0.25$ mm)	Initial ($x_{em}^{(1)}$)	4	1.34	0.46	1	8.4542	2.5061
	Final ($x_{em}^{(6)}$)	2.27	0.95	0.70	6	0.0175	0.0100
C2 ($c=0.25$ mm)	Initial ($x_{em}^{(1)}$)	4	1.01	0.28	1	7.5932	2.6800
	Final ($x_{em}^{(9)}$)	2.72	1.84	0.75	9	0.0123	0.0122

As it can be seen in Fig. 4.10, the agreement between the target (schematic) response and the electromagnetic simulation of the synthesized layout is good (losses are not included). In this case, since the unit cells are already sufficiently spaced, coupling effects are not observed. However, it appears a spurious band due the presence of the characteristic transmission zeros of the OCSRRs, and that their position was not considered during the first initial design. For comparison, we also include the measured frequency response with black solid trace, being in a reasonable agreement with the EM simulations and then proving the validity of the proposed design method.

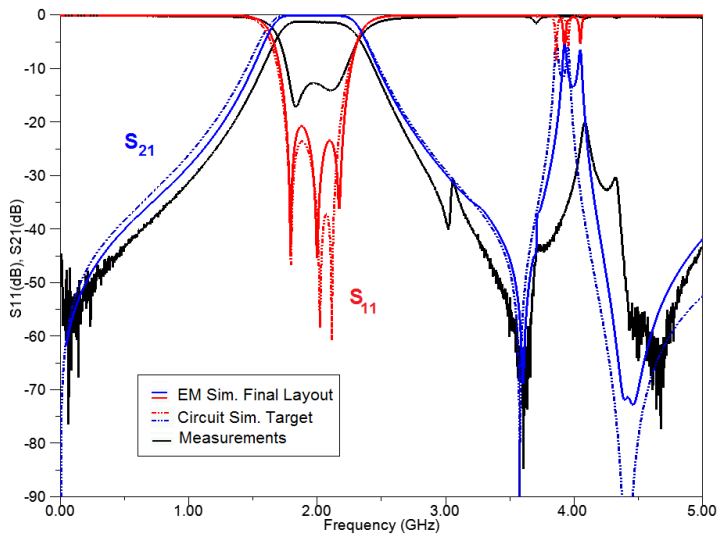


Fig. 4.10. - Insertion and return losses of the synthesized bandpass filter based on OCSRRs.

The filter was fabricated with an LPKF ProtoMat HF-100 drilling machine, and its layout is graphically shown in Fig. 4.11.



Fig. 4.11. - Photograph of the manufactured filter.

The identified spurious band can be avoided by properly designing the OCSRR cells, i.e. forcing all the transmission zeros to the same frequency:

Chapter 4. Applications

$f_{z,c1} = f_{z,c2} = f_{z,c3} = 3.9$ GHz. The new target parameter values are summarized in Table 4.7, and they are obtained according to the following expressions:

$$L_{p_i} = \frac{1}{\omega_0 b_i} \quad (4.12)$$

$$C_{p_i} = \frac{b_i}{\omega_0} \quad (4.13)$$

$$L_{sh_i} = \frac{\omega_0}{b_i \cdot (\omega_z^2 - \omega_0^2)} \quad (4.14)$$

being $b_1 = b_3 = 0.0419$, and $b_2 = 0.0647$ the slope parameter values for each shunt resonator, which are derived from the canonical formulas for the designed filter [2]. The susceptance slope parameter for the resonator having null susceptance at center frequency is defined as:

$$b_i = \frac{\omega_0}{2} \left. \frac{dB_i(\omega)}{d\omega} \right|_{\omega=\omega_0} \quad (4.15)$$

where $B(\omega)$ is the susceptance of the distributed resonator.

Table 4. 7. - OPTIMAL COARSE SOLUTIONS, REFLECTION AND TRANSMISSION ZERO FREQUENCIES

	L_p [nH]	C_p [pF]	L_{sh} [nH]	f_0 [GHz]	f_z [GHz]
C1,C3	1.897	3.338	0.677	2	3.9
C2	1.232	5.148	0.439		

Note for this case, in order to achieve a more compact design, the dimension c is now fixed to a smaller value (i.e. $c = 0.20$ mm) during the application of the ASM algorithm. The final synthesized dimensions of each cell are summarized in Table 4.8 (error under 1.5%), and graphically depicted in Fig. 4.12.

Table 4. 8. - FINE PARAMETERS, ITERATION NO. AND ERROR FUNCTION NORMS

		r_{ext} [mm]	d [mm]	e [mm]	Iter. No.	$\ f\ $	$\ f_{norm}\ $
C1, C3 ($c=0.20$ mm)	Initial $x_{em}^{(1)}$	3.5	0.74	0.25	1	7.5144	2.455
	Final $x_{em}^{(13)}$	2.17	0.87	0.29	12	0.0207	0.0147
C2 ($c=0.20$ mm)	Initial $x_{em}^{(1)}$	3.5	0.74	0.49	1	6.2080	2.6008
	Final $x_{em}^{(11)}$	2.56	1.68	0.97	11	0.0164	0.0129

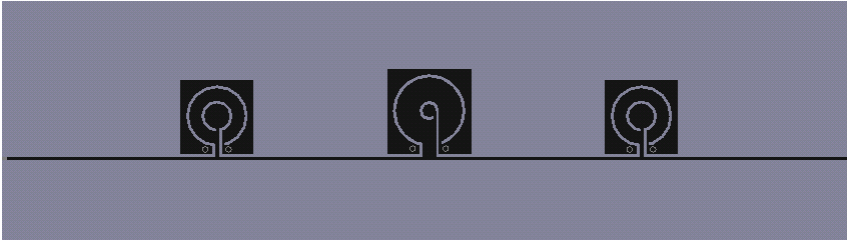


Fig. 4.12.-Layout of the 3-order bandpass filter (redesigned). The circuit target parameters are summarized in Table 4.7 and dimensions in Table 4.8. The dimension of microstrip $\lambda/4$ lines are the same of the previous design.

The simulated responses of the equivalent circuit and the layout (using ANSYS DesignerRF) of the new designed filter are displayed in Fig. 4.13, resulting into a clear improvement in the performance of the filter, specifically if we compare the out-of-band results with those of Fig. 4.10. This new prototype has not been fabricated yet, so not measurements can be provided. Some other details of interest can be found in [3], where most of the work presented in this section is published.

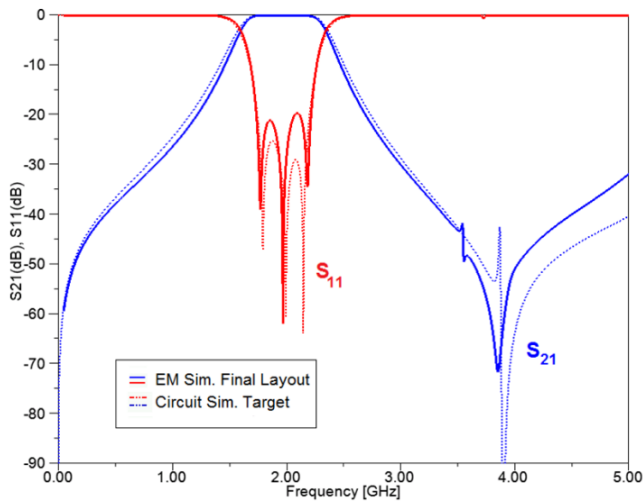


Fig. 4.13. - Insertion and return losses of the re-designed (enhanced out-of-band response) wideband bandpass filter based on OCSRRs.

References

- [1] J. Selga, A. Rodriguez, V. E. Boria, and F. Martin, “Synthesis of split rings based artificial transmission lines through a new two-step, fast converging, and robust Aggressive Space Mapping (ASM) algorithm”, *IEEE Transactions on Microwave Theory and Techniques*, vol. 61, no. 6, pp. 2295-2308, June 2013.
- [2] Jia-Sheng Hong, and M. J. Lancaster, *Microstrip Filters for RF/Microwave Applications*, John Wiley & Sons, 2001.
- [3] A. Rodriguez, J. Selga, V. E. Boria, and F. Martin, “Synthesis of open complementary split ring resonators (OCSRRs) through aggressive space mapping (ASM) and application to bandpass filters”, *Proceedings of 44th European Microwave Conference (EuMC)*, Rome (Italy), pp. 323-326, 5th-10th Oct. 2014.

CHAPTER 5

Conclusions and Future Work

5.1. Conclusions

5.2. Future Research Lines

*“Life can only be understood backwards;
but it must be lived forwards”*

Søren Kierkegaard



5 CONCLUSIONS AND FUTURE WORK

As it was outlined in the first chapter of this document, the main aim of this Ph.D. thesis work is to make easier the engineer's work for the design and synthesis of transmission lines based on MTM concepts, and as result contribute to the wider use of this technology (in particular the one based on its resonant approach). Even still lot of work needs to be done (just few cells have been synthesized up to now), we have proved that space mapping techniques, widely used in the microwave field and rarely applied in the field of metamaterials till date, can be a very good option. In the next sections, we go little more in detail through the main conclusions and the research lines derived from the present work.

5.1 Conclusions

This thesis has been performed in very close collaboration with the UAB, so two different knowledge backgrounds were joined together: optimization applied to microwave devices and expertise in the metamaterial field, in order to establish a fruitful technical collaboration. Proof of that, are the several publications and international conference papers, listed at the end of this document.

Earlier techniques to obtain the wished synthesis results relied on engineer's knowledge, use of advanced EM solvers, and parameter extraction techniques. We have gone one step forward not only by proposing an automated technique (see section 3.3.1), but also different enhancements (LS –section 3.3.2- and Two-Step approach –section 3.3.3-). As a consequence, the costs in terms of time (CPU effort) and computational resources have been dramatically decreased.

Of special interest is the two-step approach we have developed, since it provides a good estimation of the implementable circuit elements limits. It is able to predict whether a given set of element values of the equivalent circuit model of the unit cell can be physically implementable or not. Therefore, the resulting synthesis algorithm is more robust. The methodology has been proven, not just with simulations, being different practical application examples manufactured and measured, see chapter 4. The first example is a stop-band filter achieved by basically cascading three unit cells of CSRR-loaded metalines (small length of microstrip line between adjacent cells was introduced to

minimize the coupling effects that equivalent circuit does not predict). A good agreement between the measured results, EM and circuital simulation is achieved, and hence validating the designing process in the region of interest. There are small discrepancies that can be attributed to the employed manufacturing process. The second one is a dual-band power divider obtained with CSRR-gap-loaded metaline unit cell and two transmission line sections cascaded to the input and output ports (in order to find implementable values for the metaline unit cell). The agreement is excellent in the left handed region, where the model describes the structure very well, and not so good for upper frequencies, where the equivalent model is not as accurate. Last example, shows a 3-order bandpass filter, based on OCSRRs transmission lines and inverters (implemented by means of $\lambda/4$ lines). The measurement results show also a good performance of the proposed design method in the working region. In summary, it has been demonstrated that ASM algorithms are a useful tool for the automated synthesis of metamaterial transmission lines.

5.2 Future Research Lines

Many interesting topics still remain open in this so exciting and interesting research field. Some of them are briefly outlined next:

- Apply space mapping techniques to other types of MTM-based unit cells: e.g. SRR and SRR-based particles as OSRR, coupled to other types of host lines (i.e. coplanar, stripline, etc.), as well as to achieve more complex designs (high order filters, inclusion of other components as varactors).
- Development of more complex/advanced equivalent circuits that take into account the coupling effects between cells, in order to apply the same - or similar- optimization techniques, and then having a more powerful designing tool.
- Application of similar synthesis/design techniques to other planar technologies, for instance not based on MTMs. Some progress in that direction has already been started. The synthesis of Stepped Impedance Resonators (SIRs), whose EM response is identical to a series LC resonator, has also been performed using ASM techniques (see for instance the references [10]-[12] corresponding to international conferences). It is a very useful component for the design of filters and diplexers.

- Recently, a graphical interface, and all the programming related to the proposed synthesis technique, is being translated to Python (open source program), in order to explore its possible integration within commercial software tools, see some preliminary results in Fig. 5.1. That was one of the possible goals at the beginning of the thesis that now can be faced with some chances for final success.

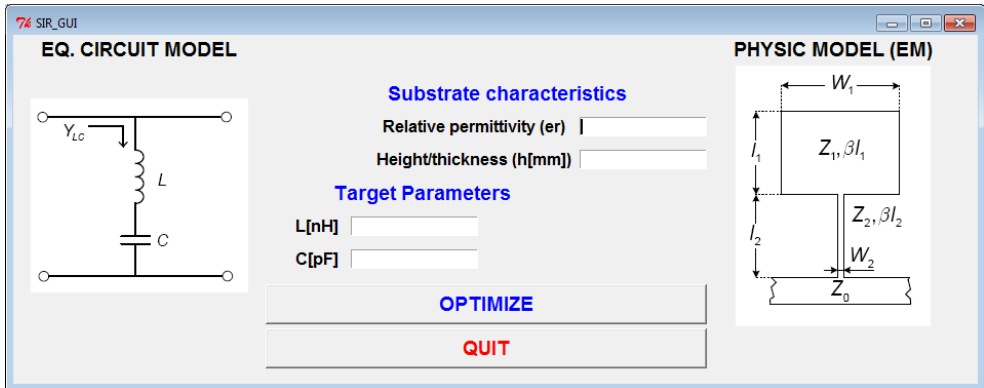


Fig. 5. 1. - SIR interface programmed in Python.

Other particles that are also being object of our interest are RF/microwave inductors, since they are a key component for applications. We have just started to develop some preliminary work on the synthesis of spiral inductors and omega inductors (see Fig. 5.2), but it is still in progress.

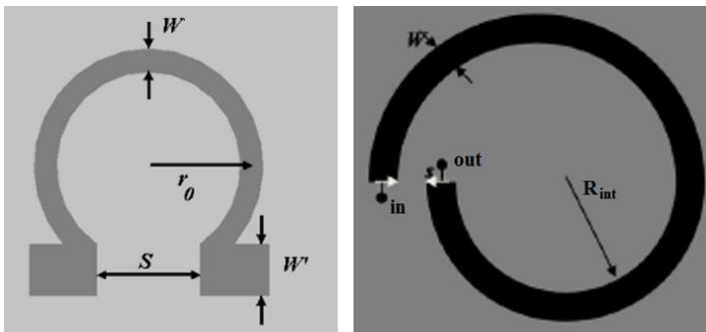


Fig. 5. 2. - Topology of omega and spiral (one turn) inductor.

- Generation of the automated synthesis from filter specifications, i.e., central frequency, fractional bandwidth, in-band ripple and order, having a fully automated tool. We have already overcome the whole problem (taking in account the effects of the narrow-band operation of the quarter-

wavelength admittance inverters) for the case of SIRs, i.e. a recent paper has been accepted, see [6]. Since similar problems appear with OCSRR (example of section 4.3), we are considering to apply a similar methodology to this type of filter design.

LIST OF PUBLICATIONS

International Journals and Book Chapters

[1] J. Selga, A. Rodríguez, M. Gil, J. Carbonell, V. E. Boria, and F. Martín, “Towards the automatic layout synthesis in resonant-type metamaterial transmission lines”, *IET Microwaves Antennas & Propagation*, vol. 4, no. 8, pp. 1007-1015, Aug. 2010.

[2] J. Selga, A. Rodríguez, M. Gil, J. Carbonell, V. E. Boria, and F. Martín, “Synthesis of planar microwave circuits through aggressive space mapping using commercially available software packages”, *International Journal of RF and Microwave Computer-Aided Engineering*, vol. 20, no. 5, pp. 527-534, Sep. 2010.

[3] J. Selga, A. Rodríguez, V. E. Boria, and F. Martín, “Synthesis of split rings based artificial transmission lines through a new two-step, fast converging, and robust Aggressive Space Mapping (ASM) algorithm”, *IEEE Transactions on Microwave Theory and Techniques*, vol. 61, no. 6, pp. 2295-2308, June 2013.

[4] A. Rodríguez, J. Selga, F. Martín, and V. E. Boria, “Practical Application of Space Mapping Techniques to the Synthesis of CSRR-Based Artificial Transmission Lines”, in *Surrogate-Based Modeling and Optimization*, S. Koziel and L. Leifsson (Editors), New York, Springer, pp. 81-97, 2013.

[5] J. Selga, A. Rodríguez, M. Orellana, V. E. Boria, and F. Martín, “Practical application of space mapping techniques to the synthesis of CSRR-based artificial transmission lines,” *Applied Physics A*, vol. 117, issue 2, pp. 557-565, Nov. 2014.

[6] M. Sans, J. Selga, A. Rodríguez, V. E. Boria, and F. Martín, “Unattended synthesis of planar wideband bandpass filters from specifications using a two-step aggressive space mapping (ASM) algorithm,” *IEEE Transactions on Microwave Theory and Techniques* (ACCEPTED for publication Oct. 2014).

International Conferences

- [1] A. Rodriguez, J. Selga, M. Gil, J. Carbonell, V. E. Boria, and F. Martin, "Automated synthesis of resonant-type metamaterial transmission lines using aggressive space mapping", IEEE MTT-S International Microwave Symposium Digest, Anaheim, CA, USA, pp. 209-212, May 2010.
- [2] J. Selga, A. Rodriguez, J. Carbonell, V. E. Boria, and F. Martin, "Synthesis of metamaterial transmission lines through aggressive space mapping", 4th International Congress on Advanced Electromagnetic Materials in Microwaves and Optics (Metamaterials 2010), Karlsruhe (Germany), pp. 690-692, 13-16 Sep. 2010.
- [3] A. Rodriguez, J. Selga, F. Martin, and V. E. Boria, "A more robust approach for the automated synthesis of artificial transmission lines combining Aggressive Space Mapping with line search", 4th Young Scientist Meeting on Metamaterials (YSMM'11), Valencia (Spain), 14-16 Feb. 2011.
- [4] J. Selga, A. Rodriguez, V. E. Boria, and F. Martin, "Automated parameter extractor for metamaterial transmission lines based on complementary split ring resonators (CSRRs)", 4th Young Scientist Meeting on Metamaterials (YSMM'11), Valencia (Spain), 14-16 Feb. 2011.
- [5] J. Selga, A. Rodriguez, V. E. Boria, and F. Martin, "Application of aggressive space mapping to the synthesis of composite right/left handed (CRLH) transmission lines based on complementary split ring resonators (CSRRs)", Proceedings of 41st European Microwave Conference (EuMC), Manchester (UK), pp. 968-971, 10-13 Oct. 2011.
- [6] A. Rodriguez, J. Selga, V. E. Boria, and F. Martin, "On the implementation of a robust algorithm which automates the synthesis of artificial transmission lines based on CSRRs" 5th International Congress on Advanced Electromagnetic Materials in Microwaves and Optics (Metamaterials 2011), Barcelona (Spain), 10-15 Oct. 2011.
- [7] A. Rodriguez, J. Selga, V. E. Boria, and F. Martin, "Practical application of space mapping techniques to the synthesis of CSRR-based artificial transmission lines," 3rd International Conference on Metamaterials, Photonic Crystals and Plasmonics (META 2012). Paris (France). 19-22 April 2012.

- [8] A. Rodriguez, J. Selga, F. Martin and V. E. Boria, "Practical application of space mapping techniques to the synthesis of CSRR-based artificial transmission lines", 3rd International Workshop on Surrogate Modelling and Space Mapping for Engineering Optimization (SMSMEO 2012), 9-11 August 2012.
- [9] A. Rodriguez, V. E. Boria, J. Selga, and F. Martin, "A robust space mapping method for the practical synthesis of CSRR-based artificial transmission lines from equivalent circuit models", Proceedings of 42nd European Microwave Conference (EuMC), Amsterdam (The Netherlands), pp. 671-674, 28 Oct.-2 Nov. 2012.
- [10] J. Selga, A. Rodriguez, J. Naqui, M. Duran-Sindreu, V. E. Boria, and F. Martin, "Application of aggressive space mapping (ASM) to the efficient synthesis of stepped impedance resonators (SIRs)", Proceedings of 43rd European Microwave Conference (EuMC), Nuremberg (Germany), 6-11 Oct. 2013.
- [11] J. Selga, A. Rodriguez, M. Orellana, V. E. Boria, and F. Martin, "Practical application of space mapping techniques to the synthesis of CSRR-based artificial transmission lines," 3rd International Conference on Metamaterials, Photonic Crystals and Plasmonics (META 2014). Singapore. 20-23 May 2014.
- [12] J. Selga, M. Sans, J. Bonache, A. Rodriguez, V. E. Boria, and F. Martin, "Automated synthesis of planar wideband bandpass filters based on stepped impedance resonators (SIRs) and shunt stubs through aggressive space mapping (ASM)", IEEE MTT-S International Microwave Symposium Digest, Tampa, Florida, USA, 1-6 June 2014.
- [13] A. Rodriguez, J. Selga, V. E. Boria, and F. Martin, "Synthesis of open complementary split ring resonators (OCSRRs) through aggressive space mapping (ASM) and application to bandpass filters", Proceedings of 44th European Microwave Conference (EuMC), Rome (Italy), pp. 323-326, 5-10 Oct. 2014.